Intracavity Frequency Doubling of Optically Pumped Semiconductor Disk Lasers to the Green Spectral Range

Dissertation
zur Erlangung des Doktorgrades
des Department Physik
der Universität Hamburg

vorgelegt von
René Hartke
aus Lohne (Oldenburg)

Hamburg
2008

Gutachter der Dissertation:	Prof. Dr. G. Huber Prof. Dr. K. Sengstock
Gutachter der Disputation:	Prof. Dr. G. Huber Priv. Doz. Dr. V. Baev
Datum der Disputation:	24.01.2008
Vorsitzender des Prüfungsausschusses:	Dr. K. Petermann
Vorsitzender des Promotionsausschusses:	Prof. Dr. G. Huber
Dekan der Fakultät für Mathematik, Informatik und Naturwissenschaften:	Prof. Dr. A. Frühwald

Abstract

René Hartke, *Intracavity Frequency Doubling of Optically Pumped Semiconductor Disk Lasers to the Green Spectral Range*

Optically pumped semiconductor disk lasers are compact light sources of high beam quality and thus they are in principle suitable for use in display technology. In this thesis the development of a green emitting optically pumped semiconductor disk laser is presented, for which the desired properties for application in compact projectors are taken into account. On the fundamental wave the laser exhibits diffraction limited beam quality and output powers up to a few hundreds of milli-Watts. Via intracavity frequency doubling, stable and efficient emission at 525 nm is achieved. For optimization of efficiency, beam quality, and adjustability, the properties of resonators comprising the nonlinear crystals KTP, LBO, BiBO, and MgO:PPLN are compared. The highest efficiency is achieved with BiBO at an output power of 113 mW at 525 nm. An optical conversion efficiency of 81% with respect to the maximum achievable infrared power is presented. The best overall performance is demonstrated with MgO:PPLN. The usability of MgO:PPLN structures with broadened spectral acceptance is examined. It is found, that such structures only are beneficial for resonators, where the second harmonic is coupled out to both sides of the nonlinear crystal. Furthermore, the output power is characterized towards amplitude fluctuations. The typically stable output of the optically pumped semiconductor disk laser can be attributed to single-mode operation. In the case of sum frequency generation a dependence of the output fluctuations on gain-decoupling of the fundamental modes is found.

Inhaltsangabe

René Hartke, *Intracavity Frequency Doubling of Optically Pumped Semiconductor Disk Lasers to the Green Spectral Range*

Optisch gepumpte Halbleiter-Scheibenlaser sind als kompakte Lichtquellen mit hoher Strahlqualität prinzipiell für den Einsatz in der Display Technologie geeignet. In dieser Arbeit wird ein grün emittierender Halbleiter-Scheibenlaser vorgestellt, bei dessen Entwicklung die benötigten Eigenschaften für Anwendung in kompakte Projektoren berücksichtigt werden. Auf der Grundwellenlänge von 1050 nm hat der Laser eine beugungsbegrenzte Strahlqualität und erreicht Ausgangsleistungen bis zu einigen hundert mW. Mittels resonatorinterner Frequenzverdopplung wird stabile und effiziente Emission bei 525 nm erreicht. Zur Optimierung von Effizienz, Strahlqualität und Justierbarkeit werden die Eigenschaften von Resonatoren mit den nichtlinearen Kristalle KTP, LBO, BiBO und MgO:PPLN verglichen. Die höchste Effizenz wird mit BiBO bei einer Ausgangsleistung von 113 mW bei 525 nm erreicht. Eine optische Konversionseffizienz von 81% bezogen auf die maximal erreichbare Infrarotleistung wird präsentiert. Die besten Ergebnisse unter Einbeziehung aller Parameter werden mit MgO:PPLN erzielt. Die Verwendbarkeit von MgO:PPLN Strukturen mit verbreiterter spektraler Akzeptanz für resonatorinterne Frequenzverdopplung wird untersucht. Dabei zeigt sich, dass solche Strukturen nur für Resonatoren vorteilhaft sind, bei denen die zweite Harmonische zu beiden Seiten des nichtlinearen Kristalls ausgekoppelt wird. Desweiteren wird die Ausgangsleistung auf Amplitudenfluktuationen untersucht. Die typischerweise stabile Ausgangsleistung des optisch gepumpten Halbleiter-Scheibenlasers kann auf Einmodenbetrieb zurückgeführt werden. Für den Fall von Summenfrequenzmischung wird ein Zusammenhang zwischen Emissionsfluktuationen und dem Entkopplungsparameter der fundamentalen Lasermoden festgestellt.

Contents

1 Introduction

1.1 Motivation

Laser technology has successfully made its way from the laboratories to applications in everyday life. High power lasers are used for drilling, marking or welding and low power lasers in the infrared and visible spectral range are utilized for telecommunication or data storage. Lasers are also established for various medical treatments, for spectroscopic measurements or in micro-lithography.

Another important upcoming market is lasers as light sources in projection display technology. By mixing the three colors red, green, and blue, laser displays can cover a much wider spectral range than actual television systems. Furthermore, they offer extremely high contrasts and, due to the operating principle, they are always in focus on any kind of surface. Additional to the optical performance, prospective laser projection systems are believed to be less power consuming and more compact than comparable conventional display technologies. Some of these advantages have been proven in commercially available large screen projectors such as those used in planetariums or cinemas. However, these systems are still bulky and very expensive.

Hence in the next step the size and the costs have to be reduced in order to break into markets of mass applications like laser television or pocket-projectors. Due to the enormous potential of these consumer markets, there is a significant interest for compact and cheap laser sources in the visible spectral range. For many display applications, like integrated projectors in mobile phones or head-up displays in cars, only low output powers are needed, i. e. a few tens of mW for green. The objective of this thesis is to contribute to the development and optimization of a compact and efficient laser in the green spectral range suitable for this kind of applications. The desired display devices require lasers, that can be fabricated at high production volumes and relatively low costs. Semiconductor lasers have already proven to be perfectly suited for such requirements as they are successfully used in consumer applications like laser printers or for data storage in DVD players and similar devices.

Regrettably there is a gap in the green spectral range for laser emission of semiconductors. Accordingly no green diode lasers are available so far. But the gap can be filled by frequency doubling of an InGaAs/GaAs based material system.

Conventional edge emitting semiconductor lasers are severely limited for frequency dou-

bling, since they typically suffer from a bad beam quality. Furthermore, they lack an external cavity, which is desirable for introducing additional resonator elements and for profiting from the much more efficient intracavity frequency doubling concept. In contrast, optically pumped semiconductor (OPS) disk lasers, which are also known as vertical external cavity surface emitting lasers (VECSEL), overcome these limitations, as they provide an external cavity and diffraction limited beam quality [Kuz97].

The OPS disk laser concept combines the advantageous beam quality and power scalability of dielectric solid state thin disk lasers with the flexibility of wavelength engineering known from edge emitting semiconductor lasers. Since OPS disk lasers also allow for a very compact laser design, they are promising candidates for laser display technology. Compact laser displays can be built using a flying spot concept, where the beam is scanned over the projection screen by miniature mirrors. This concept requires very high beam quality, since the sharpness of the resulting image strongly depends on the focus size and the beam divergence. Furthermore, the laser has to be capable of fast power modulation. For a projection with VGA resolution (640x480) and a frame rate of 80 Hz, modulation frequencies of about 25 MHz are required. The output of the laser should exhibit low amplitude fluctuations to guarantee homogeneous illumination of the full screen. The green emitting frequency doubled OPS disk lasers considered in this thesis are characterized and optimized towards these requirements.

To achieve high efficiencies in the green at relatively low powers, optimized nonlinear conversion is required. Therefore choosing the optimum conversion material is crucial. In this thesis the performance of the nonlinear crystals lithium triborate (LBO), potassium titanyl phosphate (KTP), bismuth borate (BiBO), and magnesium-oxide doped periodically poled lithium niobate (MgO:PPLN) will be compared.

1.2 The project 'VISULASE'

The work of this thesis was part of the BMBF-project VISULASE (VISUalization by semiconductor based RGB LASErs in automotive and consumer applications) under FKZ 13N8592. The aim of this project was the development of a laser projection system based on red, green, and blue (RGB) semiconductor lasers with high brilliance. Within the project, design concepts for various display applications have been investigated and demonstrated.

A main target of the project was the conception and demonstration of a head-up display for application on front windshields, but other applications were also considered and taken into account for the laser development. It is expected that various new products will benefit from the knowledge gained through this project. The results presented in this thesis characterize some fundamental properties of the green laser source.

1.3 Outline

The structure of this thesis is as follows. In chapter 2 the basic functional principles of OPS disk laser operation are presented. Structure and properties of the gain material, as well as different pumping schemes are described. A characterization of laser operation on the fundamental wave is presented in chapter 3. The laser performance is described regarding output power, polarization, emission spectra, tunability, and beam quality. The 4th chapter provides the theoretical background for second harmonic generation. The most relevant effects occurring for intracavity frequency doubling of OPS disk lasers are described. The results for birefringent phase matched frequency doubling with LBO, BiBO, and KTP are presented and discussed in chapter 5. Quasi phase matched SHG using MgO:PPLN is addressed in chapter 6. Poling designs for broadened spectral acceptance are presented and compared to single period structures. Chapter 7 provides an analysis of the continuous wave output dynamics. Finally, the main results of this thesis are summarized in chapter 8 and an outlook is given.

2 The basic principles and properties of OPS disk lasers

Semiconductor lasers are compact and highly efficient laser sources. The flexible wavelength design allows for an enormous variety of applications. However, edge emitting semiconductor lasers often suffer from a poor beam quality and high divergence. On the other hand approaches like ridge wave-guides or electrically pumped vertical cavity surface emitting lasers (VCSELs) achieve excellent beam quality, but are limited in output power.

High-power operation of edge emitting diode lasers with high brightness is prevented by different effects:

- catastrophic optical mirror damage
- temperature increase in the active region
- spatial hole burning for structures with high gain volume
- damage of the QW caused by filamentation in the active region due to self-focussing effects

The concept of OPS disk lasers overcomes these limitations and combines the benefits of semiconductor lasers with the advantages of diode pumped solid state lasers. High continuous-wave output powers can be achieved with near diffraction limited beam quality, while the emission wavelength can be designed with high flexibility. The external cavity allows for a variety of applications like intracavity frequency doubling, mode-locking, tunability or intracavity absorption spectroscopy. The basic operation principles of these emerging lasers are discussed in this chapter.

2.1 The OPS disk laser concept

In 1994 Giesen et al. [Gie94] introduced diode pumped solid state thin disk lasers as a power scalable concept. Recently output powers of more than 5 kW have been extracted from a single disk [Gie07]. The high efficiency is based upon an axial cooling configuration. The laser crystal thickness is kept small (typically a few 100 µm) with respect to the mode diameter. The crystal disk is bonded to a water-cooled heat sink. This design

allows for very efficient heat removal due to the high cooling surface to volume ratio. The thermal gradient is established along the laser axis, the thermal lens is very low for thin disk lasers and thus good beam quality can be achieved even at high powers.

A schematic of such a laser is shown in Fig. 2.1 (a). The crystal is high-reflection (HR) coated on the back side and anti-reflection (AR) coated on top for both the pump and the laser wavelength. The resonator is formed by the HR-coating and an external curved output coupler. Due to the small absorption length, the crystal is typically pumped in a multi-pass geometry consisting of a parabolic mirror and a set of roof-top prisms. As pump source usually a fiber coupled diode laser is used. Thin disk lasers typically use ytterbium- or neodymium-doped crystals, which have high gain cross sections. For an ytterbium-doped lutetium oxide (Yb:Lu_2O_3) thin disk laser a slope efficiency of 80% has been observed for a laser module providing 24 pump passes [Pet07].

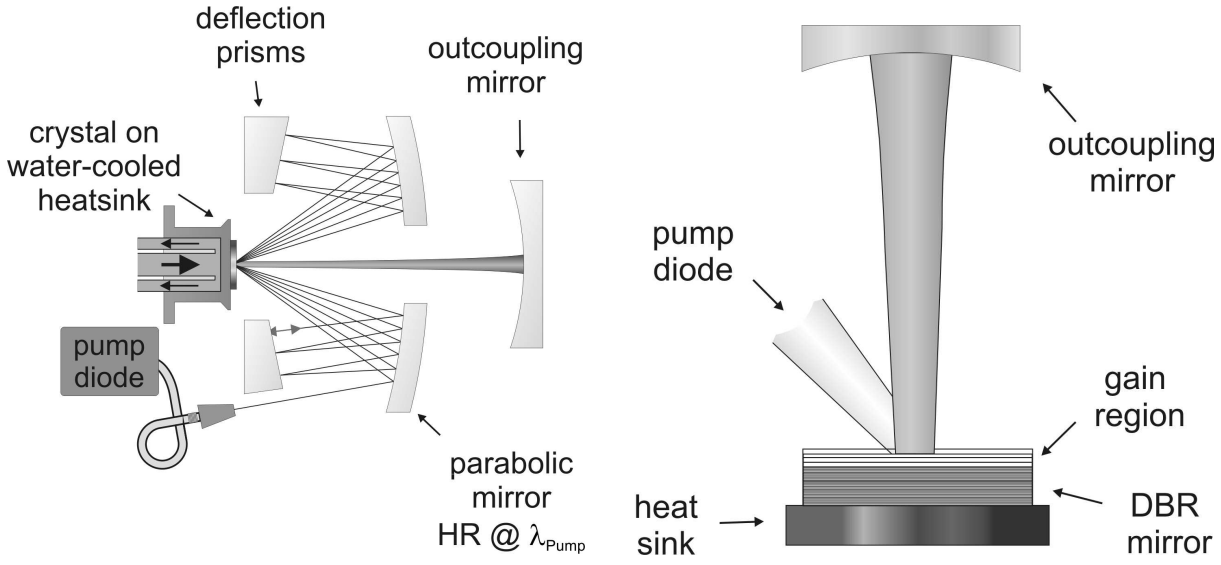

(a) solid state thin disk laser (b) OPS disk laser

Figure 2.1: Schematic of (a) a solid state thin disk laser and (b) an OPS disk laser.

OPS disk lasers follow the same principle concept, except that they use a semiconductor as gain material instead of a dielectric crystalline disk (see Fig. 2.1 (b)). The semiconductor chip generally consists of a distributed Bragg reflector (DBR) and a gain region containing several quantum wells spaced by barrier layers. The cavity is formed by the Bragg mirror and an external output coupler. No bulky and complicated pump geometry is required since the absorption coefficient is much higher than for solid-state laser materials. For conventional barrier pumping (see section 2.3) typically more than 95% of the pump light is absorbed in a single pass.

The gain length of the active medium is drastically reduced compared to almost any other type of lasers. A single quantum well has a thickness of only a few nanometers.

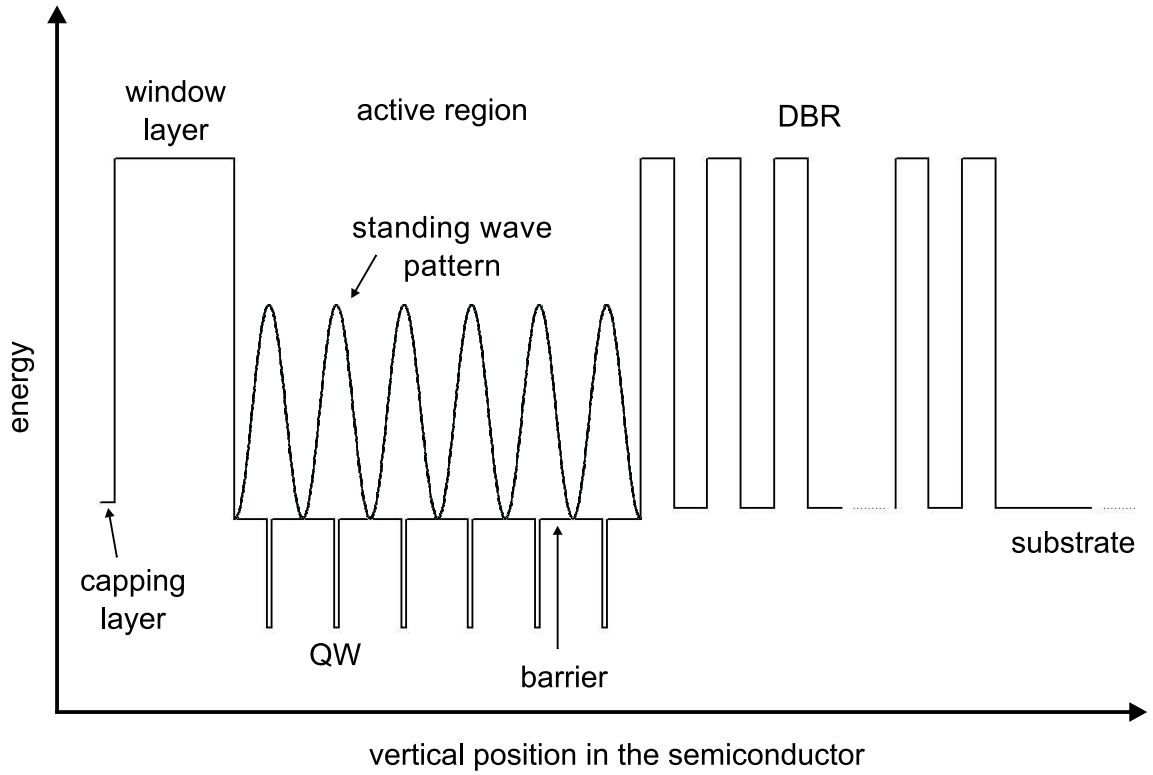

Figure 2.2: Bandgap diagram of a resonant periodic gain structure.

Therefore, it is crucial to optimize the performance of the active medium. In order to enhance the effectiveness of each quantum well, the active layers of the semiconductor form a so called resonant periodic gain (RPG) structure. Figure 2.2 shows a bandgap diagram of such a RPG structure. The quantum wells are spaced at half wavelength intervals corresponding to the positions of the antinodes of the standing wave pattern in the semiconductor sub-cavity formed by the Bragg mirror and the capping layer. Thus the electrical field is particularly high at the quantum wells resulting in efficient stimulated carrier-hole pair recombination. The gain coefficient of semiconductor materials typically is of the order of thousands per centimeter. In combination with the high electric fields at the wells due to the RPG design, sufficient total gain for laser operation can be achieved even if only a few active layers are embedded in the structure.

The gain region is covered by a window layer. This potential barrier prevents carriers from diffusing to the surface of the chip, which would lead to non-radiative electron-hole pair recombination. An aluminum-free capping layer protects the chip from oxidation. For bottom-up grown structures (see section 2.4) the semiconductor chip is topped by an etch stop layer for fabrication purposes. In some cases an anti-reflective coating is added to prevent etalon effects within the active region. This is of special interest whenever a broad emission spectrum is desired.

The RPG structure is typically pumped by a diode laser, which is a cheap and well-studied technology. This concept overcomes the limitations of current injection, where uniform pumping is hard to achieve over large areas. Like for the solid state thin disk laser described above, the poor beam quality of the pump laser is converted to a laser emission with high brilliance. OPS disk lasers can therefore be understood as beam quality converters. Another advantage of the optical pumping scheme in comparison with electrically pumped semiconductor lasers is, that wavelengths around 2 µm, for which electrical pumping is technically difficult, can be accessed.

In 1997 Kuznetsov *et al.* demonstrated the first OPS disk laser that was capable of producing high (> 0.5 W) continuous-wave output power [Kuz97]. Their laser operated around 1.0 µm with a circular TEM_{00} beam. Similar to solid state thin disk lasers the OPS disk laser concept allows for power scaling by varying the size of the pumped area [Lut03]. A good overview of OPS disk lasers and their properties is given in [Tro04] and is described in more detail in [Tro06] and [Kel06].

2.2 Gain media

Semiconductor gain media allow for flexible design of the emission wavelength by bandgap engineering. Using different material systems, a spectral range from about 650 nm to about 2350 nm can be covered with OPS disk lasers so far. Via frequency doubling this range can be extended from the visible to the ultraviolet. Theoretically, an even larger wavelength range could be obtained with the known compounds, but pushing the boarders further results in significant lattice mismatch, which leads to high defect concentration and accordingly prohibits efficient laser operation. The semiconductor structures for OPS disk lasers are typically grown by molecular beam epitaxy (MBE) or metal-organic vapor-phase epitaxy (MOVPE), which provide single atomic layer accuracy and low defect concentration.

The OPS disk laser presented in this thesis is based on an InGaAs/GaAs system. InGaAs quantum wells sandwiched between GaAs barriers is a well studied and widely used material system, which is commercially established for semiconductor lasers around 980 nm. InGaAs is also of importance in VCSEL technology [Li03], where it is combined with two GaAs/AlAs multi-layer reflectors with high index contrast. By varying the indium content, wavelengths between ~ 905 nm and ~ 1300 nm can be realized with InGaAs/GaAs quantum well lasers.

The different lattice constants of cubic GaAs ($a_{GaAs} = 5.65$ Å) and InAs ($a_{InAs} = 6.06$ Å) [Hoc66] cause a crystal deformation, which increases for higher indium content x in the $In_xGa_{1-x}As$-layers. The variation of the indium content and the corresponding compressive strain change the shape of the valence bands. An empirical formula for the energy gap of strained quantum wells for different indium concentrations was given by Chow

et al. [Cho94]. For $In_xGa_{1-x}As$ at $T = 77\,K$ they found

$$E_g(x) = 1.508\,eV - 1.47\,eV \cdot x + 0.375(eV)^2 \cdot x^2 \tag{2.1}$$

and at $T = 300\,K$

$$E_g(x) = 1.43\,eV - 1.53\,eV \cdot x + 0.45(eV)^2 \cdot x^2 \tag{2.2}$$

The bandgaps at the other temperatures are assumed to be computable from a linear fit. For strain compensation in structures with high indium content, GaAsP layers can be added to the system.

Compressively strained InGaAs/GaAs exhibits high gain and a low laser threshold. For emission around 1 µm high quality mirrors can be grown with GaAs and AlAs layers, since these materials are almost perfectly lattice matched. For the given material system oxidation of layers containing aluminum can occur. Oxidation prevention layers such as SiO_2 or SiN_x can be deposited on the surface to protect the structure.

2.3 Pumping concepts

Injection pumping is generally the most convincing method to pump semiconductors, because only a single power conversion step is required. Low thresholds and high efficiencies for edge emitting quantum well structures are achieved this way. However, electrically pumped vertical cavity semiconductor lasers suffer from carrier density anisotropy when being scaled to higher output powers, a problem that can be overcome by homogeneous optical pumping with diode lasers. In the following section the different pumping concepts for OPS disk lasers that have been proposed and demonstrated so far will be presented.

Barrier pumping

The most straight forward method for optical pumping of vertical emitting quantum well structures is barrier pumping. In this method the pump wavelength is chosen to be below the absorption edge of the barrier layers between the quantum wells (see Fig. 2.3 (left)). The contribution of absorption in the quantum wells is small, since their thickness is small in comparison with the barriers.

Barrier pumped VECSELs typically absorb most of the pump power during a single pass through the active region. The generated electrons and holes diffuse over the respective layers and are finally captured in the quantum wells. Carrier capture times are of the order of tens of picoseconds and depend on the structure. The transport of the electron-hole pairs to the quantum wells can be optimized by shaping the barrier gap with a graded index (GRIN) [Saa06].

The disadvantage of this pumping scheme is its low quantum efficiency. The quantum defect and the corresponding thermal load can be minimized by adjusting the well depth. However, in order to provide good carrier confinement, the potential wells have to be sufficiently high. Moreover the bandgap in the barrier regions sets the lower limit for the wavelength of the pump laser. Accordingly the minimization of the quantum defect is limited by the quantum confinement of the carriers. The thermal load induced this way is a critical problem for efficient high power operation of OPS disk lasers (see section 2.4).

Another drawback of barrier pumping is a longitudinal inhomogeneous depletion of the pump power, which is a consequence of the high absorption coefficient. For a multi quantum well RPG structure the carrier density thus varies over the length of the gain region. By introducing double wells at antinode positions close to the surface and omitting quantum wells at positions close to the Bragg mirror, the homogeneity of the carrier distribution over all quantum wells can be improved.

In-well pumping

The quantum defect and the thermal load can be reduced by pumping the quantum well directly [Sch04]. Figure 2.3 (right) shows a schematic diagram of in-well pumping. In this pumping concept the pump wavelength is chosen such that the incoming photons are only absorbed at the quantum wells. The pump level has to be high enough above the upper laser level to avoid bleaching at high carrier densities.

A problem arising for in-well pumping is the short absorption length, since the quantum wells are only a few nanometers thick. Higher numbers of quantum wells lead to longer total absorption lengths, but also result in a higher laser threshold. To increase the pump efficiency, a resonant absorption scheme was introduced [Bey05]. Here the pump wavelength is chosen such that

$$\lambda_{pump} = \lambda_{laser} \cdot cos(\alpha^{'}) \tag{2.3}$$

where $\alpha^{'}$ is the angle of the incoming pump light inside the semiconductor with respect to the surface normal.

Another approach to increase the absorption length is a multi-pass pump setup, which is a well-known concept for dielectric solid state thin disk lasers. Multi-pass pumping can also be combined with resonant absorption for further improvement of the absorption efficiency.

From pump power dependent laser emission spectra, the reduction of the thermal load for in-well pumping can been seen [Bey05]. A decreased thermal shift of the output wavelength for in-well pumping indicates a significantly reduced thermal load compared to barrier pumping. The reduction of the thermal load allows for extension of the

wavelength range for a given material system. In-well pumping was used for the first cw OPS disk lasers in the red spectral range [Mul03]. Laser operation at 2350 nm in-well pumped at 1960 nm has been demonstrated recently [Sch07]. Moreover, multi-watt operation of an in-well pumped OPS disk laser emitting at 920 nm [Alb05] as well as 67% slope efficiency at 853 nm have been achieved [Bey07].

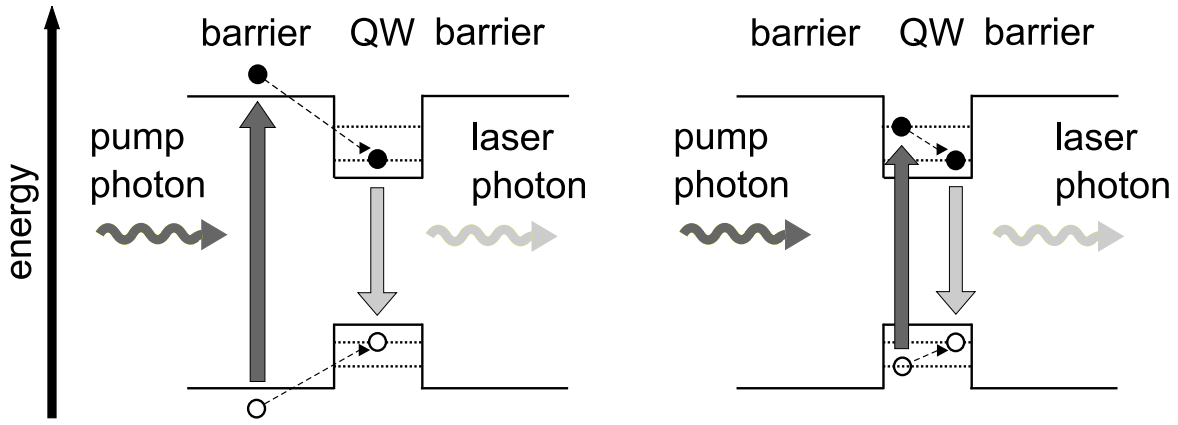

Figure 2.3: Schematic of barrier pumping (left) and in-well pumping (right).

End-pumped OPS disk lasers

The first end-pumped OPS disk laser was demonstrated by Lee *et al.* at Samsung Advanced Institute of Technology in 2006 [Lee06a]. The advantages are a round pump profile and an increased flexibility of the resonator design, since no pump optics limit the positioning of intracavity elements. The absorption in an end-pumped OPS disk laser is similar to a conventional barrier pumped OPS disk laser. Figure 2.4 (left) shows a schematic of this concept. The Bragg mirror is modified for high pump light transmission. Furthermore the semiconductor is bonded to a heat-spreader, that is transparent at the pump wavelength. In the case of Lee *et al.* diamond was used as heat-spreader. End-pumped OPS disk lasers were also used to obtain green and blue emission via frequency doubling [Kim06]. A maximum continuous wave output power of 7 W was achieved at 535 nm for 26 W of pump power [Lee06b].

Electrically pumped external cavity semiconductor disk lasers

A way of extending the great results achieved with optically pumped VECSELs to electrical pumping was demonstrated by Mooradian [Moo01] and the underlying concept was commercialized by Novalux as ”Novalux extended-cavity surface emitting laser”

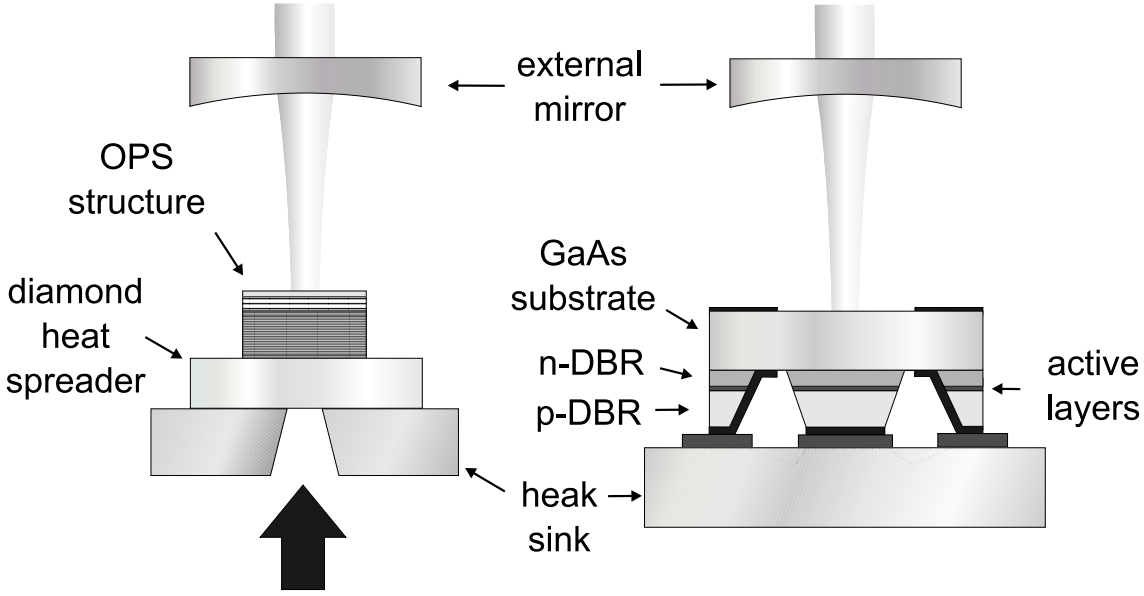

Figure 2.4: Schematic of an end-pumped OPS disk laser (left) and a NECSEL (right).

(*NECSEL*^{tm}). The idea of the NECSEL is to use a three mirror coupled cavity design (see Fig. 2.4 (right)). The semiconductor is similar to a VCSEL, but the top DBR is n-doped with a low doping concentration and only partially reflective, whereas the bottom DBR is high reflective and p-doped. However, NECSELs are limited in output power due to an inhomogeneous carrier distribution for large pump areas. In order to reach high output powers, arrays of several emitters can be used. Like OPS disk lasers, NECSELs can be frequency doubled with high efficiency. Visible lasers at 460 nm, 488 nm, and 532 nm were demonstrated by Shchegrov et al. [Shc03].

Pulsed pumping

Recently pulsed and quasi continuous wave pumping was proposed to overcome the thermal limitations of OPS disk lasers [Hem07]. Hempler *et al.* used a high power pulsed semiconductor laser, which operated at 905 nm to pump a GaInAsSb quantum well structure designed for emission at 2.3 µm. Square-shaped pulses with peak powers of 1.7 W were achieved this way. The excited pulses were slightly shorter than the pump pulses. The continuous wave output of the same structure was reported to be a factor of seven below. However, in contrast to conventional quasi continuous wave pumped edge emitting lasers, a thermally wavelength chirp was observed experimentally and a corresponding rapid temperature rise of 50 K to 60 K for a 180 ns pulse was estimated. The authors attributed the significant and fast heating of the device to the small pump volume.

2.4 Thermal management and power scalability

Probably the most crucial parameter that has to be considered for efficient operation of OPS disk lasers is the thermal management of the semiconductor structure, since the semiconductor bandgap, the length of the active medium, and the quasi-Fermi-Dirac distribution of the carriers are temperature dependent. OPS disk lasers react sensitive even to small increases of the gain medium temperature, which can occur despite the significant heat removal due to the thin disk concept.

Different approaches to reduce or at least limit the thermal load have been reported. The beneficial effects of in-well pumping and pulsed pumping on the quantum defect have been described above. Other methods cover the optimization of the heat removal.

Fig. 2.5 (left) shows a typical top emitter OPS structure on a heat sink. The main thermal resistance is induced by the substrate, which is much more bulky than the structure itself. For a bottom emitter structure (Fig. 2.5 (middle)) the layers are grown in reverse order on the substrate [Kuz99]. The Bragg mirror is directly bonded to the heat sink and the substrate is etched off subsequently. An etch stop layer between the gain region and the substrate protects the semiconductor during the etching process. In such a bottom emitter structure the thermal resistance is reduced significantly due to the absence of the substrate.

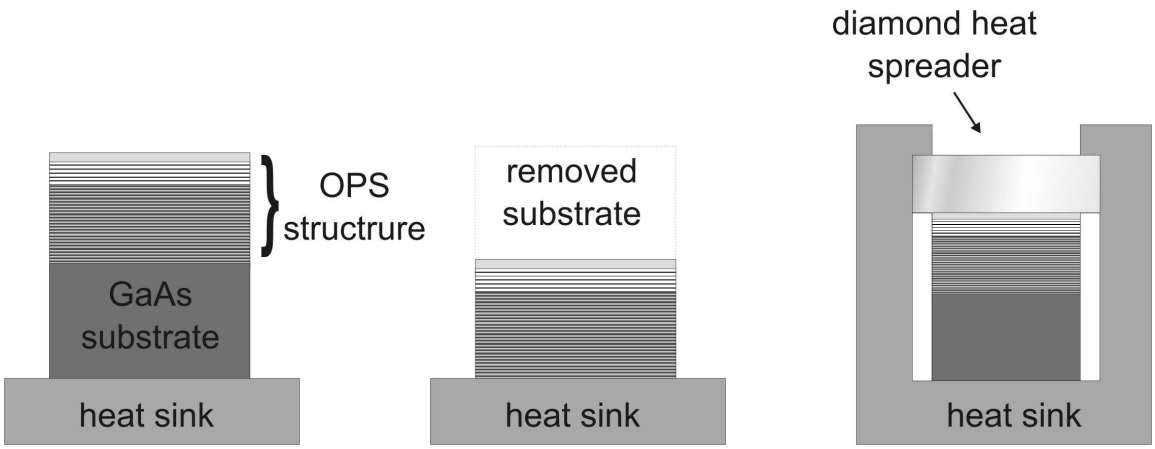

Figure 2.5: Schematic of a top emitter (left), a bottom emitter (middle) and a top emitter with a diamond heat spreader (right).

The heat can also be removed by applying an intracavity heat spreader (Fig. 2.5 (right)) [Alf02]. Such a heat spreader typically consists of diamond or sapphire and is bonded to the top of the semiconductor structure. Diamond and sapphire have a much higher thermal conductivity than the semiconductor materials of the DBR mirror (see. table 2.4) and accordingly the heat removal is more efficient. A theoretical treatment of the thermal

material	thermal conductivity κ ($\mathrm{Wm^{-1}\,K^{-1}}$)
GaAs	45
AlAs	90
diamond	2000
sapphire	44
copper	400
solder	~ 30

Table 2.1: Thermal conductivities of relevant materials for OPS disk lasers operating around 1.0 µm.

management for a heat spreader topped semiconductor via finite element analysis is given in [Kem06] and predicts superior performance in comparison with bottom emitter structures.

OPS disk lasers were shown to be power scalable with the pump spot size [Lut03]. Increasing the pump spot size reduces the thermal load per unit of area. However, for large pumped areas amplified spontaneous emission (ASE) arises and in-plane lasing with a resonator formed by the chip edges may occur [Bed05]. In-plane lasing can be avoided by roughing the edges or by changing the geometric shape of the semiconductor. ASE itself cannot be suppressed effciently, since the light is index guided in the epitaxial planes.

A power scaling scheme less sensitive to ASE is using a multi-chip cavity [Fan06], [Saa06b]. In this concept the total pumped area is distributed over several OPS chips positioned as active mirrors at different resonator positions. This way the thermal load per area can be reduced without increasing ASE losses.

2.5 Carrier dynamics, gain, and confinement

The OPS disk lasers presented in this thesis are barrier pumped and accordingly most of the electron-hole pairs are generated in the barriers. The intraband relaxation time of about 100 fs is much shorter than the carrier lifetime of $\sim 1-5$ ns and the resonator dependent photon lifetime [Gar07].

The carrier lifetime depends on the carrier concentration in the quantum wells. To approximate the carrier density, the radiative and nonradiative losses have to be considered. The respective loss mechanisms are spontaneous emission and Auger recombination. The carrier density dependence on these losses at a fixed temperature can be approximated by

$$\frac{N}{\tau(N)} = AN + BN^2 + CN^3 \tag{2.4}$$

where N is the carrier density, $\tau(N)$ is the carrier lifetime in the wells, and A, B, and C are constants. The physical interpretation of the individual terms is as follows. The first term accounts for defect recombination losses, which is negligible for semiconductors with very high optical quality. The quadratic term describes spontaneous emission and the cubic term accounts for nonradiative Auger recombination losses. Strained quantum wells have an increased electron-hole recombination time, because the radiative decay rate and the Auger rate are reduced due to a lower threshold carrier density.

The gain of OPS disk lasers is also carrier density dependent and is connected to it through the Fermi factor

$$f = f_c - f_v \tag{2.5}$$

where

$$f_c = \frac{1}{1 + exp(E_c - E_{F,c})/k_B T} \tag{2.6}$$

and

$$f_v = \frac{1}{1 + exp(E_v - E_{F,v})/k_B T} \tag{2.7}$$

are the Fermi-Dirac occupation numbers of the upper and lower laser level. Thus the Fermi factor corresponds to the population inversion at a given photon energy E_{ph}. The carrier density dependence is included in the Fermi energies in the conduction and valance band $E_{F,c}$ and $E_{F,v}$. Fig. 2.6 shows the energy level diagram for an optical transition with the photon energy

$$E_{ph} = E_{gap} + E_{e,1} + E_{h,1} + \frac{\hbar^2 k^2}{2m_e} + \frac{\hbar^2 k^2}{2m_h} \tag{2.8}$$

where E_{gap} is the quantum well bandgap energy, $E_{e,1}$ and $E_{h,1}$ are the confinement energies of the first bound states in the well, m_e and m_h are the effective masses of the electrons and holes, and k is the wave vector of the transition. The conduction and valence band are described using a parabolic approximation.

The subbands in the parabola on the right side of Fig. 2.6 vary with the thickness of the well. For a thinner well the separation between the subband increases, which results in a higher percentage of carriers occupying the lowest subband. Accordingly the inversion

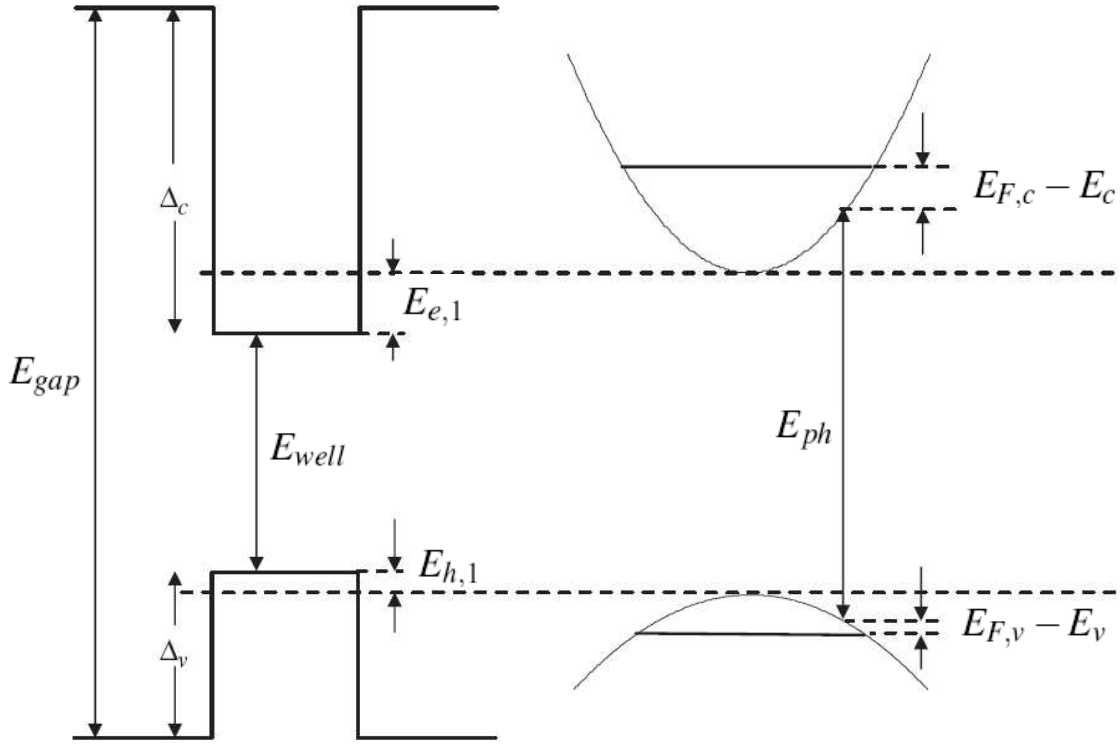

Figure 2.6: Energy level diagram of a quantum well transition. The denoted quantities determine the Fermi factor, which is proportional to the gain of the corresponding mode. The left side shows the band edge profile across a quantum well and on the right side the parabolic approximation of the conduction and valance band is sketched [Tro06].

and hence the Fermi factor increases.

The gain further depends on the distribution of the quantum wells in the RPG structure and is proportional to the longitudinal confinement factor given by

$$\Gamma_l = \sum_i |E(z_i)|^2 \tag{2.9}$$

where $E(z_i)$ is the electric field amplitude of the standing wave within the gain region at the position z_i of the i-th quantum well. The longitudinal confinement factor acts as a spectral filter [Kuz99]. Depending on the influence of the subcavity formed by the Bragg mirror and the semiconductor surface, the enhancement of the gain due to the resonant well positions and the strength of the spectral filter effect vary. The longitudinal confinement factor of an OPS disk laser is temperature dependent due to thermal expansion of the semiconductor structure.

3 Infrared characteristics

The OPS disk lasers presented in this thesis are designed for operation around 1050 nm since the desired wavelength for green display lasers is around 525 nm. The aim was to achieve high optical efficiencies for green output power in the sub-Watt regime.

In this chapter the compact laser setup and the operation characteristics at the fundamental wavelength are presented. The laser experiments were performed using a linear resonator similar to the one sketched in Fig. 3.1.

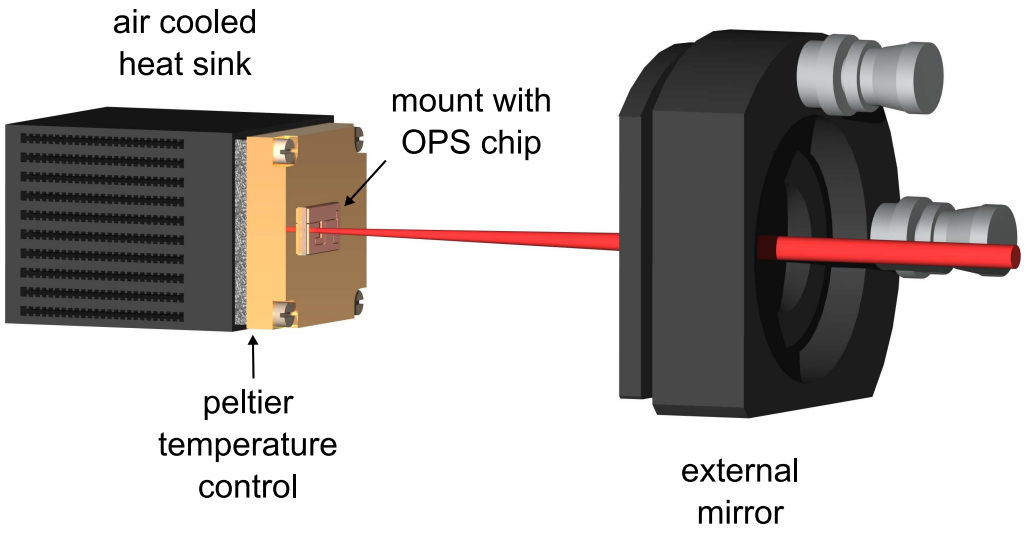

Figure 3.1: Schematic of the linear resonator setup.

3.1 Laser setup

3.1.1 The compact pump geometry

OPS disk lasers are conventionally pumped with a fiber coupled diode laser. For all experiments presented in this thesis, a different, more compact pump setup was used.

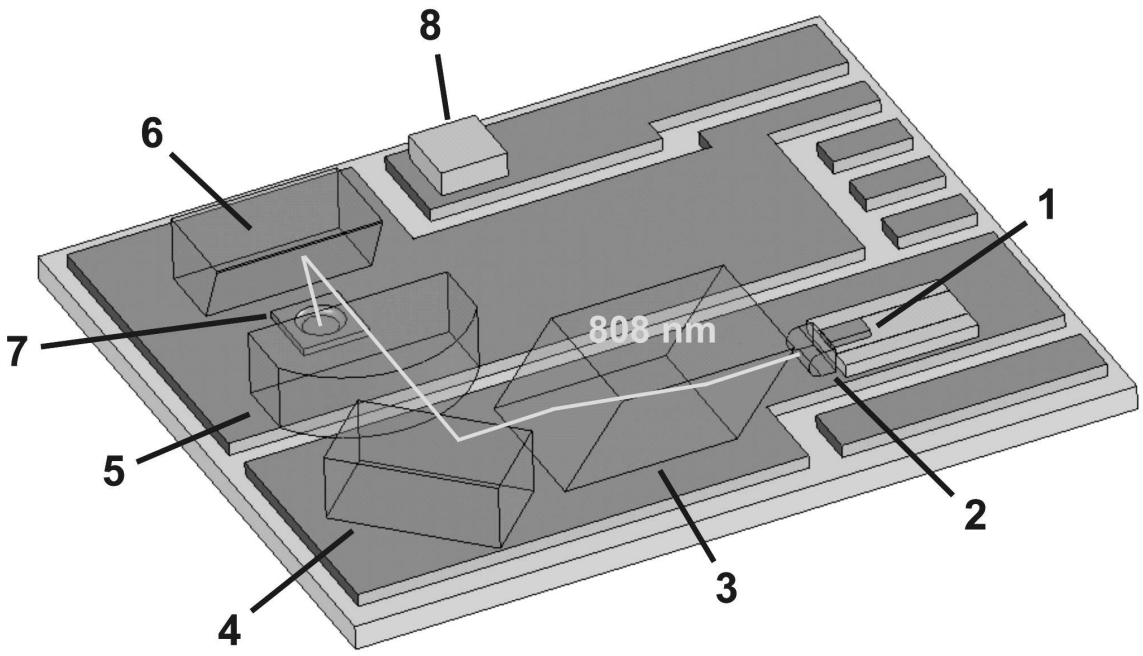

Figure 3.2: Setup of the pump unit. The pump beam is directed by micro optics to the gain region (Picture by courtesy of OSRAM Opto-Semiconductors GmbH).

The pump source, all optics required for beam guidance, and the semiconductor disk were mounted to a $9.5 \times 11.5\,\mathrm{mm}^2$ small plate. A schematic of this pump geometry and the micro-optics is shown in Fig. 3.2.

As pump source (1) a broad area laser diode emitting at 808 nm was used. Right behind this laser diode the beam was parallelized by a fast axis collimation lens (2). Then the beam was slightly altered by prism (3). A deflection prism (4) changed the direction of the beam by 90° to keep the pump setup compact. Next the beam was focussed by a lens (5) via a second deflection prism (6) onto the active region (7) under an angle of 45° with respect to the surface normal of the semiconductor. The temperature of the heat sink could be measured by a NTC thermistor (8). The semiconductor structure was attached to a mounting plate consisting of either direct bond copper (DBC) or aluminum nitride (AlN) (see right side of Figure 3.3). With a peltier element, which was applied under the plate, the temperature could be controlled accurately. The thermal load was removed by an air-cooled heat sink (see Figure 3.1).

The described pump setup not only was very compact, but also had the advantage, that the pump beam only had to be aligned once. However, once aligned, the pump spot was fixed in position and size.

Figure 3.3: Photographs of the pump unit. The right picture shows the pump unit on aluminum nitride (back) and direct bond copper (front), (Picture by courtesy of OSRAM Opto-Semiconductors GmbH).

3.1.2 Chip design

The experiments presented in this thesis were conducted with three different semiconductor chips. The choice of the chips was determined by availability rather than by their properties. Chip 1 had a more powerful pump diode and the pump spot was optimized for slightly higher output powers. The semiconductor was grown as bottom emitter. Chip 2 and 3 were designed for operation at lower powers. For reasons of compactness a deflection prism was added about 5 mm from the semiconductor surface (see Fig. 3.4). Both chips were grown as top emitters.

All gain media, that are presented in this thesis, were grown by OSRAM Opto Semiconductors GmbH and are optimized for emission around 1050 nm. The semiconductor chips were grown on gallium arsenide substrates by molecular organic vapor phase epitaxy (MOVPE) as described in section 2.1.

For the presented chips the Bragg mirror consisted of periodically distributed GaAs and AlAs layers. The respective refractive indices around 1 µm at room temperature are $n_{GaAs} = 3.50$ and $n_{AlAs} = 2.95$ [Tal95]. This high index contrast results in a reflectivity better than 99.9% at the laser wavelength for 30 periods of GaAs and AlAs quarter-wave layers.

The gain region consisted of InGaAs quantum wells, spaced by barrier layers of AlGaAs. The quantum wells were positioned at the antinodes of the intracavity standing wave

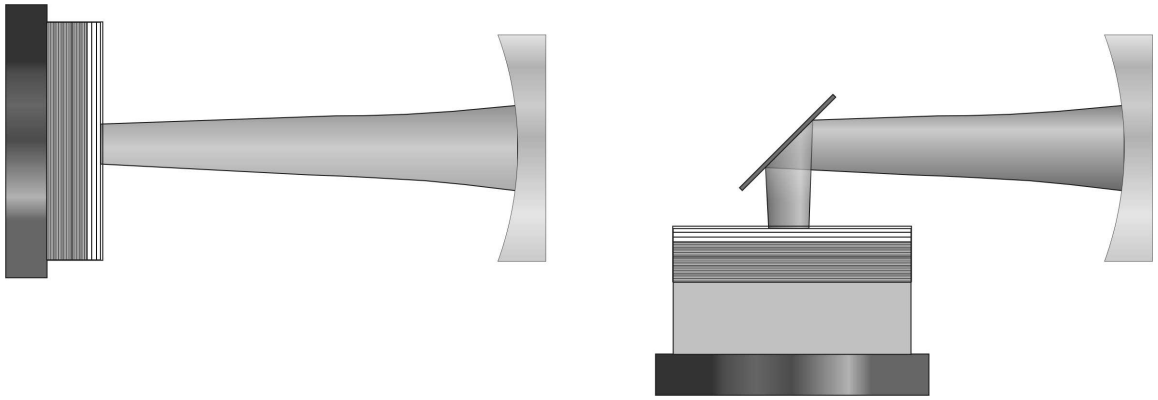

Figure 3.4: Chip 1 is a bottom emitter (left) and Chip 2 and 3 are top emitters with an additional deflection prism 5 mm from surface (right).

pattern to form a resonant periodic gain structure. GaAsP layers were added to the AlGaAs barriers for strain compensation. The semiconductor chip was soldered to a copper heat sink.

3.2 Luminescence

The luminescence of the pumped gain region was measured with a Fourier transform spectrometer (Bruker Equinox 55). With a $f = 80$ mm lens the emission near perpendicular to the surface was collected. The luminescence was measured in dependence of the temperature and the pump power. The resolution for these measurements was 1 nm. To account for small intensity fluctuations each curve was averaged over 20 scans.

Fig. 3.5 shows the luminescence spectra of chip 2 for different heat sink temperatures. The irradiated semiconductor exhibits a broad emission peak with 40 nm full width at half maximum (FWHM) around its design wavelength of 1050 nm. When the heat sink temperature is increased, this peak shifts to longer wavelengths with about 0.2 nm/K over the temperature range displayed. A second peak at 875 nm can be attributed to electron hole recombination within the barrier layers.

The shoulder on the left side of the main peak evidences the presence of light-hole recombination and states with higher energy. If the spectra were recorded at a position slightly behind the plane of the semiconductor, the shoulder would be expected to exhibit a smooth decay without ripples [Tro06]. Since the spectra presented in this section were recorded normal to the OPS chip, the emission was distorted by interference effects within the structure. The peaks around $950 - 1000$ nm correspond to the side lobes of the Bragg mirror reflectivity spectrum. An intrinsic spectral profile was not recordable with the given setup.

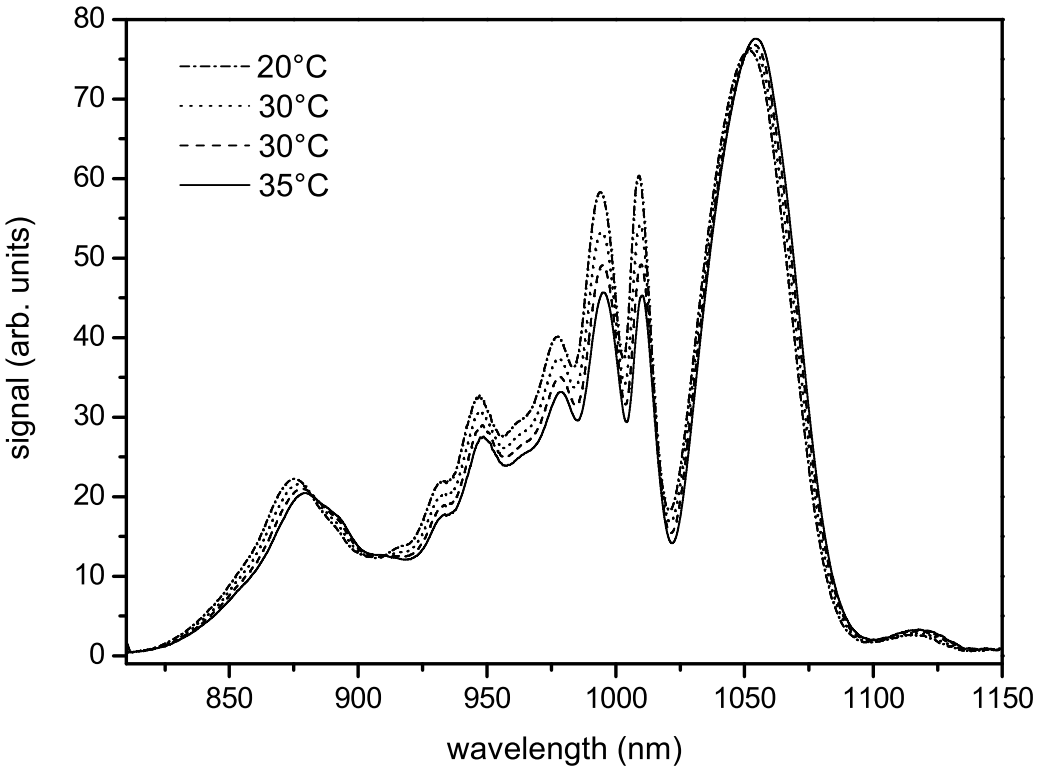

Figure 3.5: Luminescence spectrum of chip 2 in dependence of the temperature.

The dependence of the luminescence on the current of the pump diode and hence the absorbed pump power can be seen from Figure 3.6. The setup was the same as above and the heat sink temperature was kept constant at 25°C. It can be seen that the peak intensities do not increase linearly with the pump power. Instead the emission approaches a saturation. For increasing pump powers, the peak becomes broader, since more states are significantly occupied within the well. Like for the temperature dependent spectra a red shift was observed. Since the modulations resulting from the DBR spectrum are independent of the bandgap changes caused by temperature variations, the shift of these peaks provides information about the temperature of the semiconductor structure. Comparing the red shifts for the same peak from Fig. 3.5 and Fig. 3.6 yields 0.103 nm/K and 6.3 nm/W respectively. Accordingly the temperature of the active region rises by about 61 K per Watt of absorbed pump power.

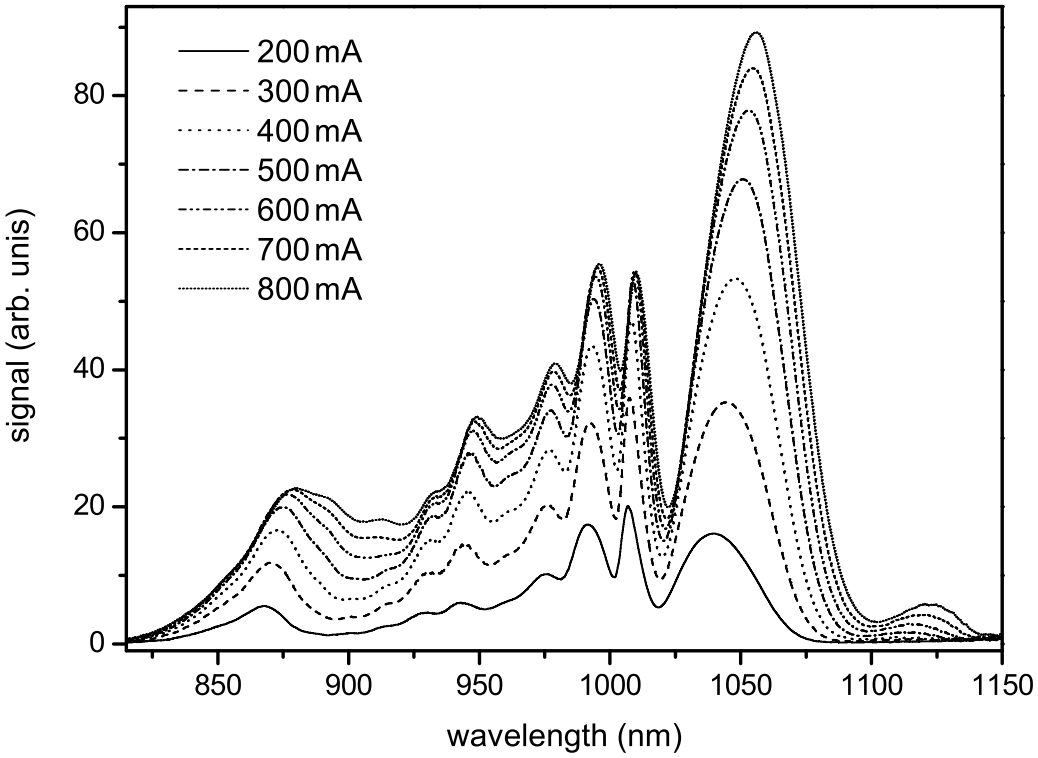

Figure 3.6: Luminescence spectrum of chip 2 in dependence of the pump current.

3.3 Laser experiments

The experimental setup for the laser experiments consisted of the compact pump module presented in section 3.1.1 in combination with semiconductor chip 2 and a 50 mm long hemispherical linear resonator. A curved mirror with $R = 50$ mm was used as output coupler. The pump diode had a maximum output power of 1.0 W at 808 nm for a pump current of 1.0 A. The laser threshold of the pump diode was 135 mA, which exhibited a maximum electrical to optical efficiency of about 50%. The circular pump spot on the active region had a diameter of about 80 µm. If not denoted differently, the heat sink temperature was kept at 25°C for all experiments.

3.3.1 Output power

In Fig. 3.7 the output power characteristics of the OPS disk laser are shown for external mirrors with different transmission coefficient T. The optimum transmission was found to be about $T = 1.2\%$. For this mirror a slope efficiency of $\eta_{slope} = 41.2\%$ was achieved. The maximum total optical conversion efficiency was $\eta = 34.9\%$. For a mirror with $T = 1.2\%$ the resonator was stable for lengths between 48.7 µm and 50.0 µm. The maximum output power of 218 mW was achieved for a 49.7 µm long resonator. The beam quality was measured to be near diffraction limited with $M^2 < 1.05$.

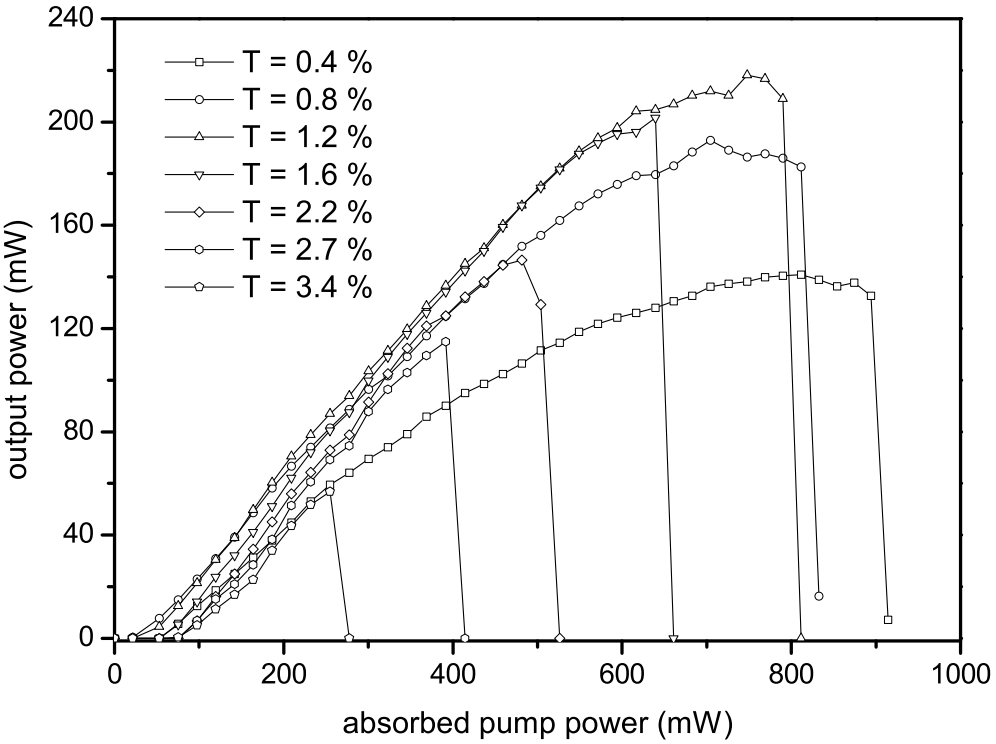

Figure 3.7: Infrared output power versus absorbed pump power for several output couplers with varying transmission for chip 2 and a 50 mm linear resonator.

Thermal runaway

As can be seen from Figures 3.7 and 3.8, the laser output power rolls over at a certain pump power. This effect is called thermal runaway or thermal rollover.

From the onset of laser oscillation, the gain of the semiconductor equals the losses of the cavity. For higher semiconductor temperatures the carrier density required to achieve this gain rises. The higher carrier density and the higher temperature lead to a higher Auger recombination rate. This actually results in a higher thermal load per absorbed pump power. Since the gain spectra shift to longer wavelengths with higher temperatures, the longitudinal enhancement factor peak is tuned away from the intrinsic gain peak. Hence the effective gain is reduced and the carrier density will rise further. An avalanche process starts at a critical pump power, the temperature rises uncontrollable and the laser switches off.

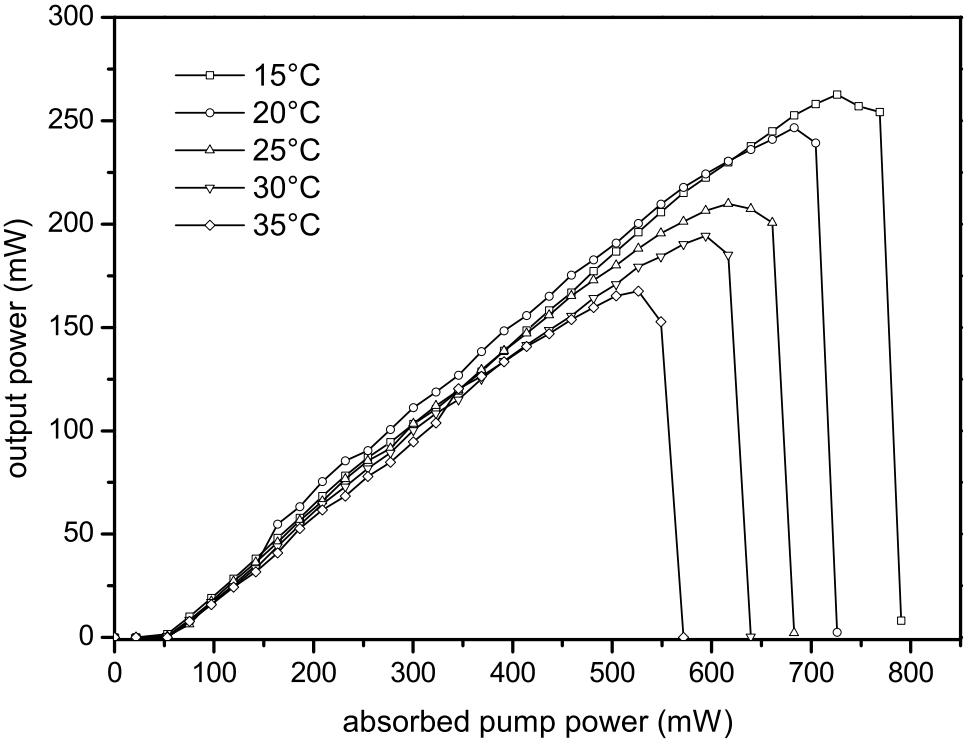

Figure 3.8: Infrared output power versus absorbed pump power for different heat sink temperatures.

The critical pump power can be increased by using an optimized thermal management and a cavity with very low losses. From Fig. 3.7 it can be seen that the thermal rollover sets in at higher pump powers for lower transmission coefficients and hence for lower round trip losses. Fig. 3.8 shows the dependence of the output power on the temperature. Five curves are shown for heat sink temperatures ranging from 15°C to 35°C. The slope efficiency is about the same for all curves with a slight increase for lower heat sink

temperatures. However, the thermal rollover sets in at different pump powers. This shows the importance of the thermal management for OPS disk lasers.

3.3.2 Polarization

The polarization of the infrared output was measured for the linear resonator setup using a prism polarizer. Without adding polarization selective elements like brewster windows to the cavity, the OPS disk laser was linearly polarized with a contrast of better than 100:1 for all samples subject to this thesis. In all cases the polarization was parallel to one of the edges of the semiconductor. According to the chip processing the polarization was either parallel or perpendicular to the $[110]$ axis of the gain material, which intrinsically has a cubic structure.

The deviation from the intuitively expected unpolarized output can be explained by a breakdown of the circular symmetry of the resonator caused by a small gain dichroism between the $[110]$ and $[1\bar{1}0]$ crystal axes. For an antimonide based OPS disk laser a gain dichroism in the quantum wells of about 10 % was measured by Garnache *et al.*, which caused the laser to oscillate preferably linearly polarized along the $[110]$ axis [Gar06].

The gain anisotropy is probably induced by mechanical stress within the quantum wells. However the polarization selectivity of the material is not very strong and therefore the polarization can be changed by intracavity elements without significant losses of output power. The detailed origin of the polarization behavior of OPS disk lasers is yet unknown.

3.3.3 Laser spectra

The laser spectra were measured with the Fourier transform spectrometer. The intensity of the signal was reduced by neutral density filters to comply with the sensitivity of the Si-detector over the desired wavelength range. Intuitively single mode operation or at least a small emission linewidth is expected for OPS disk lasers, because the resonant periodic gain structure with its quantum wells at the antinodes of the intracavity standing wave should act as a wavelength selective element. However, the laser spectra displayed in Fig. 3.9 indicate, that the emission linewidth of the OPS disk laser is rather broad, if no additional wavelength filter is applied to the cavity.

One possible reason for the broad emission linewidth is that the quantum wells have different temperatures, because there is more pump power absorbed in the regions close to the surface of the chip than in the deeper lying layers. Another linewidth enhancing effect in OPS disk lasers is inhomogeneous broadening due to growth fluctuations. Small variations of the position, the width or the composition of the quantum wells can result in fluctuations of the emission wavelength over the gain region.

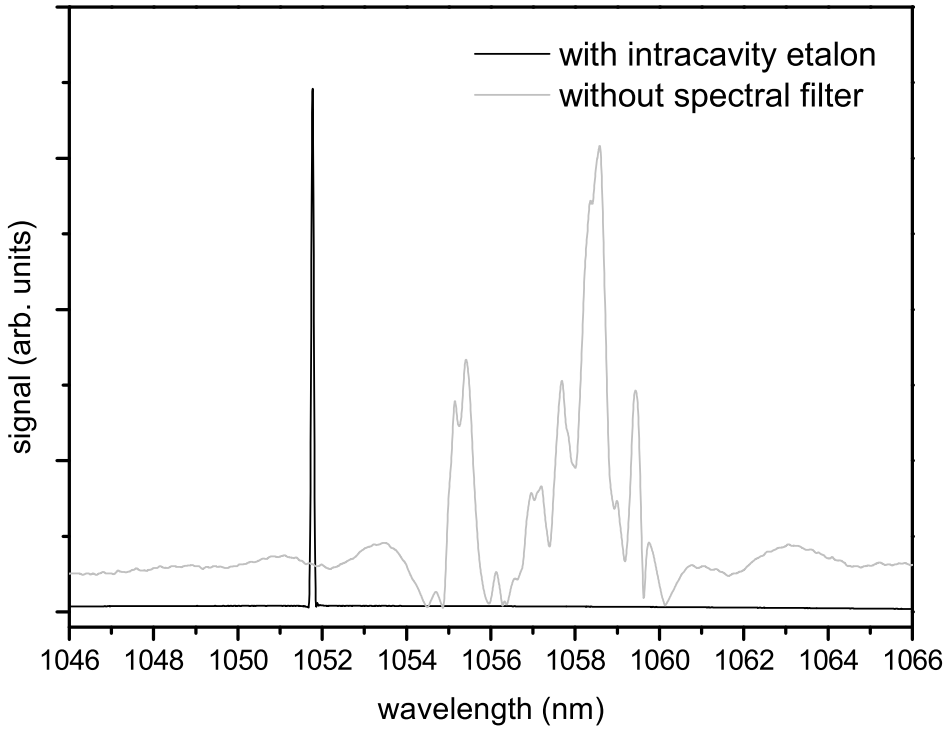

Figure 3.9: Laser spectra with and without spectral filtering for chip 1. An intracavity etalon reduces the linewidth to below 0.1 nm. The signal of the narrow peak was much more intense and is normalized for comparison.

The laser emission spectrum can be controlled by adding spectral filters like a birefringent filter under Brewster's angle or an etalon to the cavity. With spectral filtering narrow linewidths below 0.1 nm can be achieved easily (see Fig. 3.9).

In contrast to solid state laser materials, the peak positions of the semiconductor gain spectrum strongly depend on the temperature and the carrier density. Therefore, the laser spectra vary for different pump powers and heat sink temperatures. Fig. 3.10 (a) shows the laser spectra for different pump powers. For increasing pump powers a shift to longer wavelengths is observed, which results from the higher temperatures in the gain region and from the higher carrier densities in the quantum wells.

Thermal expansion of the gain region typically causes detuning of the longitudinal confinement factor to longer wavelength by about 0.1 nm/K and the temperature dependent gain profile of the semiconductor material shifts by about 0.3 nm/K [Tro04]. The presented OPS disk lasers exhibited a thermal shift of about 0.2 nm/K, indicating a mixture

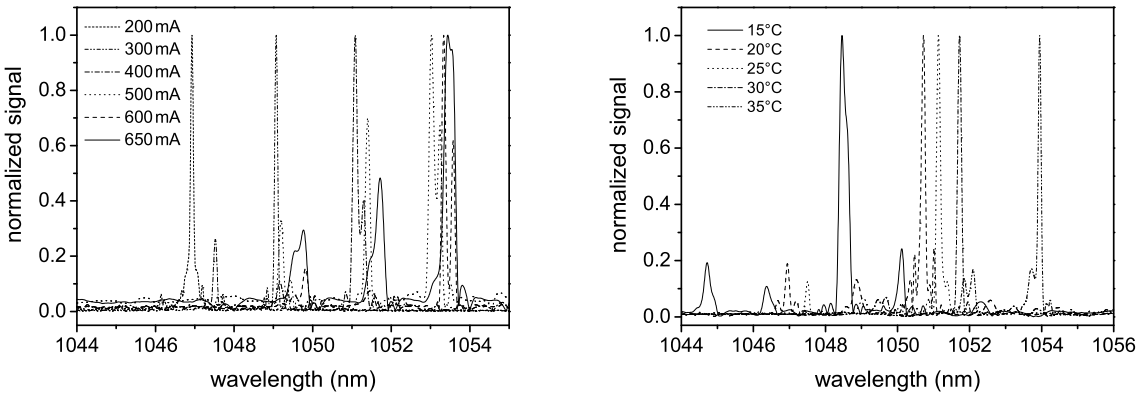

(a) pump power dependant

(b) temperature dependant

Figure 3.10: Laser spectra (a) for different pump currents and (b) for different heat sink temperatures.

of both effects. Fig. 3.10 (b) shows how the laser wavelength depends on the heat sink temperature. Furthermore, an etalon effect can be seen, which results from the 80 µm thick substrate of chip 2. The position of the etalon transmission shifts slightly with increasing temperature due to thermal expansion of the substrate.

3.3.4 Tunability and dual-wavelength operation

The broad luminescence peak around the laser wavelength and the spectral shifting of laser emission with temperature suggest, that a significant tuning range can be covered with the presented OPS disk laser, even though the gain region was not optimized for broad tunability.

A 30 µm thick etalon was added as tuning element to the linear cavity with 1.2 % output mirror transmission presented in section 3.3.1. The emission wavelength was monitored using a fiber coupled spectrometer with fast reaction time (Ocean Optics USB2000) and a Fourier transform spectrometer with high resolution. The pump current was 600 mA corresponding to an absorbed pump power of about 525 mW.

The OPS disk laser was continuously tunable with an output power of more than 10 mW over a range of more than 22 nm from 1041.0 nm to 1063.5 nm by tilting the etalon. The corresponding laser spectra are shown in Fig. 3.11 (a) and were recorded with the Fourier transform spectrometer. The distance between the peaks has no physical background, but was chosen for convenience corresponding to the resolution of the fiber spectrometer. It is noticeable, that the signals for wavelengths between 1044 nm and 1058 nm have about the same intensity. The corresponding output powers varied be-

tween 78 mW and 93 mW. The total signal for the four wavelengths around 1050 nm is distributed between two neighboring peaks.

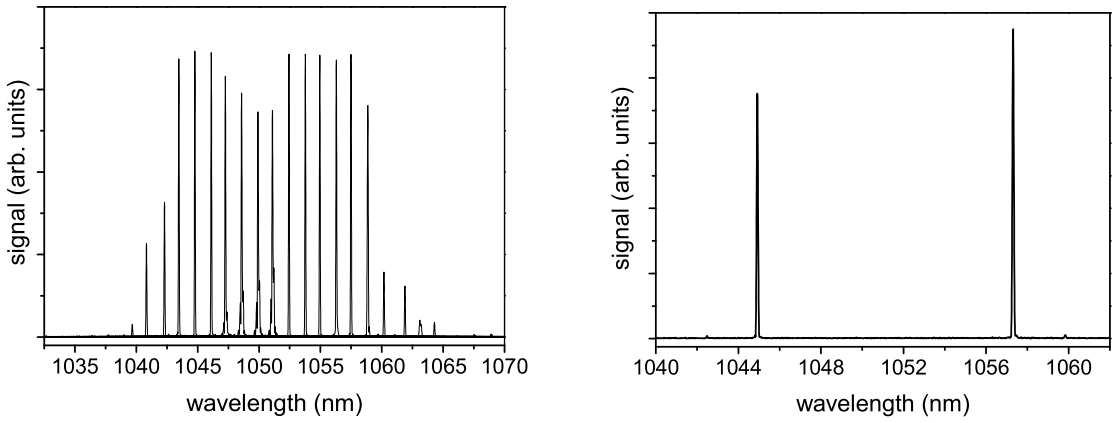

(a) tunability (b) dual-wavelength operation

Figure 3.11: (a) Tunability in a linear resonator with a tilted etalon. An output power around (85 ± 8) mW could be achieved over a continuous tuning range of 15 nm. (b) Dual-wavelength operation of a linear resonator comprising an etalon. In this configuration an output power of 72 mW was achieved.

Another interesting feature of the broad gain peak is the possibility to achieve simultaneous operation at two wavelengths. In a simple configuration using a linear resonator and an etalon, stable dual-wavelength operation was achieved with 72 mW output power (see Fig. 3.11 (b)). However, modulating the output power was not possible. As the pump power was varied, the shift of the gain peak resulted in a preference of one of the emission wavelength. The concomitance of the two wavelengths was verified by sum frequency generation experiments (see section 5.6).

3.3.5 Loss measurements

OPS disk lasers are low gain lasers and respond very sensitive to cavity losses. Efficient performance requires high quality fabricated semiconductors, e. g. low scattering losses can only be achieved for high surface quality. For intracavity frequency doubling the resonator losses should be particularly low to achieve high intracavity powers.

A method to determine the internal resonator losses requires to measure the slope efficiencies for several output couplers with different transmission coefficients [Cai88]. This method has the advantage to be independent of the laser threshold, which is hard to determine accurately. Furthermore, it is relatively insensitive to errors of the single measurements [Fre04].

For a diode pumped continuous wave laser a dependence of the slope efficiency η_{slope} on the internal resonator losses can be derived from standard rate equations [Sve98]. Using a small loss approximation, the internal resonator losses per pass γ_i can be calculated from

$$\eta_{slope} = \eta_{pump} \frac{\lambda_P}{\lambda_L} \frac{T}{T + 2\gamma_i} \tag{3.1}$$

where η_{pump} is the pump efficiency, λ_P and λ_L are the wavelengths of the pump and the laser respectively, and T is output mirror transmission. A more general form of equation 3.1 can be found by including an additional factor for losses due to excited state absorption (ESA)

$$\eta_{slope} = \eta_{pump} \frac{\lambda_P}{\lambda_L} \left(1 - \frac{\sigma_{ESA}}{\sigma_{em}}\right) \frac{T}{T + 2\gamma_i} \tag{3.2}$$

where σ_{ESA} is the cross section for the excited state absorption and σ_{em} is the emission cross section. In the presence of ESA the theoretical maximum slope efficiency is reduced by a factor equal to the ratio of the effective gain cross section $\sigma_{eff} = \sigma_{em} - \sigma_{ESA}$ to the emission cross section σ_{em}. The maximum slope efficiency that can be achieved in the absence of passive losses is then given by

$$\eta_0 = \eta_{pump} \frac{\lambda_P}{\lambda_L} \frac{\sigma_{eff}}{\sigma_{em}} \tag{3.3}$$

and the inversion of equation 3.2 yields

$$\frac{1}{\eta_{slope}} = \frac{1}{\eta_0} \left(1 + 2\gamma_i \frac{1}{T}\right) \tag{3.4}$$

It exists a linear relationship between the inverted slope efficiency η_{slope}^{-1} and the inverted output mirror transmission T^{-1}. This dependence is displayed in the so-called Caird-Plot shown in Fig. 3.12. The maximum achievable slope efficiency η_0 can be calculated as the inversion of the intersection of the linear fit with the vertical axis.

Fig. 3.12 shows three Caird-Plots for a hemispherical linear resonator in which the output couplers have a radius of curvature of 100 mm. The triangles are data for chip 1 and the squares and circles are data for chip 2 with and without an etalon in the resonator respectively. The grey lines indicate the linear fits. All measurements were similar to those displayed in Fig. 3.7.

The internal losses γ_i were calculated as described above. The internal losses of the resonators were found to be 0.125 % for chip 1 and 0.19 % for chip 2 respectively. Adding

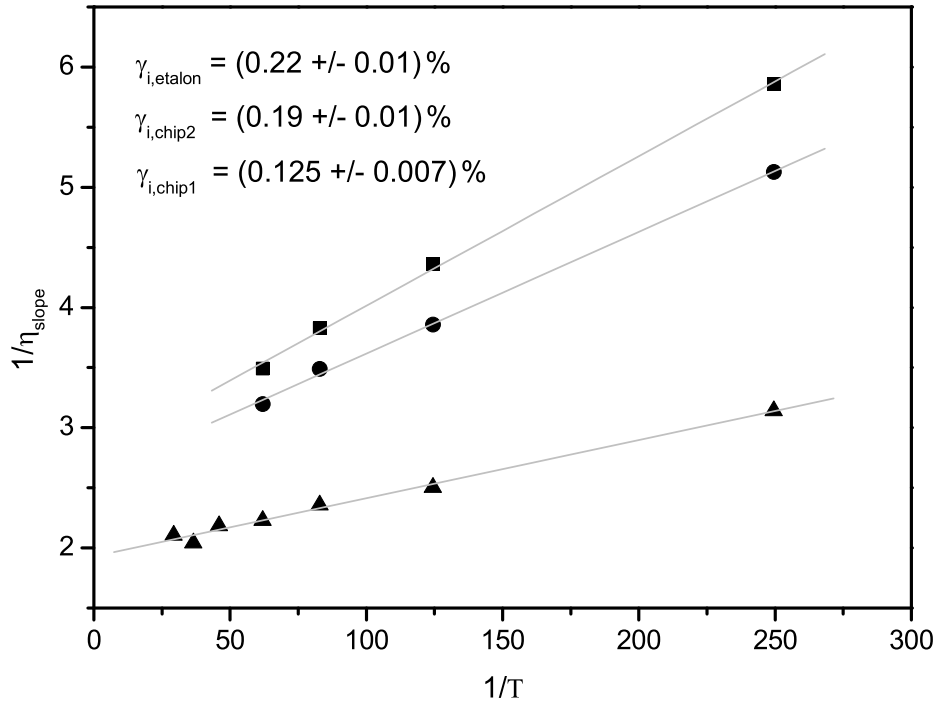

Figure 3.12: Caird-Plot for intracavity losses of a 100 mm linear resonator containing chip 1 (triangles), chip 2 (circles), and chip 2 with an intracavity etalon (squares).

an etalon to the latter cavity resulted in slightly higher internal losses of 0.22 %. The higher internal losses for the resonator comprising chip 2 are supposedly at least partially caused by the additional deflection prism (see Fig. 3.4). No data for high mirror transmission could be taken for chip 2, because the output powers were too small or no laser action was achievable at all.

4 Frequency doubling

Shortly after the presentation of the first laser in 1960 by Maiman [Mai60], the nonlinear effect of frequency doubling, also known as second harmonic generation (SHG), was described by Franken *et al.* [Fra61]. This nonlinear optical mechanism allows the generation of a wave with twice the optical frequency of an input wave. Today SHG is a common method to access new wavelengths. In this chapter the theoretical background for the frequency conversion experiments presented in chapters 5-7 is given. For a more detailed description of frequency doubling the readers are referred to [Boy03] and [Sut96].

4.1 Nonlinear optics

In contrast to linear optics, where the optical properties of a traversed medium stay unchanged and the frequency of the light is constant, in nonlinear optics some optical properties of an illuminated material, like the refractive index or the absorption coefficient, can change due to the incident field, and the frequency of the electromagnetic wave can be altered. Electric fields of intense light can modify the optical properties of crystals and other dielectric materials. If the electric field is particularly high, the dielectric response of the material becomes nonlinear dependent upon the strength of the electric field. Sufficiently high intensities to observe these modifications are typically only achieved for laser light.

4.1.1 The nonlinear polarization

A convincing way to describe the nonlinear generation of new frequencies is to look at the polarization wave created by an electromagnetic wave in a medium. An electric field applied to a dielectric medium induces a separation of bound charges and hence creates an electric dipole moment. The average electric dipole moment per unit volume defines the electric polarization $\mathbf{P}$ of the medium. For low intensities the polarization depends linear on the electric field of the incident wave:

$$\mathbf{P}(\mathbf{r},t) = \varepsilon_0 \chi^{(1)} \mathbf{E}(\mathbf{r},t) \tag{4.1}$$

Here ε_0 is the permittivity of free space and $\chi^{(1)}$ is a tensor for the dielectric susceptibility. For the calculation of this polarization wave, permanent dipoles can be neglected, since they will not oscillate at optical frequencies. The variables $\mathbf{r}$ and t are left out in the following for clarity.

If the electric field of laser radiation is particularly high, i. e. on the order of the atomic field, the polarization of the medium responds nonlinearly and equation 4.1 has to be generalized. To account for the nonlinear response, the polarization amplitude is expanded by a power series in the electric field $\mathbf{E}$. In component notation it is given by

$$P_i = \chi_{ij}^{(1)} E_j + \chi_{ijk}^{(2)} E_j E_k + \chi_{ijkl}^{(3)} E_j E_k E_l + ... \tag{4.2}$$

where the subscripts i, j, k, and l refer to the cartesian components of the fields. $\chi^{(2)}$, $\chi^{(3)}$ and so on are the nonlinear dielectric susceptibilities (see section 4.1.2). In the case of a plane monochromatic wave the subscripts from equation 4.2 are negligible.

The electric field strength of a monochromatic laser beam can be written as

$$\mathbf{E} = E e^{-i\omega t} + c.c. \tag{4.3}$$

where $c.c.$ denotes the complex conjugate. Substituting this expression in equation 4.2 yields

$$P^{(2)} = \chi^{(2)}(E^2 e^{-2\omega t} + c.c.) + 2\chi^{(2)} E E^* \tag{4.4}$$

for the second order polarization for the case of a plane monochromatic wave. This equation shows, that in a medium for which the second order susceptibility is nonzero, the created nonlinear polarization contains a contribution of the frequency 2ω. Accordingly, the electromagnetic radiation generated by the polarization wave contains a contribution at the second harmonic frequency of the incident laser beam.

If the incident wave consists of two distinct frequency components, the electrical field is represented by

$$\mathbf{E} = E_1 e^{-i\omega_1 t} + E_2 e^{-i\omega_2 t} + c.c. \tag{4.5}$$

and the second order contribution to the nonlinear polarization becomes

$$\begin{aligned} P^{(2)} = \chi^{(2)}(&E_1^2 e^{-2i\omega_1 t} + E_2^2 e^{-2i\omega_2 t} + 2E_1 E_2 e^{-i(\omega_1+\omega_2)t} \\ &+2E_1 E_2^* e^{-i(\omega_1-\omega_2)t} + c.c.) + 2\chi^{(2)}(E_1 E_1^* + E_2 E_2^*) \end{aligned} \tag{4.6}$$

The oscillation amplitudes of the different frequency components of this polarization wave are given by

$$\begin{aligned} P(2\omega_1) &= \chi^{(2)}E_1^2 && (SHG) \\ P(2\omega_1) &= \chi^{(2)}E_2^2 && (SHG) \\ P(\omega_1+\omega_2) &= \chi^{(2)}E_1E_2 && (SFG) \\ P(\omega_1-\omega_2) &= \chi^{(2)}E_1E_2^* && (DFG) \\ P(0) &= 2\chi^{(2)}(E_1E_1^*+E_2E_2^*) && (OR) \end{aligned} \tag{4.7}$$

Each of these expressions describes a different second order nonlinear process for an incident wave with two distinct frequency components. The physical processes are second harmonic generation (SHG), sum frequency generation (SFG), difference frequency generation (DFG), and optical rectification (OR). The quantities of the complex conjugate components of the nonlinear polarization are not taken into account here, since they do not yield additional information. A schematic process diagram for second harmonic generation and sum frequency generation is shown in Fig. 4.1.

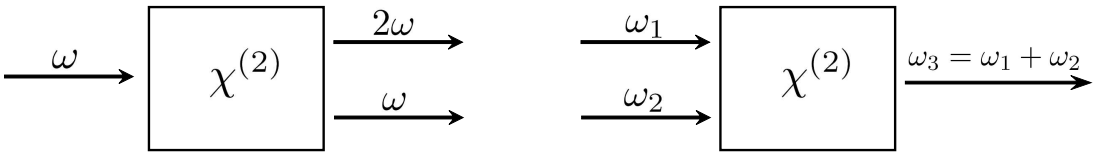

Figure 4.1: Schematic of second harmonic generation (left) and sum frequency generation (right).

So far only the effects of the second order nonlinear polarization have been considered. Higher orders can generate other frequencies. Third harmonic generation, self phase modulation, and stimulated Raman scattering are examples for third order nonlinear effects. However, these processes require even higher intensities to achieve appreciable efficiencies. A detailed description is given in [Boy03].

4.1.2 The nonlinear optical susceptibility

The optical susceptibility χ is a dimensionless material constant for the dielectric response of an optical medium. $\chi^{(1)}$ in equation 4.2 is known as linear optical susceptibility whereas the higher orders are nonlinear optical susceptibilities. In general, $\chi^{(n)}$ is a tensor of rank $n+1$. In this thesis only second order effects, namely SHG and SFG, will be considered and $\chi^{(2)}$ is a third rank tensor with 27 compounds.

Second order nonlinear effects exist only in acentric crystals, since $\chi^{(2)} = 0$ for crystals with a symmetry center and for isotropic media. Accordingly, no second order nonlinear

effects can be observed in gases, liquids, crystals with inversion symmetry, glasses, and other amorphous solids. In contrast, third order effects can take place in any crystalline or isotropic material.

The description of the nonlinear optical susceptibility given in this section is only valid for the assumption of a dispersionless and lossless material. If dispersion and losses are considered, the nonlinear susceptibility becomes a complex quantity, which couples the complex amplitude of the electric field to the complex amplitude of the polarization.

To calculate the efficiencies for frequency conversion, so-called nonlinear coefficients are used. They are defined as

$$d_{ijk} = \frac{1}{2}\chi^{(2)}_{ijk} \tag{4.8}$$

where i,j, and k are the directions in space. If Kleinman symmetry is obeyed for the nonlinear crystal, d_{ijk} is symmetric in its last two indices and the notation can be simplified:

$$\begin{array}{rcl} \mathbf{jk} & \rightarrow & \mathbf{l} \\ 11 & \rightarrow & 1 \\ 22 & \rightarrow & 2 \\ 33 & \rightarrow & 3 \\ 23,32 & \rightarrow & 4 \\ 31,13 & \rightarrow & 5 \\ 12,21 & \rightarrow & 6 \end{array} \tag{4.9}$$

This notation reduces the nonlinear susceptibility tensor to a 3×6 matrix. For frequency doubling this simplification is always valid, since two of the involved frequencies are identical. The second order polarization can be calculated from this matrix by

$$\begin{pmatrix} P^{(2)}_{3,x} \\ P^{(2)}_{3,y} \\ P^{(2)}_{3,z} \end{pmatrix} = 2 \begin{bmatrix} d_{11} & d_{12} & d_{13} & d_{14} & d_{15} & d_{16} \\ d_{21} & d_{22} & d_{23} & d_{24} & d_{25} & d_{26} \\ d_{31} & d_{32} & d_{33} & d_{34} & d_{35} & d_{36} \end{bmatrix} \begin{pmatrix} E_{1,x}E_{2,x} \\ E_{1,y}E_{2,y} \\ E_{1,z}E_{2,z} \\ E_{1,y}E_{2,z} + E_{2,y}E_{1,z} \\ E_{1,x}E_{2,z} + E_{2,x}E_{1,z} \\ E_{1,x}E_{2,y} + E_{2,x}E_{1,y} \end{pmatrix} \tag{4.10}$$

If Kleinman symmetry is given, only 10 of the tensor elements are independent [Kle62]. Tables for the 3×6 matrices of various symmetry classes can be found in [Sut96].

4.2 Phase matching

From equation 4.7 it can be seen, that four different frequency components are generated by the second order polarization. For a typical laser setup only one of these frequencies can accumulate significant intensity while passing the nonlinear crystal. The dominating conversion mechanism then satisfies a so-called phase matching condition. In the majority of cases only one of the frequencies complies with this condition. This section describes phase matching of the second harmonic frequency.

Within the nonlinear crystal the fundamental wave and the polarization wave produced by it propagate with the same velocity, which is determined by the index of refraction n_ω. The polarization wave induces a second harmonic wave, which travels independently at a velocity determined by $n_{2\omega}$. Due to dispersion of the nonlinear crystal, n_ω is dissimilar from $n_{2\omega}$ and the fundamental and second harmonic waves propagate at different velocities. As a second harmonic wave generated at the front side of the nonlinear crystal travels along the fundamental wave, and thereby also along the polarization wave, the relative phase between the waves increases linearly. Second harmonic waves are generated at every position of the polarization wave. The created waves interfere with all waves that have been created previously. Whether this interference is constructive or destructive depends on the relative phase and is subject to a periodic change.

Constructive and destructive interference correspond to a positive or a negative power flow from the fundamental to the second harmonic. The propagation distance it takes for the two waves to have a phase difference of π, is the so-called coherence length

$$l_c = \frac{\lambda_\omega}{4(n_{2\omega} - n_\omega)} \tag{4.11}$$

which also defines the period of the sign change for the power flow from the fundamental wave to the second harmonic. According to this periodic power flow, the second harmonic wave reaches an intensity maximum at l_c behind the front end of the crystal. Another l_c further the intensity is zero again and the periodic rise and fall starts again. Typical full-cycle period lengths for visible and near infrared light are in the range of a few micrometers to tens of micrometers.

The periodic change of the power flow direction can be avoided by either inhibiting the dispersion (birefringent phase matching) or by flipping the sign of the nonlinear coefficient every other coherent length via domain inversion in the nonlinear crystal (quasi phase matching).

4.2.1 Birefringent phase matching

The phase mismatch between the fundamental and the second harmonic wave is usually expressed using the difference between the wave vectors Δk. For efficient nonlinear frequency conversion the two waves have to remain in phase. Therefore, the condition for the wave vectors is

$$\Delta k = |2\mathbf{k}_\omega - \mathbf{k}_{2\omega}| = \left| \frac{4\pi(n_\omega - n_{2\omega})}{\lambda_\omega} \right| = 0 \tag{4.12}$$

where $\mathbf{k}_\omega$ and $\mathbf{k}_{2\omega}$ are the wave vectors of the fundamental and the second harmonic wave respectively. From equation 4.12 it is obvious that $n_\omega = n_{2\omega}$ has to be accomplished.

Birefringent phase matching, which is also called index matching, uses the natural birefringence of anisotropic crystals to elude dispersion. For these types of crystals the refractive index depends on the electric field polarization of the beam for a given direction of propagation. The refractive index varies with the orientation of the polarization towards an optical axis. If the polarization is perpendicular to the optical axis, the light is subject to the ordinary refractive index n_o. Parallel polarization is subject to the extraordinary refractive index n_e. All other orientations are partially perpendicular and partially parallel to the optical axis and the combined index of refraction depends on the angle θ between the polarization direction and the optical axis

$$n_e(\theta) = \frac{n_o n_e}{\sqrt{n_o^2 sin^2(\theta) + n_e^2 cos^2(\theta)}} \tag{4.13}$$

The optical axis is defined as a direction of propagation for which the refractive index is independent of the polarization. Propagation along this axis implies that the polarization is always oriented perpendicularly to it and hence only n_o occurs. Birefringent crystals are either uniaxial or biaxial, meaning they have either one or two optical axes. The denotation n_o and n_e is only used for uniaxial crystals. In the case of biaxial crystals all three crystal axes have different refractive indices and it is conventional to take $n_z > n_y > n_x$.

It is impossible to have $n_\omega = n_{2\omega}$ if the fundamental and the second harmonic wave are polarized in the same direction. However, if the waves are polarized orthogonally to each other (type-I phase matching) or if the fundamental wave has ordinary and extraordinary components and the second harmonic wave is polarized under 45° to it (type-II phase matching), $\Delta k = 0$ can be achieved.

Fig. 4.2 schematically shows the refractive indices n_o and n_e in dependence of θ given by 4.13 for the frequently encountered case of an uniaxial crystal. Both indices are given for the fundamental (black lines) and the second harmonic wave (gray lines). The

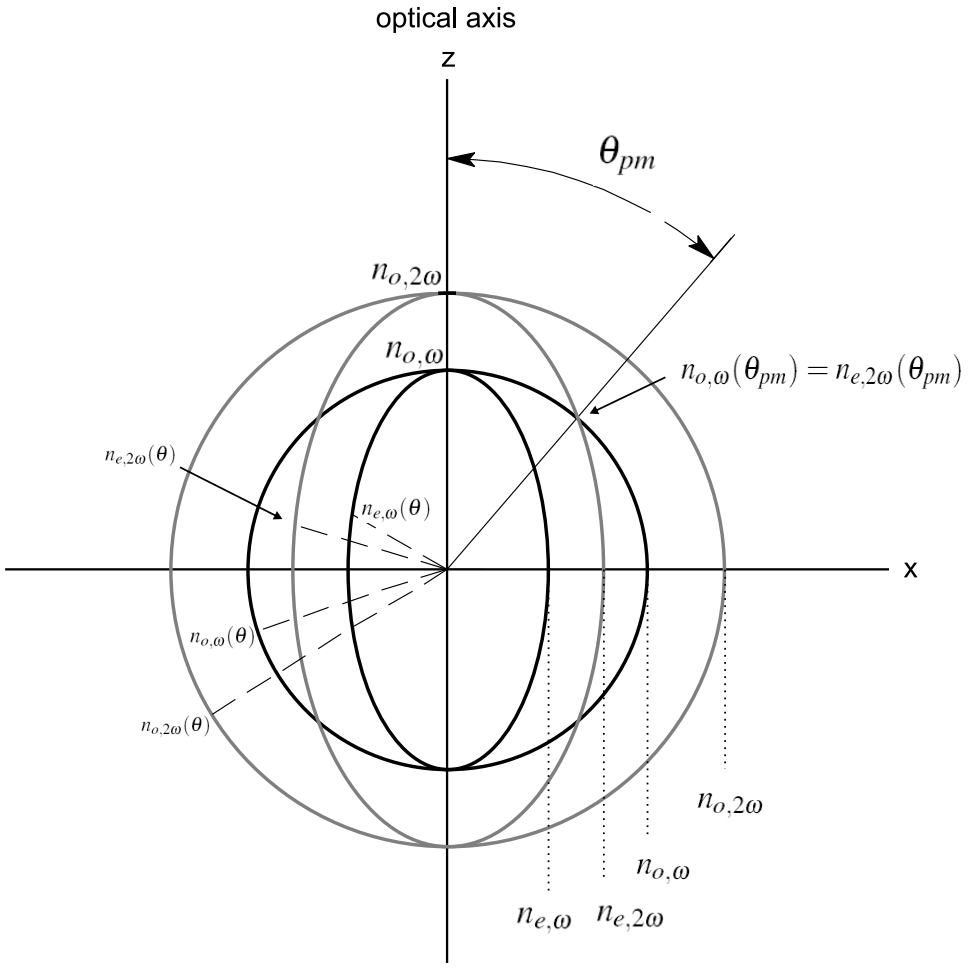

Figure 4.2: Schematic of the angular dependent refractive indices of an uniaxial crystal.

combined index $n_e(\theta)$ varies between n_o and n_e to form an ellipse. The ordinary indices are displayed as circles. The ellipse for $n_{2\omega}$ and the circle for n_ω overlap at the phase matching angle θ_{pm} at which the phase matching condition from equation 4.12 is obeyed. For a beam propagating along the axis defined by θ_{pm}, the incident wave and the orthogonally polarized second harmonic wave experience the same refractive index, if the polarization of either the fundamental wave (ooe, see below) or the second harmonic wave (eeo) is oriented perpendicularly to the optical axis.

Nonlinear crystals are typically cut normal to θ_{pm} for convenience. For normal incidence of the fundamental wave, such crystal only has to be rotated around this axis to match the required orientation. This technique to obtain $\Delta k = 0$ is called critical phase matching, because it is relatively sensitive to misalignment of the phase matching angle.

For negative uniaxial crystals ($n_o > n_e$) the phase matching angle can be calculated from the relations

$$\begin{aligned} n_e(2\omega,\theta_{pm}) &= n_o(\omega) && Type-I \quad (ooe) \\ n_e(2\omega,\theta_{pm}) &= \tfrac{1}{2}\left[n_e(\omega,\theta_{pm})+n_o(\omega)\right] && Type-II \quad (eoe) \end{aligned} \tag{4.14}$$

and for positive uniaxial crystals ($n_e > n_o$) from

$$\begin{aligned} n_o(2\omega) &= n_e(\omega,\theta_{pm}) && Type-I \quad (eeo) \\ n_o(2\omega) &= \tfrac{1}{2}\left[n_o(\omega)+n_e(\omega,\theta_{pm})\right] && Type-II \quad (oeo) \end{aligned} \tag{4.15}$$

Using the relations 4.14 and 4.15 in 4.13, the phase matching angle for uniaxial crystal and type-I phase matching can be calculated as

$$\begin{aligned} sin^2(\theta_{pm}) &= \frac{(n_{e,2\omega})^2}{(n_{o,\omega})^2}\left[\frac{(n_{o,2\omega})^2-(n_{o,\omega})^2}{(n_{o,2\omega})^2-(n_{e,2\omega})^2}\right] && (ooe) \\ sin^2(\theta_{pm}) &= \frac{(n_{e,\omega})^2}{(n_{o,2\omega})^2}\left[\frac{(n_{o,2\omega})^2-(n_{o,\omega})^2}{(n_{e,\omega})^2-(n_{o,\omega})^2}\right] && (eeo) \end{aligned} \tag{4.16}$$

and for type-II phase matching as

$$\begin{aligned} \tfrac{1}{2}n_{o,\omega} &= \frac{(n_{o,2\omega})}{\left(1+\left[\frac{(n_{o,2\omega})^2}{(n_{e,2\omega})^2}-1\right]sin^2(\theta_{pm})\right)^{\frac{1}{2}}} - \frac{\frac{1}{2}(n_{o,\omega})}{\left(1+\left[\frac{(n_{o,\omega})^2}{(n_{e,\omega})^2}-1\right]sin^2(\theta_{pm})\right)^{\frac{1}{2}}} && (eoe) \\ sin^2(\theta_{pm}) &= \frac{4n_{o,2\omega}(n_{e,\omega})^2(n_{o,2\omega}-n_{o,\omega})}{(2n_{o,2\omega}-n_{o,\omega})\left[(n_{e,\omega})^2-(n_{o,\omega})^2\right]} && (oeo) \end{aligned} \tag{4.17}$$

where the indices of refraction are calculated from the respective Sellmeier equations. For some cases of type-II phase matching θ_{pm} has to be calculated numerically since no analytical solutions can be obtained [Sut96].

All considerations above are limited to uniaxial crystals. The situation for biaxial crystals, where all three crystal axes have different refractive indices, is more complex. A detailed description of phase matching in biaxial crystals is given in [Hob67].

Besides the phase matching angle, the phase mismatch depends on the crystal temperature and the spectral width of the laser beam. These dependencies can be given by a Taylor series around $\Delta k = 0$

$$\Delta k(\theta,\varphi,T,\lambda) = \left.\frac{\partial(\Delta k)}{\partial\theta}\right|_{\theta_{pm}} \delta\theta + \left.\frac{\partial(\Delta k)}{\partial\varphi}\right|_{\varphi_{pm}} \delta\varphi + \left.\frac{\partial(\Delta k)}{\partial T}\right|_{T_{pm}} \delta T + \left.\frac{\partial(\Delta k)}{\partial\lambda}\right|_{\lambda_{pm}} \delta\lambda \tag{4.18}$$

where φ gives the angle of the propagating beam to the x-axis of the crystal in polar coordinates. The conversion efficiency in dependence of the phase mismatch follows a sinc^2-function around $\Delta k = 0$. The spectral, temperature, and angular acceptances are defined as the FWHM of this curve. Tables for the acceptances of the most common nonlinear crystals can be found in [Dmi99].

4.2.2 Poynting vector walk-off

For propagation of a laser beam in an anisotropic material system the wave vector **k** and the energy flow given by the Poynting vector **S** can diverge slightly. This effect is known as Poynting vector walk-off or spatial walk-off. From Maxwell's equations one finds, that the electric displacement field **D**, the electric field **E**, and the wave vector **k** lie within the same plane. The magnetic field **H** points in a direction normal to this plane. Since the Poynting vector **S** is defined as

$$\mathbf{S} = \mathbf{E} \times \mathbf{H} \tag{4.19}$$

it lies within the plane defined by **D**, **E**, and **k**. Equation 4.19 also indicates that **S** is perpendicular to **E**, whereas **k** is perpendicular to **E**. In anisotropic media **D** and **E** usually are not parallel, because the dielectric tensor ε does not degenerate to a scalar like for isotropic media. Thus **S** and **k** also diverge.

In the case of birefringent phase matched frequency doubling the fundamental and the frequency doubled wave have collinear wave vectors. However, if the phase matching angle θ_{pm} is other than 90°, the directions of the Poynting vectors are different due to the dissimilar electric field directions. Accordingly the two waves diverge and the angle between their Poynting vectors is known as the walk-off angle.

For type-I phase matching in a negative uniaxial crystal, the walk-off angle is given by

$$tan(\rho) = \frac{(n_{o,\omega})^2}{2}\left[\frac{1}{(n_{e,2\omega})^2} - \frac{1}{(n_{o,2\omega})^2}\right] sin(2\theta) \tag{4.20}$$

Typically these angles are small and ($tan(\rho) \approx \rho$).

The Poynting vector walk-off limits the interaction length of the fundamental beam and the second harmonic light in a nonlinear crystal leading to a reduced conversion efficiency. At a distance of about

$$l_a = \frac{a}{\rho} \tag{4.21}$$

where a is the beam diameter, the beams completely separate. For weakly focussed Gaussian beams this distance, which is called the aperture length, is given by [Boy65]

$$l_a = \frac{w_0\sqrt{\pi}}{\rho} \approx 1.77\frac{w_0}{\rho} \tag{4.22}$$

where w_0 is the radius of the fundamental beam. If the nonlinear crystal length l excesses l_a the relationship between length and second harmonic power changes from quadratic to linear. As another negative consequence, the walk-off can broaden the beam profile in one direction which reduces the beam quality.

Walk-off can be avoided by using a noncritical phase matching scheme where **S** and **k** are parallel (see sections below) or by walk-off compensation. In the latter case the spatial walk-off is compensated by an array of paired nonlinear crystals of opposite walk-off directions [Zon03a, Zon03b].

4.2.3 Noncritical phase matching

If for $\theta_{pm} = 90^\circ$ the refractive indices $n_{o,\omega}$ and $n_{e,2\omega}$ are almost equal and if their respective shift due to temperature variation is different, it is possible to accomplish the phase matching condition $\Delta k = 0$ by temperature tuning of the nonlinear crystal. This method is called noncritical phase matching, because it is relatively insensitive to angular misalignment of the involved beams. The phase mismatch depends on a much smaller, quadratic term for the angular misalignment $\delta\theta$ in contrast to the linear dependence for critical phase matching.

Another advantage is the absence of Poynting vector walk-off at $\theta_{pm} = 90^\circ$. Accordingly, limitations due to beam divergence between fundamental and second harmonic wave are strongly reduced. This allows for tighter focussing in the nonlinear crystal.

A major drawback of noncritical phase matching is that the required crystal temperatures are typically far above room temperature and stabilized crystal ovens have to be used. The nonlinear phase matching temperature for frequency doubling of a Nd:YAG laser at 1064 nm with lithium triborate for example is 148°C [Uka90].

4.2.4 Quasi-phase matching

Quasi phase matching (QPM) is a technique to achieve a net energy flow from the fundamental wave to the second harmonic by either a modulation of the linear refractive

index or by modulating the magnitude of the nonlinearity. This method was first proposed by Armstrong *et al.* [Arm62], shortly after the first demonstration of SHG. It can be understood as an periodical reset of the accumulated phase mismatch. The best results are achieved, if this reset takes place after one coherence length (see equation 4.11) corresponding to a period of $\Lambda = 2l_c$ (1st order QPM), but a reversal every $3\,l_c$ (3rd order), every $5\,l_c$ (5th order) and so on also results in a significant increase of the net power flow. In comparison with birefringent phase matching, the efficiency of m-th order QPM frequency doubling is reduced to

$$d_{eff,qpm} = \frac{2}{m\pi} d_{eff,pm} \tag{4.23}$$

for the same propagation direction. In Fig. 4.3 the conversion efficiency with respect to the propagated crystal length is shown for (a) phase matched, (b) 1st order, (c) 3rd order, and (d) 5th order QPM frequency doubling. The SHG efficiency without any phase matching is also shown for comparison (e).

Even though the effective nonlinear coefficient is reduced in comparison with birefringent phase matching for a given crystal orientation, QPM often can yield higher conversion efficiencies. For QPM the involved beams can be collinear and have the same polarization, which allows one to use the highest available nonlinear coefficient of the nonlinear optical material. In the case of lithium niobate the maximum nonlinear coefficient is a factor of ≈ 5.8 higher than for the best birefringent phase matchable propagation direction. 1st order QPM along this direction results in an overall increase of d_{eff} by a factor of ≈ 3.7.

For many nonlinear crystals, QPM gives access to spectral ranges, where no birefringent phase matching is possible. Furthermore, cubic crystals, that sometimes have large nonlinear coefficients but exhibit no birefringence, can be used for QPM.

Since the introduction of electrical field poling in the early 1990s [Yam93], quasi phase matching has been subject to an increased interest. Lithographic processing techniques allow for domain lengths short enough for 1st order QPM in the visible spectral range. Ferroelectric crystals like lithium niobate ($LiNbO_3$, LN), lithium tantalate ($LiTaO_3$, LT) and potassium titanyl phosphate ($KTiOPO_4$, KTP) can be poled with high precision. A good review of QPM nonlinear interactions is given in [Bye97] and [Fej92].

4.3 Intracavity doubling

As stated above, frequency doubling requires high intensities to be efficient. Therefore, often pulsed lasers with high peak powers are used. For SHG of continuous wave lasers with relatively low powers, one can make use of the much higher intracavity powers by positioning the nonlinear crystal inside the laser resonator.

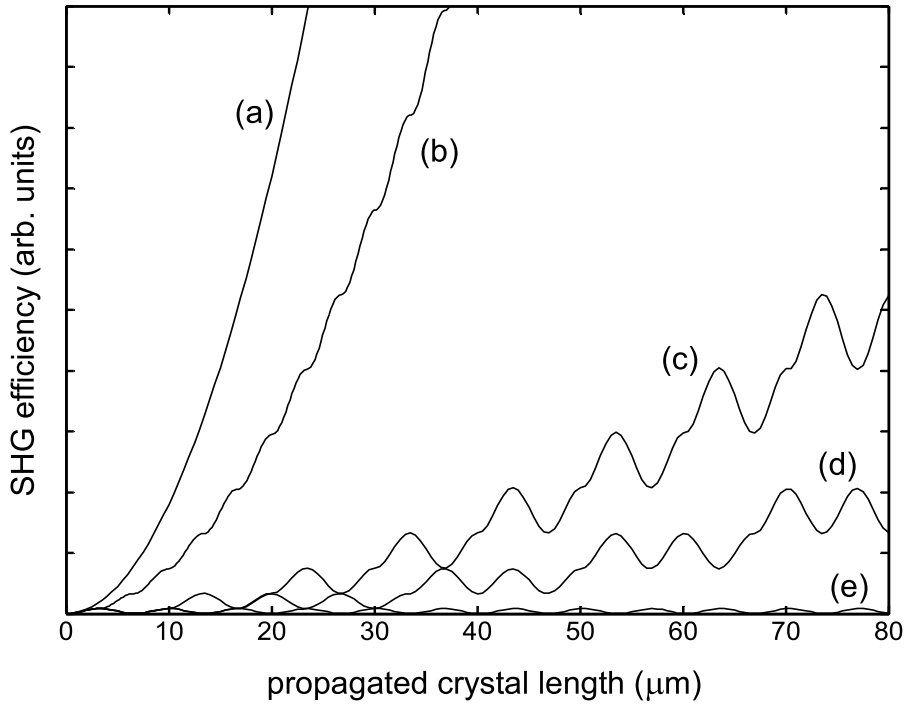

Figure 4.3: Conversion efficiencies for quasi-phase matching. Comparison of (b) 1st, (c) 3rd, and (d) 5th order QPM with (a) birefringent phase matching. Without any phase matching, the SHG power oscillates close to zero (e).

The nonlinear crystal within the laser resonator acts as an output coupler and the generated beam exits the resonator via a dichroic mirror with high reflectivity at the fundamental wavelength and high transmissions at the harmonic wavelength. The outcoupling rate depends on the conversion efficiency and therefore also on the intracavity power. The highest conversion efficiency is achieved, if the outcoupling rate via SHG equals the optimum outcoupling of the resonator for operation on the fundamental wave. For most lasers this rate is on the order of only a few percent. High conversion efficiencies can be achieved by intracavity doubling, even if the converted power per single pass is quite low. The unconverted power stays within the resonator and therefore passes the crystal again. The outcoupling rate via the nonlinear crystal is given by

$$T_{nl} = KI_{\omega} \tag{4.24}$$

where I_{ω} is the fundamental intensity and K is the nonlinear coupling given by

$$K = 2\left(\frac{\mu_0}{\varepsilon_0}\right)^{\frac{1}{2}} \frac{\omega^2 d_{eff}^2 l^2}{n_\omega^2 n_{2\omega} c^2} \frac{sin(\Delta kl/2)}{\Delta kl/2} \tag{4.25}$$

Optimum nonlinear coupling is obtained for [Smi70]

$$K_{opt} = \frac{\gamma_i}{I_{sat}} \tag{4.26}$$

where I_{sat} is the saturation intensity, which depends on the gain material and the fundamental wavelength, and γ_i is the total internal loss of the resonator at the fundamental wave for one round trip.

For $\Delta k = 0$ and $n_\omega = n_{2\omega}$ the optimum length of the nonlinear crystal can be calculated from equations 4.25 and 4.26 to

$$l_{opt} = \left[\left(\frac{\varepsilon_0}{\mu_0}\right)^{\frac{1}{2}} \frac{n_\omega^3 c^2}{2\omega^2}\right]^{\frac{1}{2}} \frac{1}{d_{eff}} \left(\frac{\gamma_i}{I_{sat}}\right)^{\frac{1}{2}} \tag{4.27}$$

4.4 Selection of nonlinear crystals

A main part of this thesis is devoted to finding the optimum nonlinear crystal to meet the desired requirements in efficiency, compactness, beam quality, and price. There are several different crystals available commercially and the selection is often a sophisticated process. The choice of the nonlinear crystal for a particular laser setup depends on various crystal parameters and has great effects on power and brilliance of the emitted laser beam. In this section the most important properties of nonlinear crystals are briefly described and discussed.

Transparency

The most straightforward criteria for a nonlinear crystal to be suitable for a particular system is its transparency for the concerned wavelengths or wavelength ranges. This involves the fundamental wavelength as well as the harmonic. Lack of transparent nonlinear optical materials can be a problem especially when ultraviolet or mid- to far-infrared radiation is involved. If the transparency is well below 100 %, linear absorption causes objectionable losses. For intracavity doubling the transmissivity is a particularly sensitive parameter, because the crystal is passed many times and therefore the losses accumulate massively. Absorption not only leads to losses, but also generates a thermal load in the crystal, which can disturb the phase matching, create a thermal lens that changes the resonator properties or even might result in crystal damage.

It is possible, that a transparent crystal becomes partially absorbent at very high intensities or for irradiance with light of short wavelengths. This behavior is refered to as photodarkening. Well-known examples are grey tracking in potassium titanyl phosphate [Bou99] and green induced infrared absorption in lithium niobate or lithium tantalate [Bat98].

Dispersion and birefringence

As described in section 4.2, only crystals for which any kind of phase matching is achievable are adequate for frequency doubling. The possibility to obtain phase matching depends on the dispersion and the birefringence of the nonlinear material. Birefringent phase matching is only achievable over a certain spectral range by varying the orientation of the optical axis. Noncritical phase matching is impossible for many crystals.

Potential for periodical poling

Quasi phase matching is accessible even in cases where no birefringent phase matching can be achieved. It is limited by the shortest domain length that can be fabricated. The oldest method for producing quasi phase matching crystals is stacking of thin plates. However, at wavelengths in the visible the required poling periods are on the order of a few micrometers and can only be achieved by ferroelectric domain inversion poling. This technique generates a periodic reversal of the sign for the nonlinear coefficient along the crystal by application of strong electric fields to patterned electrodes on the crystal surface. Only ferroelectric materials with a small coercive field are suited to be fabricated this way. Typical examples are lithium niobate($LiNbO_3$), lithium tantalate ($LiTaO_3$) and potassium titanyl phosphate ($KTiOPO_4$).

Effective nonlinear coefficient

For efficient frequency conversion a high effective nonlinear coefficient d_{eff} is desired. The dependance of the second harmonic intensity on d_{eff} is quadratic for a single pass. d_{eff} depends on the nonlinear tensor and the crystal orientation, which in most cases is dictated by the phase matching configuration. In periodically poled materials the crystal orientation can be chosen freely and d_{eff} can be much higher for the same material as in the case of birefringent phase matching. The nonlinear coefficient is of particular importance, if the optical intensities of the fundamental wave are low and the outcoupling rate via SHG is far from saturation.

Tolerances towards laser parameters and alignment

Especially for systems that are needed to be unsensitive and mechanically stable, which is the case for many industrial applications, it is important to have some tolerances in the alignment to guarantee stable operation over long time scales. The intrinsic tolerances of nonlinear crystals are the angular, spectral, and temperature acceptances. If the laser system is subject to a surrounding with varying temperatures, the crystal temperature might fluctuate. Modulation of the fundamental intensity or absorption in the nonlinear crystal also cause a change of temperature. Under these conditions a high temperature acceptance is desired. Some lasers, such as OPS disk lasers, have broad gain spectra. For nonlinear crystals that have a spectral acceptance much smaller than the gain bandwidth, these lasers tend to avoid the conversion losses by changing to a different operation wavelength in the case of intracavity doubling. Lasers with a broad linewidth or with a drifting emission wavelength thus often require crystals with large spectral acceptances. For easy positioning of the crystal a good angular acceptance is of interest.

Walk-off angle

Nonlinear crystals with a high walk-off angle suffer from two negative effects. First, the walk-off angle limits the interaction length of the fundamental wave with the second harmonic. This limits the usable crystal length. Second, it reduces the beam quality. The effects of a high walk-off in combination with a curved end mirror can be seen from Fig. 5.8. For quasi phase matched crystals the propagation direction often is chosen to be along an optical axis and no walk-off occurs. Spatial walk-off is also avoided by using noncritical phase matching.

Damage threshold

Especially when short pulses with high peak powers are involved, the damage threshold of all optical elements along the beam propagation should be high. This is particularly important for the nonlinear crystal, because it is typically positioned at a beam waist where the intensities are exceedingly high. The damage threshold has to be considered for the coatings of the nonlinear crystal as well. For the relative low powers presented in this thesis this feature is uncritical.

Crystal dimensions

The most important dimension of a nonlinear crystal is its length, since the conversion efficiency responds quadratic to it. However, longer crystals also have negative effects like higher losses due to absorption or scattering. Furthermore, the optimum of the

crystal depends on the Rayleigh length of the focus and the walk-off limited nonlinear interaction length. For intracavity frequency doubling the optimum length can be calculated from equation 4.27, if the limiting effects other than nonlinear outcoupling are negligible. An exact calculation of the optimum crystal length often is inaccurate due to unknown parameters and thus testing different lengths experimentally might be more reasonable.

The aperture of the crystal becomes critical if the beam diameters are very large, like it is the case for many high intensity lasers, or if an array of beams is guided through the same crystal. The maximum dimensions of most nonlinear materials are limited by the growth mechanism. For ferroelectrically poled materials the thickness is typically limited to $< 1\,\mathrm{mm}$.

Available crystal qualities and chemical stability

Not every crystalline material can be grown at the same quality. Some crystals are inhomogeneous or have unwanted inclusions. In many cases crystals, that have been grown for the first time only recently and which are not well studied, are not available at good optical quality and reasonable dimensions. The chemical stability should also be considered, because some crystals tend to change their optical properties over time, at high temperatures or are hygroscopic. Moreover, the deposition of high- or anti-reflective coatings on the crystal's surfaces should be uncomplicated and stable.

Price

If at some point the developed laser setup is actually going into mass production, the price of the crystals becomes an important factor. Some crystals like KTP or LBO are grown in amounts of many tons per year and hence are available at low prices. Other crystals are still rare, expensive and only available by specialized manufacturers. Especially for low cost products in volume markets, the price of the nonlinear crystal significantly influences the overall costs of the laser system.

The choice of the nonlinear crystals often is a trade-off between the various parameters above and is highly dependent on the respective laser system. For the setups presented in this thesis, lithium triborate (LBO), bismuth borate (BiBO), potassium titanyl phosphate (KTP), and periodically poled lithium niobate (PPLN) were used. A detailed description of these materials and the corresponding experimental results are given in chapters 5 and 6.

5 Frequency doubling with LBO, BiBO, and KTP

The OPS disk lasers presented in this thesis operate at relatively low powers. To achieve high efficiencies for green emission in this power regime, optimized nonlinear conversion is required. High conversion efficiencies are not only important, because of the output power, but are also needed for fast power modulation. Therefore, it is of high importance to find the optimum nonlinear optical material. In this chapter frequency doubling experiments with type I phase matched LBO and BiBO as well as with type II phase matched KTP are presented. Experiments with periodically poled lithium niobate crystals will be discussed in the next chapter. If not denoted different, chip 3 was used for all frequency doubling experiments.

5.1 Crystal properties

5.1.1 Potassium titanyl phosphate ($KTiOPO_4$)

Potassium titanyl phosphate (KTP) was first synthesized in 1890 by Ouvrard. 1976 Zumsteg *et al.* discovered its great properties as a nonlinear optical material [Zum76]. Today, KTP is a well established nonlinear crystal and a standard material for SHG of neodymium doped lasers.

KTP has a biaxial structure with the point group symmetry mm2. The lattice constants are $a = 12.814\,\text{Å}$, $b = 6.404\,\text{Å}$ and $c = 10.616\,\text{Å}$. The structure consists of TiO_6 octahedra and PO_4 tetrahedra with the K^+ ions weakly bonded to both of them. The octahedra are distorted and linked to each other at two corners to form TiO_6 chains. A displacement of the Ti atoms from the center of the octahedra results in alternating long and short Ti-O bond lengths along these chains, causing a net $[001]$-directed polarization within the crystal, and giving rise to the large nonlinearities observed in this material.

The transparency of KTP ranges from 350 nm to 4500 nm, however the transmission is strongly reduced for wavelengths longer than 2500 nm. Critical phase matching is only possible for wavelengths above 994 nm and accordingly cannot be achieved for SHG to the blue spectral range.

KTP provides a rather high nonlinear optical coefficient of ($\sim 3.3\,\mathrm{pm/V}$), a broad thermal acceptance ($\sim 25\,\mathrm{K{\cdot}cm}$), and a small walk-off angle ($\sim 1\,\mathrm{mrad}$). Due to a high production volume, KTP can be obtained at relatively low costs. KTP can be grown by hydrothermal and flux techniques and is non-hygroscopic. Sellmeier coefficients for KTP can be found in [Kat02].

Another advantage of KTP is its low coercive field, which allows for high quality electric field poling. For quasi phase matched frequency conversion, the high nonlinear coefficient d_{33} can be used and the spectral range from blue to ultraviolet can be accessed. PPKTP already has been applied for SHG of OPS disk lasers to the blue [Raf03].

KTP is the most common nonlinear optical material for frequency doubling of pulsed and continuous wave lasers to the green. The unusually large temperature acceptance and the high damage threshold are advantageous for conversion of pulses with high energies. Other applications are optical parametric oscillators and low loss wave-guides [Bie89].

At 1050 nm KTP can be phase matched by using either type I or type II configurations. For the present work the more efficient type II phase matching was chosen.

5.1.2 Lithium triborate (LiB_3O_5)

In the late 1980s lithium triborate (LBO) was recognized as a nonlinear optical crystal by Chen *et al.* [Che89]. Like other boron-oxygen compounds, LBO offers transparency far into the ultraviolet spectral range, namely from 155 nm to 3200 nm.

LBO is a negative biaxial, orthorombic crystal with point group symmetrie mm2 and lattice parameters $a = 8.447\,\text{Å}$, $b = 7.379\,\text{Å}$, and $c = 5.140\,\text{Å}$. The birefingence of LBO is small and the nonlinear coefficient is moderate. It has a small walk-off angle and a very broad spectral acceptance. Various sets of Sellmeier equations have been published for this material. Good results are obtained by using the Sellmeier equations determined by Kato *et al.* [Kat90].

LBO is a non-hygroscopic crystal with good mechanical and chemical stability. It is typically grown by flux method and large, almost inclusion free crystals of high optical quality can be processed. Due to the high damage threshold, it can be used for high power applications.

Non-critical phase matching in LBO for frequency conversion to the green spectral range is possible. The required temperature for SHG at 1.064 nm is 148 °C with a temperature acceptance bandwidth of 3.9 °C. However, since high temperatures are undesirable for most applications, critical phase matching was preferred for the presented setups.

5.1.3 Bismuth borate (BiB_3O_6)

Bismuth borate (BiBO) in contrary to LBO and KTP is a relatively new nonlinear crystal material. First studies on BiBO were conducted by Hellwig *et al.* in 1998 [Hel99]. However, BiBO already has proven to be a good material for single-pass as well as intracavity frequency doubling.

BiBO has a biaxial, monoclinic structure of point group 2 with the lattice parameters $a = 7.116\,\text{Å}$, $b = 4.993\,\text{Å}$, and $c = 6.508\,\text{Å}$. Like the other crystals, BiBO is non-hygroscopic. Adequate Sellmeier coefficients are given in [Hel00].

The transparency of BiBO ranges from 300 nm to 2500 nm. It has a large effective nonlinear coefficient of $\sim 3.3\,\text{pm/V}$ and conversion efficiencies of more than 63 % have been demonstrated previous to this thesis [Cze03]. A major drawback of BiBO is its exceptionally large walk-off angle of $\sim 28\,\text{mrad}$ at 1050 nm. The spectral acceptance is moderate and ranges between that of LBO and KTP.

	KTP	**LBO**	**BiBO**
nonlinear coefficient (pm/V)	3.3	1.0	3.3
spectral acceptance (nm · cm)	0.67	4.7	3.4
temperature acceptance (K · cm)	25	5.8	2.2
angular acceptance (mrad · cm)	20	6.5	2.1
walk-off angle (mrad)	1	4	26
θ_{PM}	90°	90°	168.9°
φ_{PM}	24.8°	11.4°	90°
transparency range (nm)	350-4500	155-3200	300-2500
phase matching range (nm)	994-3400	554-2600	542-3000

Table 5.1: Properties of the utilized nonlinear optical crystals for SHG from 1064 nm to 532 nm [Dmi99],[Wes06],[Hel99],[Gho04].

Other widely used crystals for SHG around 1064 nm are beta barium borate ($\beta - BaB_2O_4$, BBO), potassium niobate ($KNbO_3$) and lithium niobate ($LiNbO_3$). However, BBO has a very low spectral acceptance and seems to be inferior in comparison with BiBO regarding nonlinear coefficient and walk-off angle. $KNbO_3$ has the highest nonlinear coefficient of the described crystals, but the low spectral and temperature acceptance make it impractical for the use with OPS disk lasers in many applications. Therefore, these two materials were not tested in this thesis. Lithium niobate is of special interest as periodically poled material and will be described in the next chapter.

A comparison of the basic optical properties is given in table 5.1. The values for the

spectral acceptance were measured by external frequency doubling with a widely tunable ytterbium doped lanthanum scandium borate (Yb:LSB) thin disk laser (see Fig. 5.1).

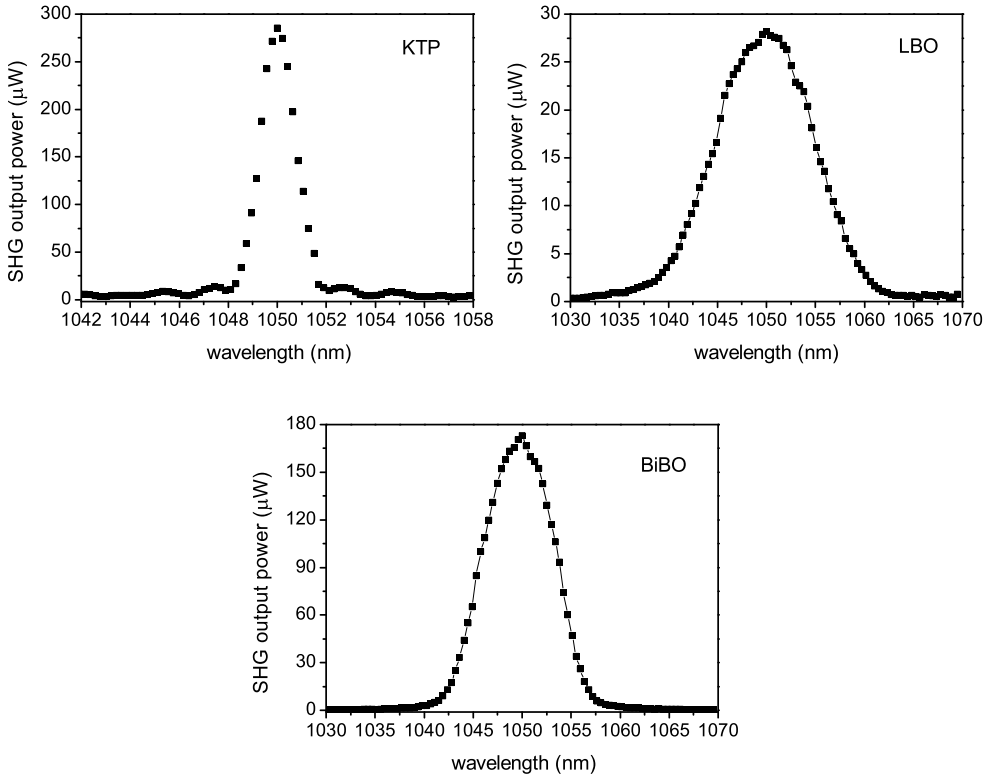

Figure 5.1: Spectral acceptance measurements for KTP, LBO, and BiBO. All crystals were 4 mm long.

5.2 Experimental setup

As described in chapter 4, high intensities within the nonlinear crystal are required to obtain significant conversion efficiencies. Therefore lasers with high output powers or with short pulses are advantageous for nonlinear frequency conversion. However, for low power continuous wave lasers, like the presented OPS disk lasers, sufficient intensity can be achieved by intracavity frequency doubling, where the conversion process profits from the enhanced intracavity power.

In the presented experiments a V-type resonator was used (see Fig. 5.2). It consisted of the integrated Bragg reflector and two external mirrors. The folding mirror M1 had a radius of curvature of $r_1 = 75\,\text{mm}$ and a distance of $L_1 = 68\,\text{mm}$ from the OPS chip. The tilting angle was kept low at approximately 10° with respect to the semiconductor surface normal to limit astigmatism. M1 was used as output coupler for the second harmonic wave and was highly transmissive ($> 97\%$) around 525 nm. The end mirror M2 had a radius of curvature of $r_2 = 25\,\text{mm}$, a distance of about $L_1 = 109\,\text{mm}$ from M1 and was highly reflective around 525 nm. Both external mirrors were particularly high reflective around 1050 nm ($> 99.95\%$) to achieve highest intracavity intensities at the fundamental wavelength.

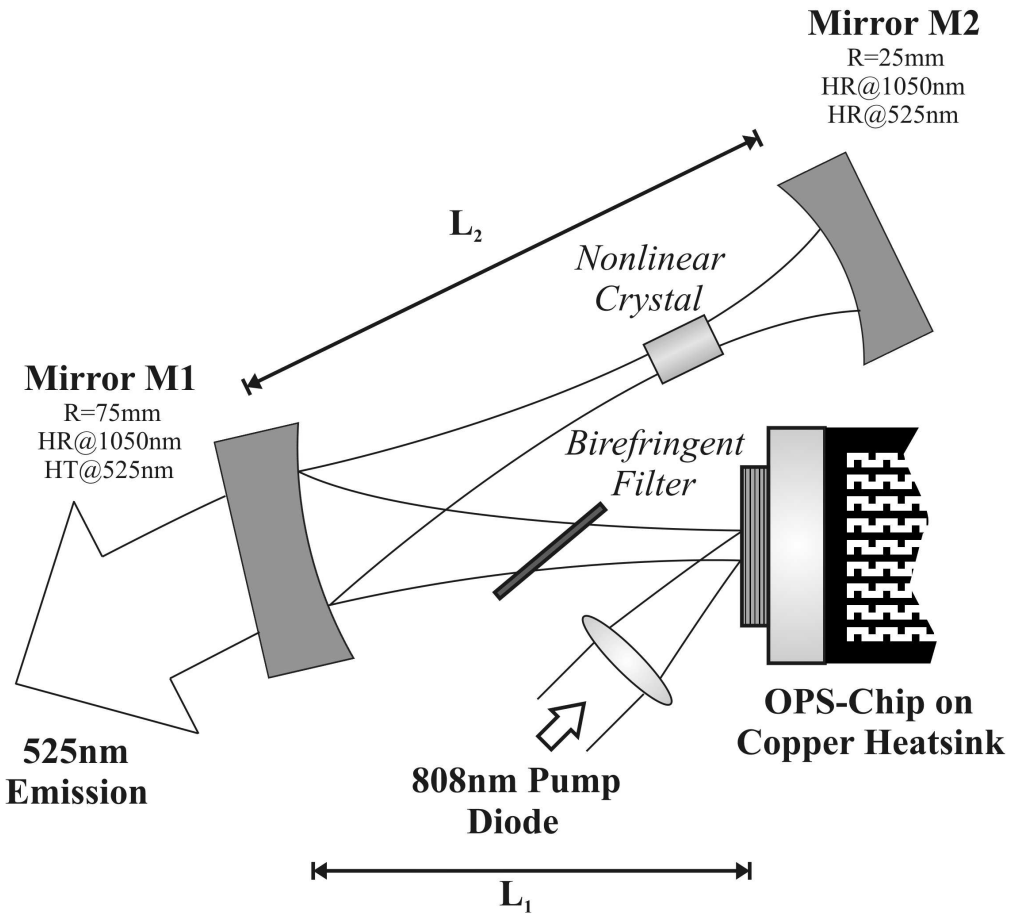

Figure 5.2: Schematic setup for intracavity frequency doubling experiments. The birefringent filter can be replaced by an etalon.

The V-type resonator was advantageous, because it provided a beam waist at the OPS chip and a second beam waist between M1 and M2. At these positions the highest intensities were realized. The second waist was located about 25 mm in front of the end mirror. Its tightness and length could be adjusted by varying the lengths of the resonator

arms. The nonlinear crystal was positioned at this beam waist. Accurate angular and positional adjustment of the crystal was possible for all angles and directions. Furthermore, the crystal could be temperature tuned by a peltier controlled oven. All nonlinear crystals were anti-reflection coated on both sides.

For intracavity SHG the fundamental wavelength of the OPS disk lasers had to be spectrally controlled for two reasons. On the one hand the linewidth had to be limited to match the spectral acceptance of the nonlinear crystal. On the other hand the gain of OPS disk lasers is spectrally broad and highly homogeneous and therefore the lasers tended to operate away from the phase matching wavelength to avoid the losses caused by nonlinear frequency conversion. Accordingly for maximum conversion efficiency the wavelength selective elements not only had to narrow the linewidth below the spectral acceptance of the nonlinear crystal but also were needed to cleave the fundamental wave to the phase matching wavelength. For the presented experiments either an etalon or a birefringent filter at Brewster's angle was used.

Like for the infrared experiments the semiconductor structure was optically pumped by an 808 nm laser diode at an angle of 45°. The pump geometry was identical to the one described in section 3.1.1 and is sketched in Fig. 5.2. For all experiments presented in this chapter the heat sink temperature was kept at 25°C.

The infrared power characteristic for the V-type resonator comprising chip 3 is shown in Fig. 5.3. The astigmatism of the folded cavity caused a smaller overlap of the fixed pump spot with the cavity mode and therefore the IR output was reduced in comparison with the linear resonator presented in chapter 3. For 0.87% output coupling, 128 mW of infrared power could be achieved with the folded cavity. Additional cavity elements like an etalon or a birefringent filter caused additional losses and hence further reduced power was observed. The laser was linearly polarized perpendicular to the plane of the resonator (s-polarization). For the frequency doubling resonator with its high reflective mirrors, the intracavity power was estimated to be about 13.5 W.

Since the steps between the available output couplers presented in Fig. 5.3 are quite large, it is possible, that higher infrared output powers are achieved by using an outcoupling mirror with a transmission slightly above or below 0.87%. An upper limit for the maximum achievable infrared power from the V-type resonator with and without wavelength selective element will be estimated in the following paragraphs.

A set of outcoupling mirrors with small transmission steps was available with a radius of 100 mm. The appropriate linear resonator comprising OPS chip 3 yielded a maximum infrared output power of 157 mW at an outcoupling rate of 1.2%. For the proximate outcoupling rates of 0.87% and 1.6% the output power was reduced by 3.5% and 9.1% respectively. Considering these deviations and the miscellaneous measurement uncertainties, an upper limit for the output power of 165 mW at the maximum pump power could be estimated.

To approximate the minimum power reduction when applying the V-type resonator in-

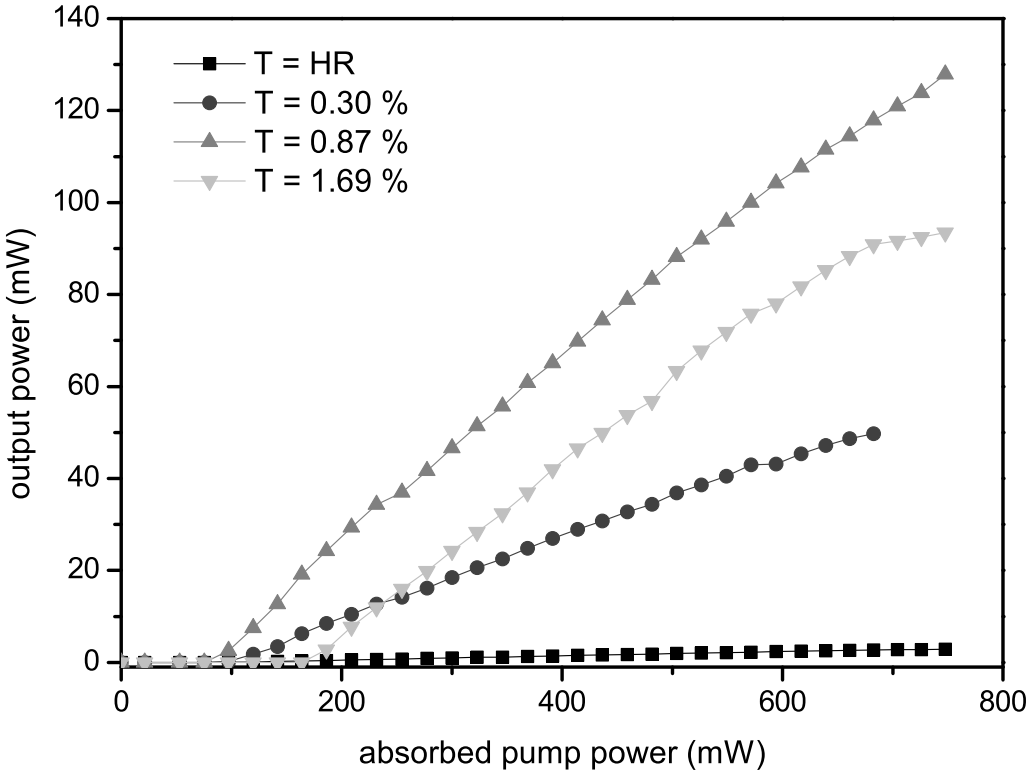

Figure 5.3: Infrared output power versus absorbed pump power for different output couplers.

stead of the linear cavity, similar measurements using different outcoupling rates for both setups were conducted with four different semiconductor structures. The power reduction varied between 16% and 27%. A lower limit for the power reduction of 12% was approximated, taking into account the high statistical error. Accordingly, the achievable infrared output power of the V-type resonator is expected to be below 145 mW.

If intracavity elements are added to the resonator, the cavity losses are increased and the maximum available output power is further reduced. The minimum power reduction caused by a wavelength selective element was found to be 4.3% for an etalon. Altogether, the upper limit of the maximum achievable infrared power for the V-type resonator with an intracavity wavelength filter was estimated to be 139 mW. The conversion efficiency for frequency doubling with different nonlinear crystals was calculated with respect to this value. The infrared losses induced by the nonlinear crystals could not be measured and hence were neglected for these estimations.

5.3 KTP experiments

The KTP crystals were cut at angels of $\theta = 90^\circ$ and $\varphi = 35.1^\circ$ for type II phase matched SHG at 1050 nm. Crystal lengths from 1 mm to 6 mm in steps of 1 mm were available with an aperture of $3 \times 3\,\mathrm{mm}^2$.

Without any spectral control no appreciable SHG output was obtained. Only a strongly fluctuating green emission at a power level well below 1 mW could be observed. By inserting an intracavity etalon the power could be increased to a few milli-Watts, but the output was still unstable and far below the desired power. Measurements concerning spectral and polarization characteristics of the output indicated, that the fundamental wave not only switched the wavelength but also the polarization to avoid conversion losses. For OPS disk lasers polarization switching is possible with negligible reduction of the efficiency.

This polarization switching effect only occurred for KTP and was not observed for SHG with LBO or BiBO, which can be explained as follows. For frequency doubling with KTP the fundamental wave has ordinary and extraordinary polarized fractions due to the type II phase matching scheme. This birefringence caused a depolarization of the fundamental wave as it traveled along the KTP crystal. After passing the crystal the infrared wave comprised circularly or elliptically polarized fractions, that were enhanced in the gain medium and caused the polarization switching. The strength of the depolarization depends on the optical length of the birefringent medium. The phase difference between the ordinary and extraordinary wave varies periodically with the crystal length. Accordingly, a phase difference of $n \cdot 2\pi$ corresponding to zero depolarization theoretically should be achievable for example by adjusting the optical length via temperature tuning of the KTP crystal. However, the high sensitivity of such a setup makes this approach impractical for any consumer application.

A considerable improvement of the performance was achieved by replacing the etalon with a quartz birefringent filter tilted at Brewster's angle. Such a filter not only narrows the linewidth, but also stabilizes the polarization by outcoupling of the depolarized fraction of the fundamental wave and thereby preventing it from further amplification. Fig. 5.4 shows the output powers obtained for a 2 mm and a 3 mm long crystal. The maximum SHG powers were 12.5 mW at 747 mW of absorbed pump power and 3.9 mW at 660 mW of absorbed pump power respectively. The corresponding optimum crystal temperatures were found to be 25.7°C and 27°C. On the right hand side of Fig. 5.4 the respective IR powers coupled out by the birefringent filter are shown. The overall IR powers coupled out at both sides of the filter were 53.8 mW for the 2 mm long crystal and 21.7 mW in the case of the 3 mm long crystal.

The beam quality of the green emission was near diffraction limited and the beam quality parameter was measured to be $M^2 < 1.15$. A photograph of the far field beam profile is displayed in Fig. 5.8 (a).

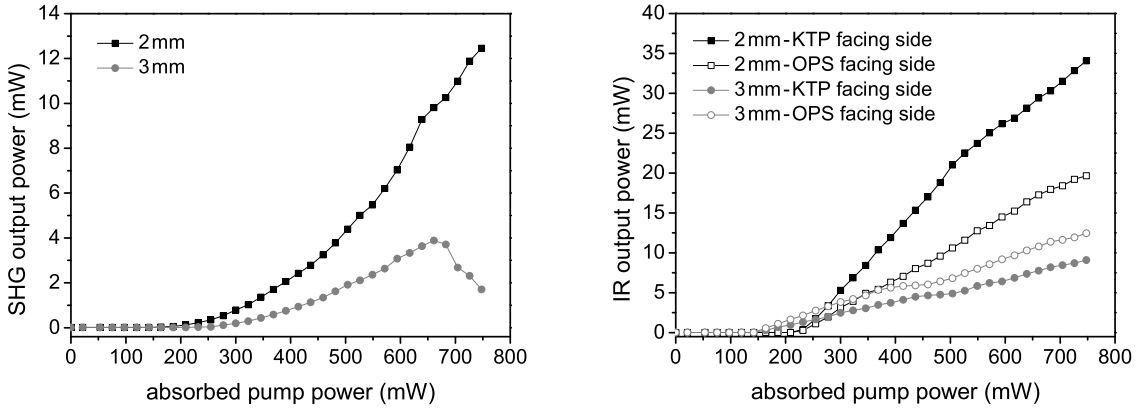

Figure 5.4: Output power for SHG with KTP (left) and the corresponding IR losses at the birefringent filter (right).

For all KTP comprising setups the alignment of the resonator was very sensitive. Particularly in the case of the 3 mm long crystal slight changes of the crystal temperature or careful rotation of the birefringent filter resulted in dramatically reduced output power. It was not possible to achieve stable operation over the full pump power range.

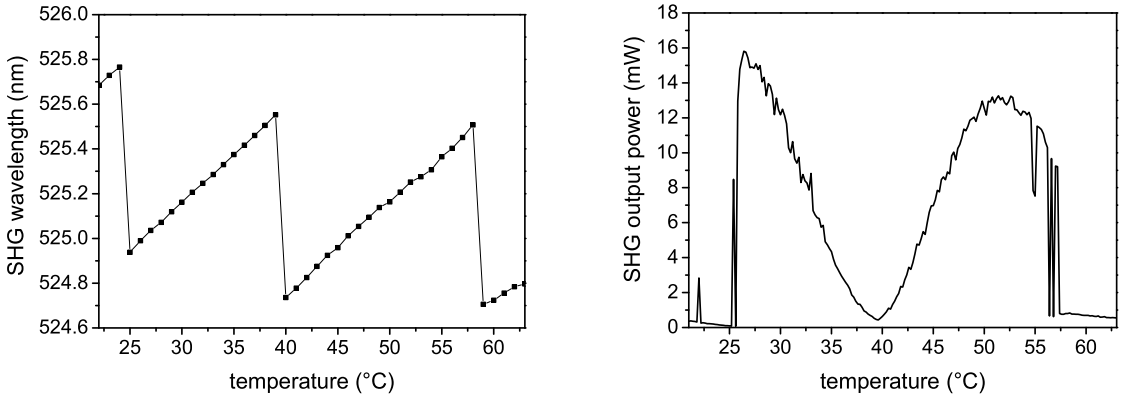

Figure 5.5: SHG wavelength shift for intracavity doubling with KTP and birefringent filter at Brewster's angle (left) and the corresponding SHG output power (right) measured with chip 1.

Fig. 5.5 (right) shows, how the SHG output power depended on the crystal temperature if all other resonator parameters are unchanged. Two peaks were observed at 26.5°C and 51.4°C. From Fig. 5.5 (left) it can be seen, how the wavelength shifted to avoid depolarization and nonlinear outcoupling losses. Wavelength jumps occurred whenever

the order of the birefringent filter changed to a higher one. The wavelength range was limited by the selectivity of the birefringent filter and depended on its thickness. Plates of higher thickness are more selective, which was found to be beneficial for the SHG output power. The best results were obtained with a 2.5 mm thick quartz plate.

Laser operation was also possible with an 1 mm and a 4 mm long crystal, but for both crystals the SHG output powers were well below 1 mW. Laser operation with the 4 mm KTP crystal in the cavity required particularly careful alignment and was unstable. In the case of the 1 mm long crystal the alignment was less sensitive.

For completeness it should be noted, that all six KTP crystals provided significant conversion efficiencies for an OPS disk laser optimized for higher power levels. More than 70 mW of SHG power at an absorbed pump power of 1.3 W could be demonstrated with chip 1. This setup was much less sensitive to alignment.

5.4 LBO experiments

The LBO crystal had the dimensions $4 \times 3 \times 3\,\mathrm{mm}^3$ and was cut for type I phase matching at angles of $\theta = 90^\circ$ and $\varphi = 12.4^\circ$. The optimum crystal temperature was found to be 25.6°C. An etalon was used for spectral filtering.

For SHG with LBO it was particularly important to select the etalon thickness and the operation wavelength correctly. In section 3.3.4 it has been shown, that the OPS disk laser can operate over a wavelength range of more than 10 nm without significantly reducing the output power. Accordingly, the laser tended to switch to a different wavelength, if nonlinear outcoupling losses were introduced to the operation wavelength. Preferably the wavelength changed to an adjacent maxima of the etalon. Therefore, the etalon had to be quite thin, so that the adjacent maxima were out of the tuning range. In the presented experiment an etalon of about 30 µm thickness was used, which had a free spectral range of more than 12 nm. If a central position within the tuning range was chosen, the adjacent wavelengths were just outside the tuning range and the laser emitted on the same wavelength over the complete pump power modulation range. The peak width of the etalon was not as important, since the spectral acceptance of LBO is broad. Even thinner etalons should alow for easier alignment, but would be hard to handle. These considerations also proved true for BiBO and PPLN.

A maximum output power of 27 mW at 525 nm was achieved for the 4 mm long LBO crystal. This corresponds to a conversion efficiency of 19.4% with respect to the maximum available infrared power. Fig. 5.6 shows that the SHG output power increased quadratically with the pump power. The IR output leaking out the HR mirrors is also indicated (circles). It developed less than linearly due to the increasing nonlinear conversion losses. The beam quality was near diffraction limited with a beam quality parameter

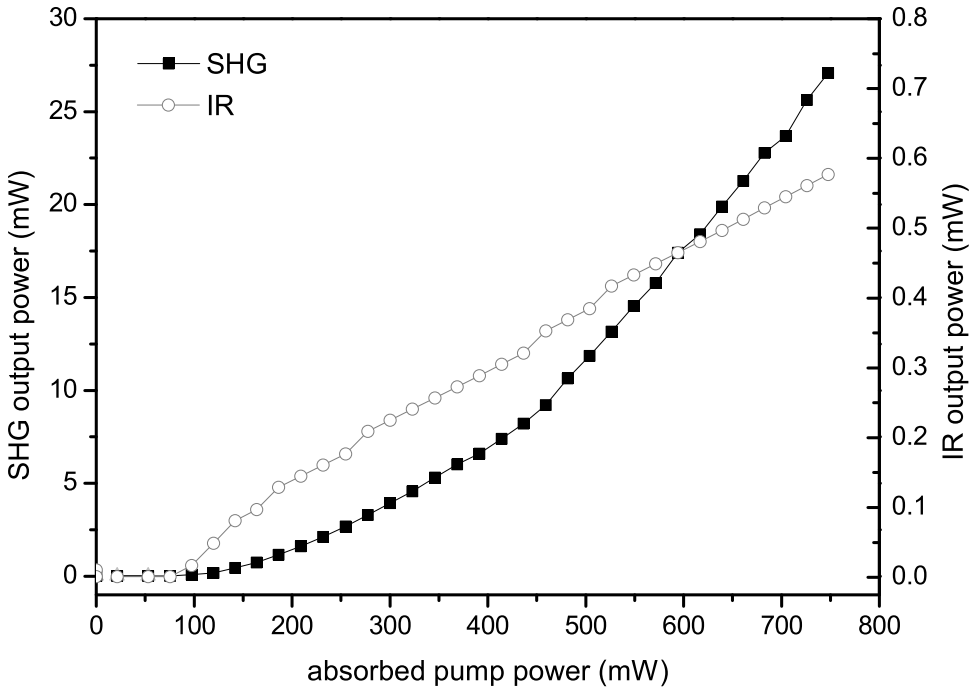

Figure 5.6: SHG and IR output power for a 4 mm long LBO crystal.

of $M^2 < 1.2$. The far field beam profile was similar to that of the KTP setup 5.8 (b). The output was stable on long and short time scales.

5.5 BiBO experiments

BiBO has a three times higher effective nonlinear coefficient than LBO and therefore higher conversion efficiencies could be expected from this material. For the experiments BiBO crystals with 2 mm, 4 mm, and 6 mm lengths and an aperture of $3 \times 3\,\mathrm{mm}^2$ were used. The angles for type I phase matching at 1050 nm were calculated to be $\theta = 168°$ and $\varphi = 90°$. The temperature was stabilized at 26°C.

The maximum SHG output powers were 113 mW, 79 mW, and 22 mW for the 6 mm, 4 mm, and 2 mm long crystals respectively. The corresponding conversion efficiencies from 1050 nm to 525 nm with respect to the maximum available infrared power were 81 %, 57 %, and 15.8 %. 81 % is, to the best of our knowledge, the highest conversion efficiency ever reported for low power OPS disk lasers. From Fig. 5.7 it can be seen, that

the output characteristic for the 2 mm long crystal exhibits a quadratic rise with increased pump power, whereas the curves for the 4 mm and the 6 mm long crystal behave near quadratic for low pump powers and than saturate to a near linear behavior, indicating that the nonlinear outcoupling rate was close to the optimum. The residual IR power was about the same for the 4 mm and 6 mm long crystals and slightly higher for the 2 mm long crystal.

The wavelength control was even more crucial than for LBO, because the nonlinear outcoupling rate and accordingly the infrared losses were much higher. The same etalon was used, but the alignment was somewhat more sensitive.

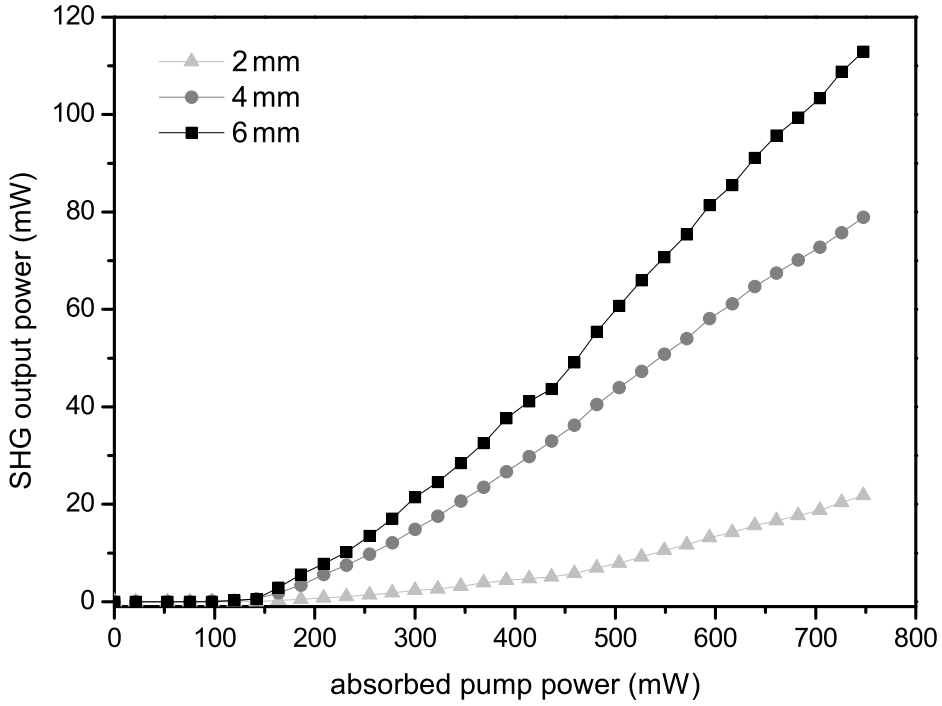

Figure 5.7: SHG output powers for the BiBO crystals.

Regarding conversion efficiency and output power the BiBO setup more than accomplished the desired laser parameters. However, BiBO suffers from a very high Poynting vector walk-off. The consequence was a disturbance of the beam quality.

The far field exhibited an interference pattern, which resulted from a combined effect of the large walk-off angle and the curved end mirror (see Fig. 5.8 (c)). More than 80% of the energy was located within the main peak of the pattern and the beam quality factor

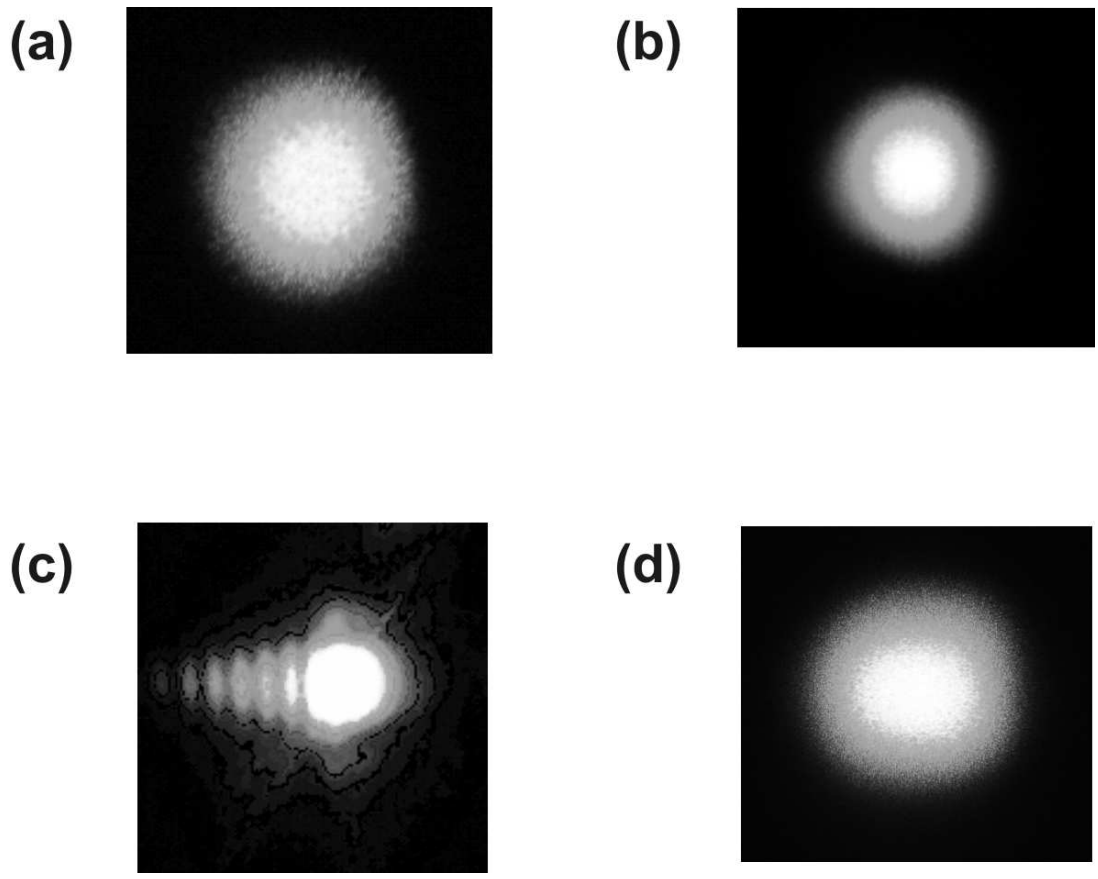

Figure 5.8: Beam profiles for intracavity frequency doubling with (a) KTP, (b) LBO, (c) BiBO, and (d) a setup with a planar end mirror and BiBO.

of this peak was measured to be $M_x^2 < 1.45$ and $M_y^2 < 4$ for a setup with a 4 mm long BiBO crystal. The pattern disappeared for a setup with planar end mirror, leaving an elliptical, unmodulated spot (Fig. 5.8 (d)), but for this configuration the output power decreased below that of the LBO setup.

5.6 Sum frequency generation

As demonstrated in section 3.3.4, OPS disk lasers can operate on different wavelengths at the same time. Accordingly, intracavity frequency conversion via sum frequency generation (SFG) or difference frequency generation (DFG) should be possible. In this section only SFG will be treated, since no crystals and detectors were available for the long wavelengths expected from DFG.

The phase matching angles for SFG are similar to those for SHG and therefore the same crystals tilted by a slightly different angle could be used. The presented results were

obtained using a 4 mm long BiBO crystal. A glass etalon with a thickness of about 70 µm was used to achieve simultaneous operation on two fundamental wavelengths.

From the infrared spectrum in Fig. 7.4 (a) it can be seen, that dual-wavelength operation was achieved with a spectral gap of 0.52 nm. The corresponding emission spectrum for the green spectral range is shown in Fig. 7.4 (b). This spectrum exhibits two outer peaks at the SHG wavelengths of the infrared spectrum and an additional middle peak which can be attributed to SFG. The observed sum frequency generation is proof for the coexistence of the two fundamental wavelengths.

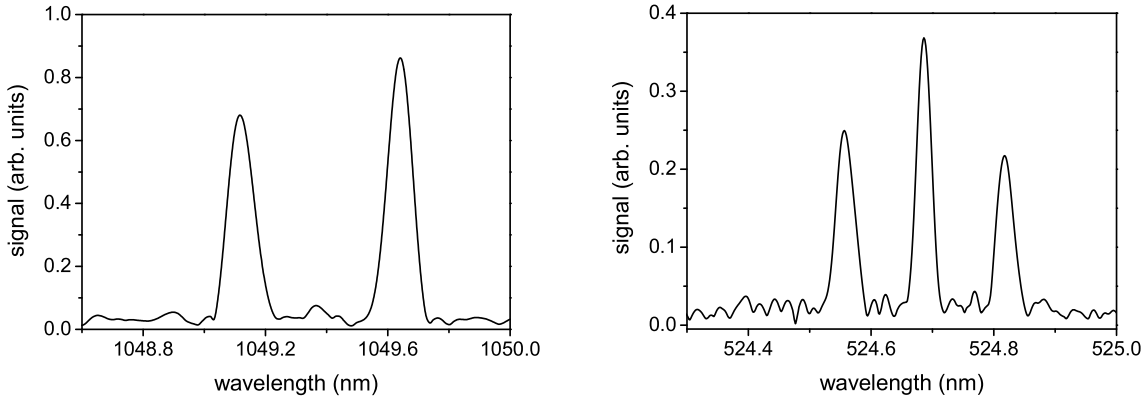

(a) infrared spectrum

(b) SHG and SFG spectrum

Figure 5.9: Sum frequency generation proved that the OPS disk laser operated on two wavelengths at the same time.

Since the gain spectra of OPS disk lasers shift with the absorbed pump power, SFG could only be realized for a small pump power range of about 20 to 30 mW without realignment of the resonator. Pump powers somewhat below or above this range typically resulted in single wavelength emission on the shorter or longer wavelength correspondingly.

The combined output powers of SFG and SHG were only slightly below those obtained at the same pump power with the SHG setup, since all involved wavelengths were well within the spectral acceptance of the nonlinear crystal and the losses of the 70 µm etalon were similar to those of the 30 µm etalon presented above.

In chapter 7 further SFG experiments will be presented, in which etalons of different thicknesses were used to vary the gap between the two fundamental wavelengths from 0.13 nm to 12.4 nm.

	KTP	LBO	BiBO
maximum output power	12.5 mW	27 mW	113 mW
maximum conversion efficiency	9.0%	19.4%	81%
beam quality	$M^2 < 1.15$	$M^2 < 1.2$	$M_x^2 < 1.45$, $M_y^2 < 4$
spectral filter	birefringent filter	etalon	etalon
polarization control	required	none	none
sensitivity to misalignment	very high	low	moderate

Table 5.2: Summary of the SHG results obtained with chip 3 for KTP, LBO, and BiBO.

5.7 Summary

In this chapter birefringent phase matched frequency doubling experiments with different nonlinear optical crystals have been demonstrated. A comparison of the obtained results is given in table 5.2.

Despite its high effective nonlinear coefficient, the conversion efficiency for intracavity doubling with KTP was quite low. Due to the type II phase matching scheme, accurate temperature control was required and the polarization had to be stabilized. The beam quality was very good, but the bulkiness of a birefingent filter at Brewster's angle and the delicate alignment make KTP impractical for use in compact portable setups.

The cavity comprising LBO was much easier to align and yielded higher output powers. The beam quality was good and an etalon could be used instead of the birefringent filter. However, due to the low nonlinear coefficient, the conversion efficiency has not proved satisfactory.

The highest efficiencies were achieved with a 6 mm long BiBO crystal at a maximum SHG output power of 113 mW, corresponding to a conversion efficiency of 81% with respect to the maximum available infrared power. This is, to the best of our knowledge, the highest conversion efficiency for low power OPS disk lasers. Unfortunately, the beam quality for this setup was bad due to the high Poynting vector walk-off.

6 Frequency doubling with MgO:PPLN

Periodically poling of crystals is an emerging field and extends the feasibilities of frequency conversion in several ways. The quasi phase matching (QPM) scheme is possible even in cases where no birefringent phase matching can be achieved, allowing for the use of the highest nonlinear coefficients. Furthermore periodically poled crystals can be designed to meet special requirements like tunability or simultaneous SHG of two widely spaced wavelengths. Schematic pictures of some special designs for periodically poled structures are shown in Fig. 6.1. The basic design is a single period structure (a), which is engineered for quasi phase matching of a particular frequency conversion process. Multiple grating structures (b) comprise segments of different poling period aligned side by side. By shifting the crystal horizontally the different gratings can be accessed. In a cascaded structure (c) the spatial positions along the crystal are designed

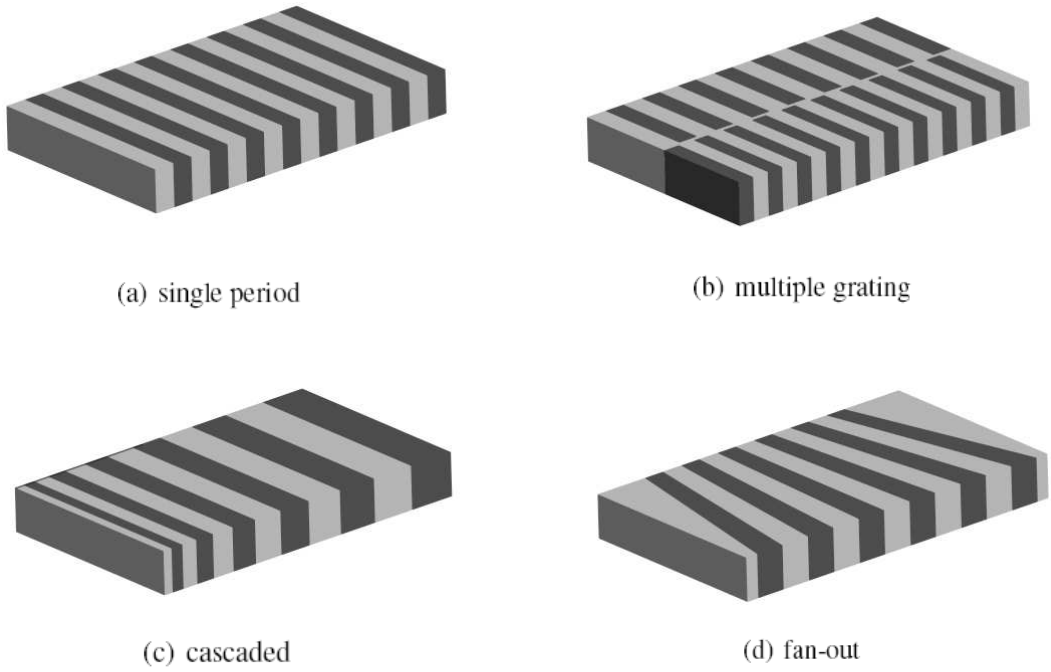

Figure 6.1: Different structure designs for periodically poled crystals.

for conversion of different frequencies and hence these structures yield a broadened bandwidth, e. g. to match the spectrum of ultra short pulses. A fan-out structure (d) exhibits a linear horizontal increase of the poling period and accordingly can be used for continuous wavelength tuning.

During the last few years electric field poling techniques have been improved and periods short enough for 1st order QPM frequency doubling to the blue or even ultraviolet can be produced. Furthermore, the processable crystal thickness has been enhanced [Ish03]. Thus periodically poled media are prospective materials for commercial applications.

Intracavity frequency doubling of OPS disk lasers with periodically poled potassium titanyl phosphate (PPKTP) from 978 nm to 489 nm successfully has been demonstrated previously [Raf03]. In this chapter the applicability of single period and bandwidth enhanced structures of magnesium oxide doped periodically poled lithium niobate (MgO: PPLN) to intracavity frequency doubling of OPS disk lasers will be discussed.

6.1 Periodically poled lithium niobate (PPLN)

Lithium niobate is a negative uniaxial crystal of the trigonal point group 3m. The lattice constants are $a = 5.151$ Å and $c = 13.865$ Å. It is non-hygroscopic and transparent from 350 nm to 5000 nm. It can be grown by Czochralski method with high optical quality. The ferroelectric domains of lithium niobate are parallel to the c-direction with altering sign.

Periodically poled lithium niobate has gained particular importance with the onset of electric field poling in the early 1990's as an attractive material for frequency doubling and in optical parametric oscillators. Lithium niobate is already produced at high volumes and the poling can be processed on wafers up to 4 inch diameter. This makes PPLN likely to become compatible with consumer applications regarding production costs.

Since the crystal axis can be chosen without limitations due to phase matching considerations, the direction with the largest nonlinear optical coefficient can be accessed. In the case of lithium niobate this is $d_{33} = 27$ pm/V, which results in $d_{eff} = \frac{2}{\pi} d_{33} \approx 17$ pm/V for 1st order QPM. The birefringence depends on the crystal temperature and thus the poling periods are calculated for a given operating temperature. Temperature dependent Sellmeier coefficients for such calculations are given in [Jun97].

6.1.1 Magnesium oxide doping

All crystals presented in this chapter are congruently grown and doped with magnesium oxide (MgO) at a concentration of about 5% (mol.). Conventional undoped congruent lithium niobate (CLN) suffers from green induced infrared absorption (GRIIA) and a

low photorefractive damage threshold. It has been demonstrated, that by adding about 5 % MgO, GRIIA effects are strongly reduced [Fur01] and the optical damage threshold is improved significantly [Bry84]. Furthermore, MgO doping lowers the electric field strength required for domain inversion [Che05].

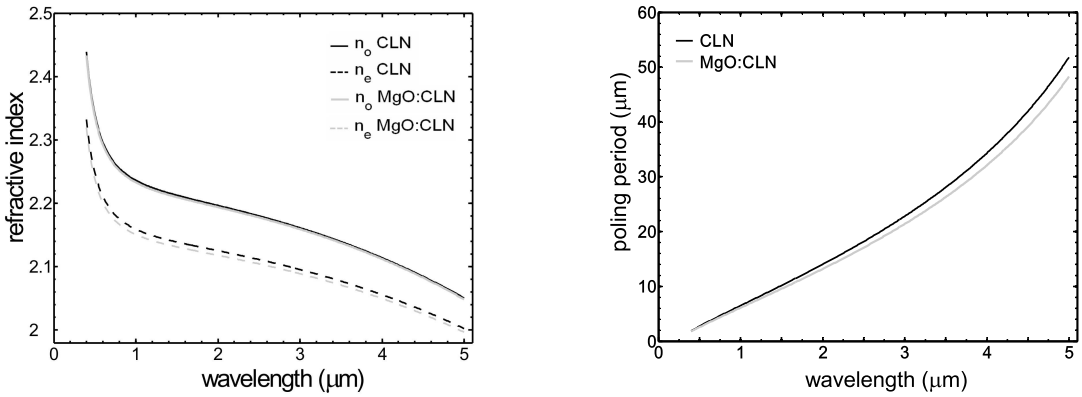

Figure 6.2: Simulation of the wavelength dependent refractive index (left) and calculated poling periods for 1st order quasi phase matched SHG (right) in congruent PPLN with and without 5 % MgO doping in comparison.

MgO doping also influences the refractive index and the birefringence of the material. This has to be taken into account for calculating the poling periods. Sellmeier coefficients for CLN with 5 % MgO doping are given in [Zel97]. A comparison of the refractive indices and of the wavelength dependent poling period is shown in Fig. 6.2.

6.2 Single period structures

The simplest structures are single period crystals. These crystals are designed for conversion of a specific wavelength at a given operation temperature. In this section two single period crystals with 0.50 mm and 0.75 mm thickness are compared.

6.2.1 Crystal characterization

The presented crystals had the dimensions $0.50 \times 0.90 \times 1.25\,\mathrm{mm}^3$ and $0.75 \times 1.04 \times 1.25\,\mathrm{mm}^3$ for thickness, length and width respectively. They were designed for frequency doubling from 1050 nm to 525 nm at an operation temperature of 50°C. Both sides were anti-reflection coated for the fundamental and second harmonic wave.

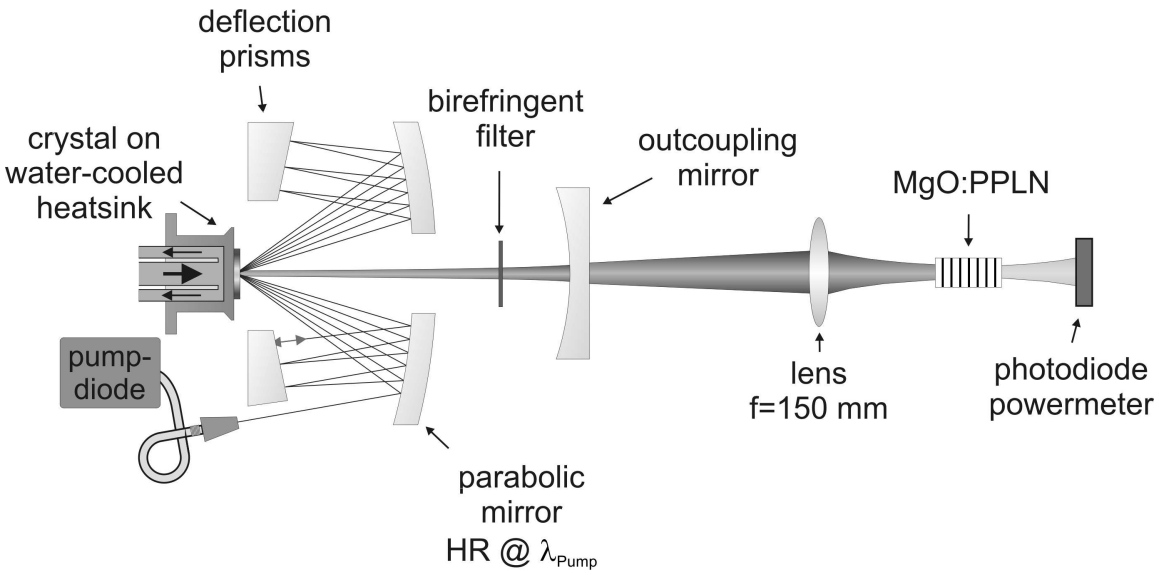

Figure 6.3: Setup for external SHG with a widely tunable Yb:Lu_2O_3 thin disk laser.

For characterization of the crystals in a single-pass configuration a widely tunable ytterbium doped lutetium oxide (Yb:Lu_2O_3) thin disk laser was used (see Fig. 6.3). This laser provided more than 10 W of continuous wave output power over a tuning range of 90 nm around the desired wavelength of 1050 nm. Tuning was achieved with an 1 mm thick birefringent filter. Additional information about this laser system can be found in [Pet07].

The beam of the thin disk laser was weakly focussed into the medium by a $f = 150$ mm lens to form a homogeneous intensity distribution over the full crystal length. The crystal temperature was stabilized at 50°C and the surface was oriented normal to the incident beam. To measure the spectral acceptance of the crystal, the thin disk laser was tuned from 1040 nm to 1060 nm. The infrared output power of the thin disk laser was kept constant at 2.0 W over the whole tuning range.

From Fig. 6.4 (bottom) it can be seen, that the spectral acceptance followed a sinc^2-function for both crystals, like it has been predicted in chapter 4. The peaks were positioned at 1051.1 nm and 1051.5 nm respectively, which was slightly higher than the calculated wavelengths. The FWHM was measured to be 1.97 nm and 1.78 nm corresponding to spectral acceptances of 0.177 nm·cm and 0.185 nm·cm.

Fig. 6.4 (top) shows the homogeneity over the full aperture in comparison for both crystals. For these measurements the infrared power was reduced to 1.0 W. The homogeneity was measured by scanning the infrared beam adjusted at the optimum wavelength over the whole aperture of the MgO:PPLN crystals in equally spaced steps. Clipping of the beam at the lateral edges was excluded by discarding the outermost measurements at both sides of the crystal.

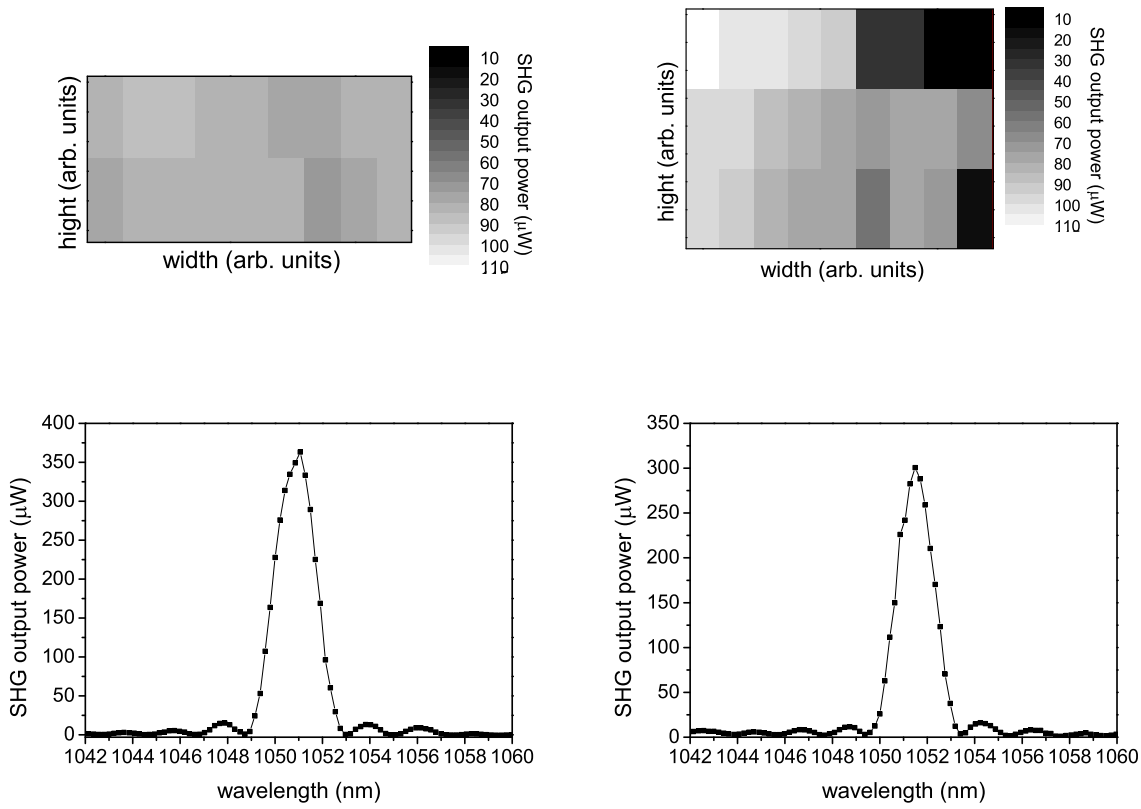

Figure 6.4: Homogeneity (top) and wavelength acceptance (bottom) for external SHG with 0.50 mm (left) and 0.75 mm (right) thick single period MgO:PPLN.

The 0.50 mm thick sample exhibited highly homogenous conversion efficiency over the whole aperture. The SHG output powers ranged between 74.7 µW and 85.2 µW with an average value of 81.8 µW and a standard deviation of 2.8 µW. The 0.75 mm thick crystal was much more inhomogeneous and yielded SHG output powers between 5.0 μW and 110.5 μW with an average value of 73.28 μW and a standard deviation of 28.3 μW. This indicates that the development of the domains in the crystal was not uniform in this case. Similar results were obtained for other crystals with same thicknesses.

Even though the poling was inhomogeneous for the 0.75 mm thick crystal, there were many good crystal positions for efficient frequency doubling. However, the advantage of a larger aperture could not be used.

6.2.2 SHG experiments

Both single period crystals were applied to the SHG setup presented in section 5.2. The crystals were heated to 50°C and an etalon was used as wavelength selective element. Like for BiBO and LBO, careful adjustment of the operation wavelength was required to prevent excitation of modes beyond the spectral acceptance of the nonlinear crystal.

Fig. 6.5 displays the measured SHG output powers for both crystals. The maximum output powers were 69 mW and 65 mW for the 0.50 mm and the 0.75 mm thick sample respectively. This corresponds to conversion efficiencies of 49.6% and 46.8% with respect to maximum available infrared power. The emission at 525 nm was near diffraction limited and a beam quality parameter of $M^2 < 1.2$ was determined for the setup containing the 0.50 mm thick MgO:PPLN crystal.

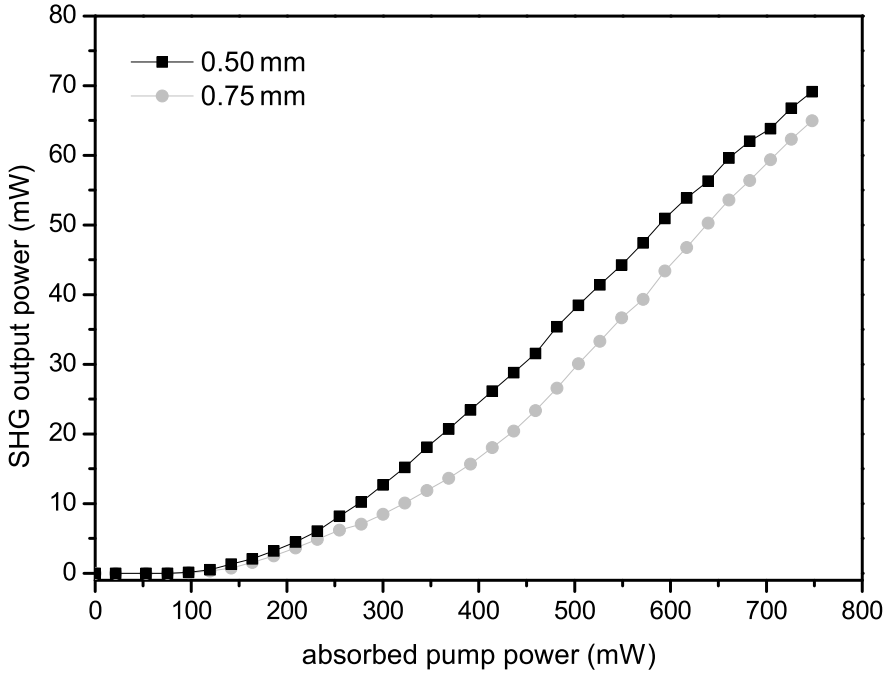

Figure 6.5: SHG output power for single period MgO:PPLN.

As described above, the spectral acceptance of the periodically poled crystals is quite low. Since for an intracavity configuration the crystal is passed twice, it should be even lower in this case. For the actual SHG setup it was not possible to tune the wavelength without realignment of the cavity. Therefore the intracavity spectral acceptance was determined by measuring the thermal acceptance of the nonlinear crystal. In [Zhu03]

it has been shown that the central wavelength of the bandwidth acceptance spectrum shifts with a near linear temperature dependence for 1st order QPM around 1500 nm. Simulations of the temperature dependence for SHG at 1050 nm exhibited an almost linear shift of the central wavelength by about 0.080 nm/K. Experimental verification using the external SHG setup yielded a value of 0.082 nm/K. It should be noted, that low temperatures correspond to long wavelengths and accordingly the temperature spectrum has to be flipped for comparison with the bandwidth acceptance curve.

Fig. 6.6 shows the MgO:PPLN intracavity temperature dependence of the SHG output power for the 0.50 mm thick crystal. The measurements were conducted using a moderate pump power at which stable output power over several hours had been demonstrated previously. The central peak had a FWHM of 11.75 K corresponding to a spectral acceptance of 0.97 nm. Thus the spectral acceptance was reduced by a factor of roughly 2 with respect to the single-pass configuration. This effect was expected, since the effective crystal length is twice as high for a double-pass setup.

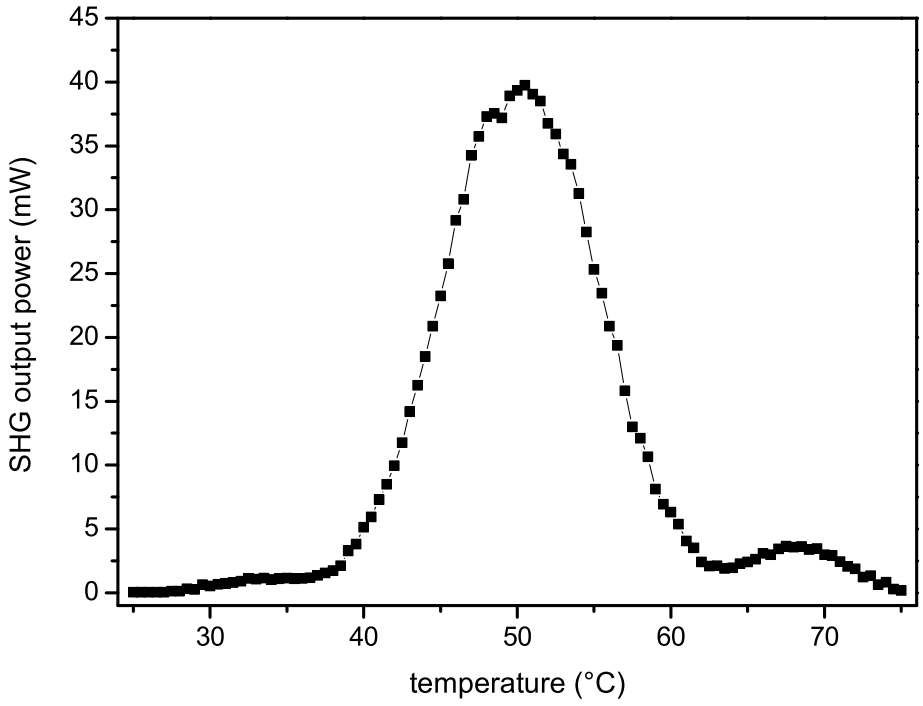

Figure 6.6: Temperature dependence of the SHG output power for intracavity frequency doubling.

Furthermore, it can be seen from Fig. 6.6, that the spectrum is not symmetric around the main peak. This effect can also be attributed to the double-pass configuration of

intracavity doubling. The reason for the asymmetric shape is an inexact final period length at the crystal end. More information and simulations concerning this effect will be presented in the following section.

6.2.3 Simulations for single period structures

To understand the shape of the curve in Fig. 6.6, simulations for SHG with periodically poled crystals in single- and double-pass configuration were conducted. All simulations presented in this section were accomplished with MatLab R2006a. The Sellmeier coefficients were taken from [Jun97].

The simulations of the wavelength dependent conversion efficiency for different poling structures were constructed as follows. First the domain structure was defined by dividing the crystal into finite elements and attributing arithmetic signs corresponding to the domain orientation at given positions within the crystal. In the next step the amplitude and the phase of the second harmonic electric field were calculated and added element by element. From the electric field amplitude behind the final element, the conversion efficiency was calculated. For all simulations continuous wave operation and low conversion efficiency per pass were assumed. The simulations yielded information about the wavelength dependent conversion efficiency and about the phase of the electric field at every position along the crystal.

The second harmonic electric field for quasi phase matching can be calculated by [Fej92]

$$E_{2\omega} = G \int_0^L d(z) e^{i\Delta k z} dz \tag{6.1}$$

where L is the crystal length, $d(z)$ contains the sign for the domain direction, dz is the step size, G is a constant containing the fundamental electric field amplitude, and Δk is the wave vector mismatch caused by dispersion. The electric field is calculated for every wavelength separately.

The simulated bandwidth acceptance for a single period crystal in single- and double-pass configuration is shown in 6.7 (top). To have comparable central peak widths, the single-pass simulation was conducted for a 2 mm long crystal and the double-pass simulation for a 1 mm long crystal. The simulated bandwidth for a single-pass follows a sinc^2-function, like has been determined experimentally. The double-pass bandwidth exhibits the same asymmetric shape as the temperature dependent SHG output power shown in Fig. 6.6. As was stated above, the temperature dependence has to be flipped for comparison with the spectral bandwidth.

The asymmetry depends on the length of the final domain in the crystal, because this length governs the relative phase of the interacting waves before the second pass [Ime98].

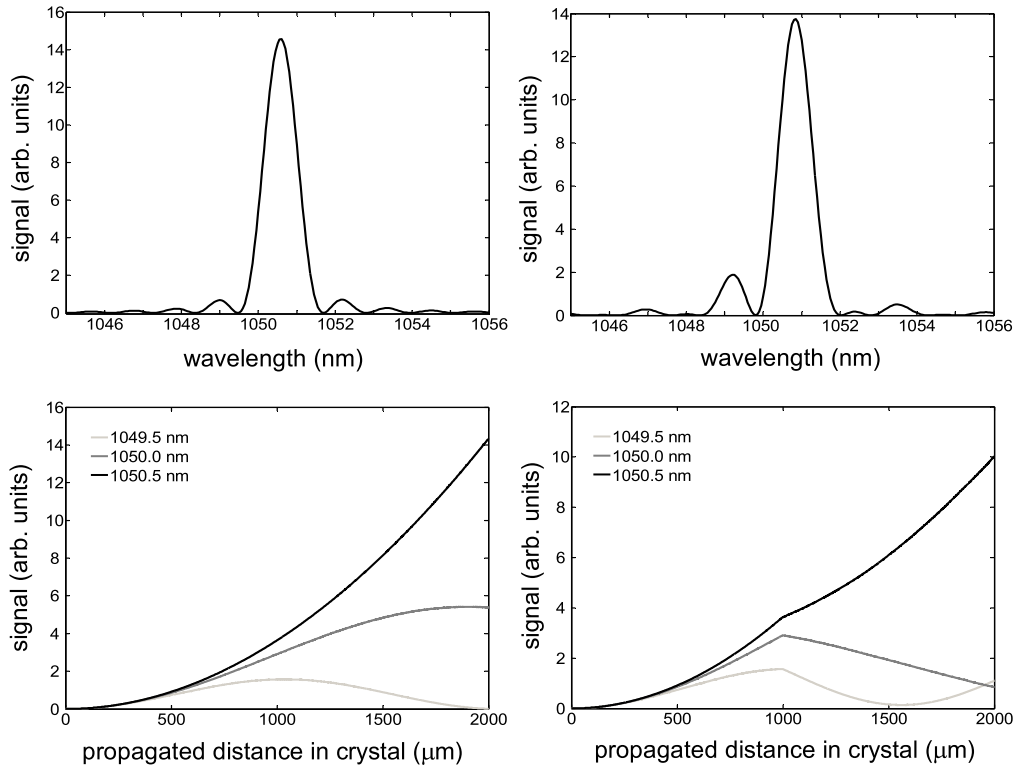

Figure 6.7: Simulated spectral acceptance (top) of the SHG efficiency for a single period PPLN crystal in a single- (left) and double-pass (right) configuration. The bottom graphs show the respective development of the SHG power over the crystal length.

By varying the final domain length, the relative phase can be controlled and accordingly the asymmetry effect can be suppressed.

The development of the converted power for three fundamental wavelengths around 1050 nm over the propagated distance in the nonlinear crystals is shown in 6.7 (bottom). It can be seen how the phase mismatch between the fundamental waves due to the final domain effects the development of the conversion efficiency on the second pass. While for the single-pass configuration the development of the SHG output power follows differentiable curves, the double-pass configuration exhibits a phase jump after the first pass.

Since the asymmetric spectral acceptance showed not significant effects on the maximum conversion efficiency for intracavity frequency doubling with MgO:PPLN, it was not required to control the length of the final domain in the presented experiments.

6.3 Bandwidth enhancement

A major drawback of MgO:PPLN is its small spectral acceptance. Especially for longer crystals this limits the practicability for broad emitting lasers and for lasers that can shift in wavelength. OPS disk lasers are designed for a certain wavelength, but the resulting gain spectrum can vary by a few nanometers. Furthermore, their gain is broad and their wavelength shifts with pump power and gain medium temperature. Accordingly crystal structures with a broadened spectral acceptance are of interest for OPS disk lasers.

The spectral acceptance is inversely proportional to the interaction length and thus can be increased by reducing the crystal length. However, this would result in a poor trade-off between conversion efficiency and spectral acceptance, since the SHG output power depends quadratically on the interaction length.

Sophisticated engineering of periodically poled crystals allows for adaption of the crystal properties to the required specifications in many cases. Different structures have been proposed to enhance the acceptance bandwidth for quasi phase matching with acceptable conversion efficiency reduction. In this section simulations and experiments using crystals with bandwidth enhanced structures will be presented.

6.3.1 External frequency doubling with cascaded structures

Quasi phase matched crystals are designed for conversion of a specific wavelength by selecting the appropriate period length of the domains. Longer domains correspond to longer wavelengths (see Fig. 6.2). The most straightforward technique to increase the phase matching bandwidth of periodically poled crystals, is using a structure with cascaded poling period like is sketched in Fig. 6.1 (c). Such a "chirped grating structure" has been proposed by Suhara *et al.* [Suh90]. The MgO:PPLN crystals presented in this section have been designed using a similar approach [Miz94], where the structure is divided into segments of different poling period (see Fig. 6.8), which is easier to process than a chirped grating.

Simulations predict good results if the segments are assembled with increasing poling periods. A structure where

$$\Lambda_1 < \Lambda_2 < \Lambda_3 < ... < \Lambda_n \tag{6.2}$$

is given, will be called cascaded structure in the following. Distinct shapes of the resulting bandwidth can be obtained by varying the segment lengths, the poling periods, the number of segments or by interchanging segment positions. The relative phase of the involved waves can also be influenced by introducing additional separation domains of variable lengths between the segments [Miz94].

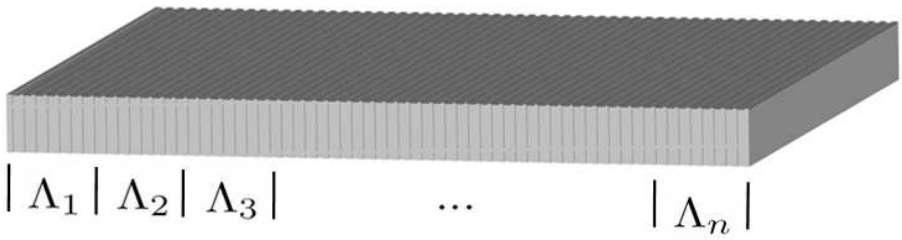

Figure 6.8: Schematic of a PPLN crystal with segmented structure.

For simulating the bandwidth of a cascaded structure, the integral from equation 6.1 has to be divided into sections corresponding to the segments of different poling period:

$$E_{2\omega} = G\left[\int_0^{L_1} d_1(z)e^{i\Delta kz}dz + \int_{L_1}^{L_2} d_2(z)e^{i\Delta kz}dz + \int_{L_2}^{L_3} d_3(z)e^{i\Delta kz}dz + \ldots\right] \tag{6.3}$$

In this equation the information about the structure is included in the $d(z)$ terms.

Fig. 6.9 shows the phase matching bandwidth of two diverse cascaded structures. Both structures comprised five segments, but the poling periods of the segments were composed differently. The total crystal length was 2.10 mm for both structures. The experimental results (top) were obtained by external SHG with the setup from Fig. 6.3 and are consistent with the simulations (bottom). The predicted values for the phase matching bandwidth (FWHM) were 3.06 nm and 3.26 nm for the left and the right structure respectively. The corresponding experimental values of 3.14 nm and 3.21 nm are in good agreement.

The experimentally determined spectral acceptances of 0.685 nm·cm and 0.674 nm·cm were increased by more than a factor of 3.5 with respect to the single period structures. Moreover, the conversion efficiency has been improved, because the efficiency reduction due to the deviation from 1st order QPM was more than compensated by the increased crystal length.

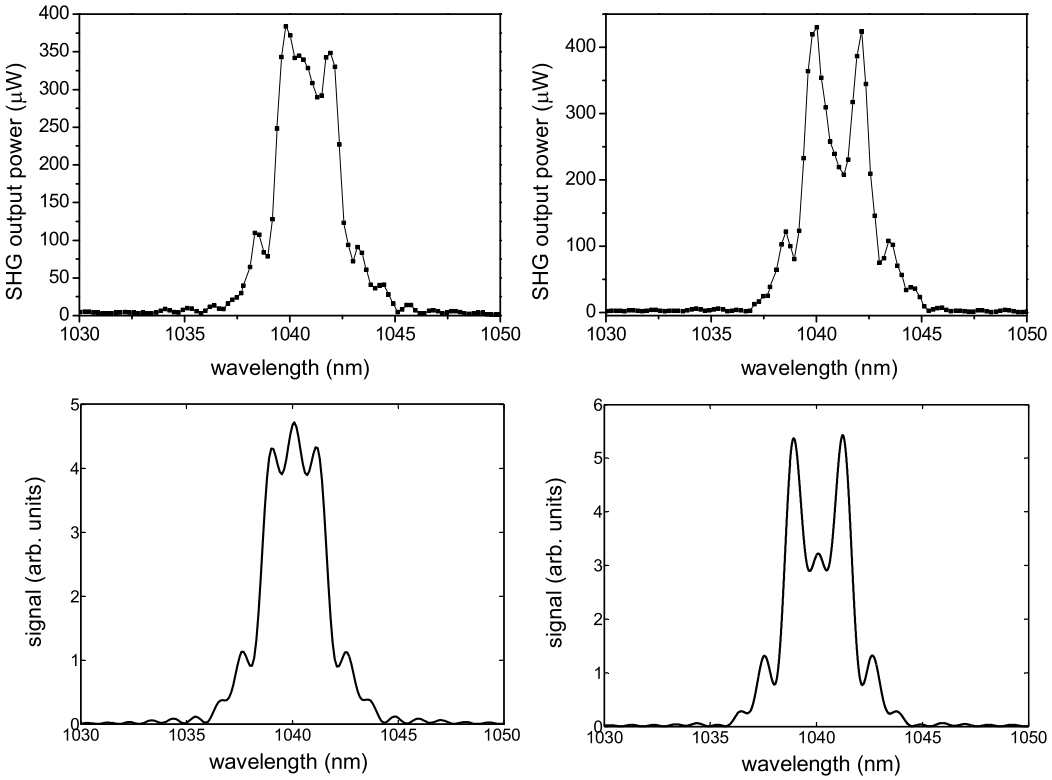

Figure 6.9: Experimental (top) and simulated (bottom) bandwidths for cascaded structures comprising five segments with different poling period.

6.3.2 Intracavity doubling with cascaded structures

For intracavity experiments a cascaded structure with 21 segments, which was anti-reflection coated on both sides, was used. Like for all presented MgO:PPLN crystals the operation temperature was 50°C. About 80 mW of green output power has been achieved from this crystal with chip 1. The conversion efficiency was satisfying, but the expected simplification of the alignment due to the broadened spectral acceptance was not attained.

The reason was found to be a break-down of the broad phase matching acceptance for the double-pass configuration. Fig. 6.10 (left) shows the temperature dependance of the SHG output power for the same crystal for a single-pass and a double-pass configuration in comparison. For single-pass conversion, the green laser emission was coupled out through both external mirrors of the V-type resonator. The black curve shows the combined SHG output power from both outcoupling directions. The shape of the acceptance curve is relatively flat and broad. The grey curve corresponds to SHG with the

standard double-pass setup. The acceptance bandwidth is interrupted by several minima. Seemingly the peaks of the measured spectrum are enveloped by the curve for the single-pass configuration. Fig. 6.10 (right) shows the corresponding simulation for a double-pass. The shape of the bandwidth is similar to the measured curve, but the minima of the spectrum are much more pronounced.

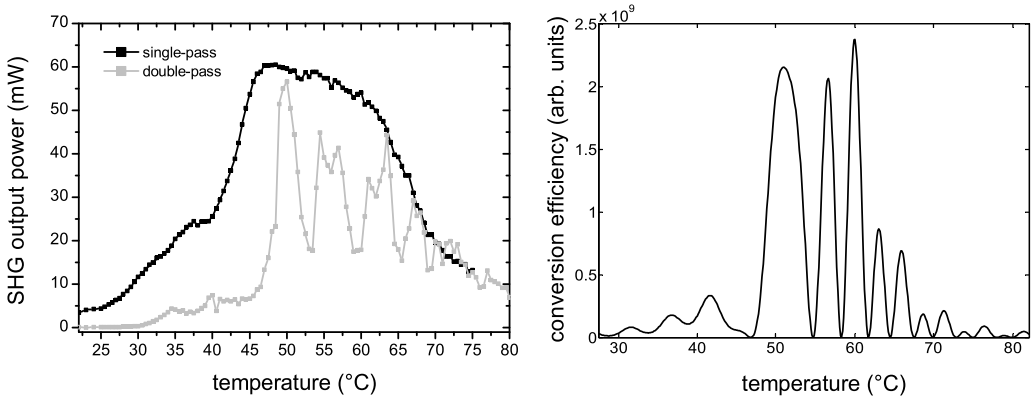

Figure 6.10: Temperature dependent SHG output power for a single-pass and a double-pass setup for a MgO:PPLN crystal with cascaded structure (left) and the corresponding simulated conversion efficiency (right).

The minima result from dispersion of the interacting waves in the nonlinear crystal. Fig. 6.11 (right) shows the simulated bandwidth acceptance for a double-pass through a 2.10 mm long structure having a symmetric single-pass spectral acceptance around 1050 nm similar to 6.9 (left). The simulated double-pass is asymmetric with several peaks and minima to the short wavelength side of the designed central wavelength and a low efficiency tail to longer wavelengths.

For a better understanding of the shape of this curve, the development of the SHG output for some wavelengths with special characteristics is shown in 6.11 (left). The left side of the graph shows the SHG output development during the first and the right side the development during the second pass. After a single pass through the periodically poled crystal, the phases of the different wavelengths have shifted with respect to each other. The curves for the wavelengths 1049.85 nm and 1051.38 nm exhibit bilateral symmetry. Accordingly all of the SHG power converted during the first pass is returned to the fundamental wave during the second pass and a minimum occurs at the respective positions in the bandwidth acceptance spectrum. The curves for 1049.48 nm and 1050.34 nm correspond to maxima and have a near rotational symmetric shape superposed with an exponential growth. The curve for 1050.10 nm exhibits no symmetry and corresponds to a wavelength in the slope of a peak. The considered wavelengths are marked with black

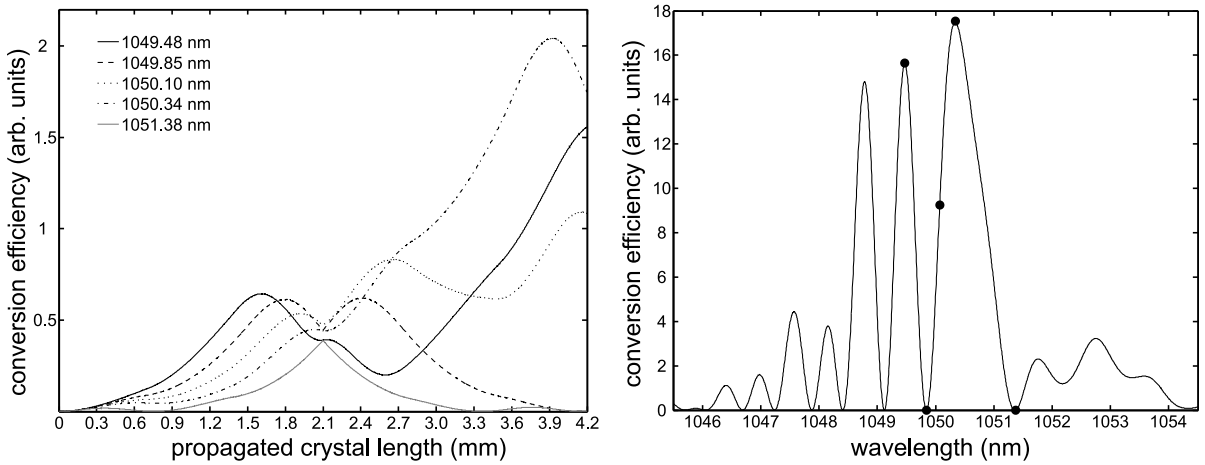

Figure 6.11: Development of the SHG output power for different wavelengths and wavelength dependent conversion efficiency for a cascaded structure comprising five segments.

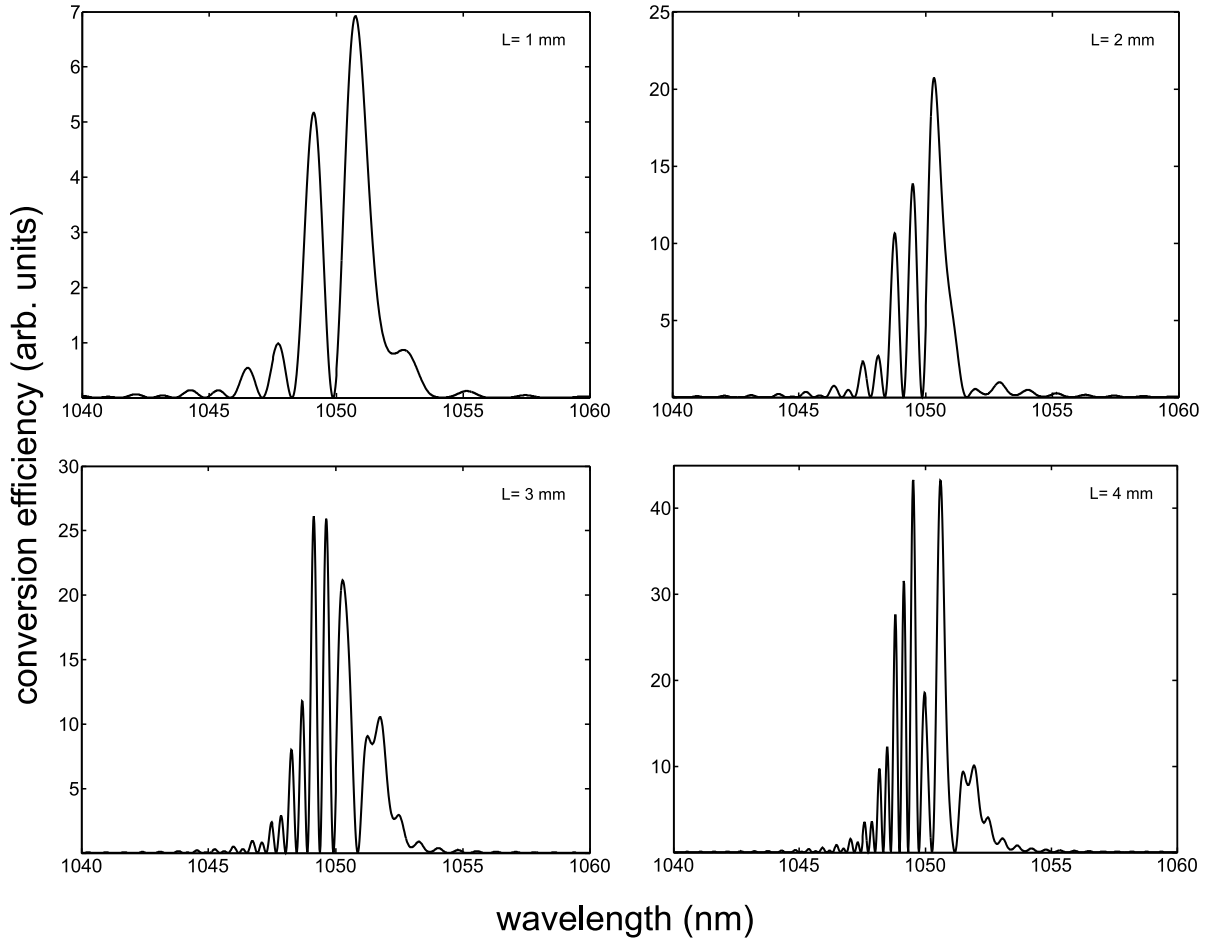

Figure 6.12: SHG efficiency for a double-pass configuration with MgO:PPLN crystals of different lengths.

dots in the bandwidth acceptance spectrum 6.11 (right). The maxima and the minima on the short wavelength side of the spectrum are almost equally spaced.

Simulations for various crystals with cascaded structures exhibit an almost linear dependence between the crystal length and the number of minima in the main comb of the bandwidth acceptance spectrum. Fig. 6.12 shows the spectra of four crystals with the same number of segments. The increase of the number of minima with the crystal length can be seen clearly. Structures with other segment numbers and poling periods exhibited the same dependence. The relation between crystal length and number of minima indicates that the distortion of the acceptance bandwidth due to the double-pass configuration is caused mainly by the dispersion of the material and that cascaded structures are generally unfeasible for double-pass configurations. However, this hypothesis was not proven mathematically. According to this result the SHG power has to be coupled out at both sides of the MgO:PPLN crystal in order to benefit from a cascaded structure in an intracavity setup.

6.3.3 Other bandwidth enhancing concepts

A cascaded or chirped grating structure is not the only way to obtain broadened spectral acceptance in periodically poled crystals. Several different approaches have been proposed and demonstrated.

Mizuuchi *et al.* demonstrated a design similar to the segmented structures presented above, which yielded a broadened flat top phase matching acceptance [Miz98]. In these structures phase shifts were achieved by varying the lengths of spacings between segments comprising the same poling period. This aperiodic grating resulted in efficient suppression of ripples on the acceptance curve.

QPM with a grating modified by equally spaced phase reversals, where the sign of the phase reversal is determined by a 13-bit Barker Code, has been predicted and demonstrated by Bortz *et al.* [Bor94]. For an optimized positioning of the phase reversals, an increase of the phase matching bandwidth by a factor of 15 with respect to an uniform grating was achieved, while the conversion efficiency was reduced by a factor of ten. However, simulations for structures designed on the basis of this paper exhibited a similar interruption of the bandwidth spectrum for a double-pass configuration like has been observed for the cascaded structures.

T. D. Reid presented a simulated annealing algorithm for analytical calculation of the SHG output for arbitrary quasi phase matching bandwidth spectra [Rei03]. The gratings were designed from a variable number of alternately inverted domains of individual length. This method allows for tailoring the grating structure to the desired shape of the frequency response.

An optical Fibonacci superlattice structure, which was first demonstrated by Zhu *et al.* [Zhu97], does not broaden the spectral acceptance, but exhibits a frequency response

allowing for SHG at several widely spaced wavelengths. These structures consist of two different building blocks that are lined up following a mathematical rule determined by a Fibonacci concatenation. Both building blocks contain two ferroelectric domains with opposite inversion and a particular lengths proportion. The conversion efficiency at the highest peaks of the spectrum is only slightly reduced with respect to a periodic structure. The poled lithium tantalate structure with a length of 8 mm realized by Zhu *et al.* yielded conversion efficiencies for external SHG of a ps-OPO ranging from $\sim 5\,\% - 20\,\%$ at the wavelengths 973 nm, 1082 nm, 1283 nm, 1365 nm, and 1569 nm.

A simulation of a 3.35 mm long optical Fibonacci superlattice structure optimized for simultaneous conversion to red, green, and blue is shown in Fig. 6.13. The grating was designed to meet the fundamental wavelength of the OPS disk laser at 1050 nm. For this structure the fundamental wavelengths for SHG to red and blue are 1231 nm and 908 nm respectively and their second harmonics are suitable for display technology. An OPS disk laser around 1231 nm recently has been demonstrated at significant output power [Har07]. In combination with the presented MgO:PPLN crystal and the laser presented in this thesis, frequency doubling of two different OPS disk laser in a single medium would be possible. Furthermore, simulations indicate, that Fibonacci superlattice gratings can be used in double-pass configurations. Superposing a chirp to the structure results in broadening of the single peaks. However, the broadened acceptance collapses for double-passes.

6.4 Conclusions

The results presented in this section prove, that MgO:PPLN is a suitable crystal for intracavity doubling of OPS disk lasers to the green spectral range. The combination of high conversion efficiency and good beam quality make it superior to the birefringent phase matched crystals presented in the previous section regarding consumer applications in display technology.

Bandwidth enhancement by using cascaded structures is possible for intracavity frequency doubling if the SHG power is coupled out to both sides of the nonlinear crystal. The advantageous increase of bandwidth acceptance is lost in a double-pass configuration, where the acceptance spectrum is interrupted by several minima caused by dispersion. The number of minima presumably only depends on the crystal length.

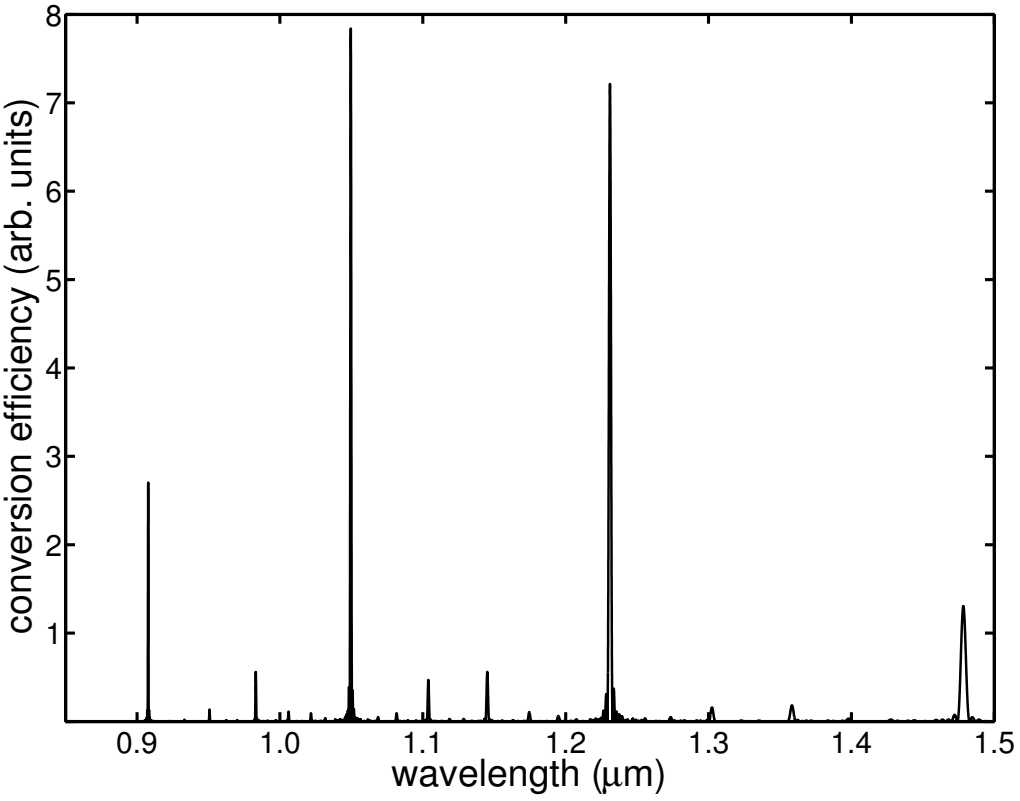

Figure 6.13: Conversion efficiency for a Fibonacci superlattice structure optimized for simultaneous SHG to red, green, and blue.

7 Dynamics of the output amplitude

A basic problem for intracavity frequency doubling of diode pumped solid state lasers are large amplitude fluctuations of the output, widely known as the green-problem [Bae86]. These fluctuations originate from nonlinear coupling effects between different resonator modes and can have very high modulation depths. In contrast, intracavity frequency doubled OPS disk lasers with a simple spectral filter typically exhibit stable output and seemingly do not suffer from the green-problem [Fan06b]. In this chapter the dynamic behavior of the continuous wave SHG and SFG output of OPS disk lasers will be discussed.

7.1 Amplitude fluctuations of DPSSL and the model of Baer

The term green-problem originates from the well-established system of a Nd:YAG laser being intracavity frequency doubled to 532 nm. These laser systems typically exhibit large fluctuations of the output amplitude if no particular setup is used [Smi70]. The stabilization of the output often requires special cavity designs [Ant92]. For example efficient stabilization can be achieved by placing the gain medium and nonlinear crystal at resonator positions, where nonlinear coupling of different longitudinal modes is strongly reduced [Cze03].

Amplitude fluctuations due to nonlinear longitudinal mode coupling were first theoretically described by Baer [Bae86]. With a KTP intracavity frequency doubled end-pumped Nd:YAG laser Bear observed chaotic amplitude fluctuations. Inserting an intracavity etalon yielded stable output for single-mode operation and well defined oscillations of the output power when two modes were present simultaneously. The theoretical model of Baer provided a suitable explanation for the experimentally observed effects.

Starting from time dependent rate equations for the of laser intensity and gain, Baer included term accounting for sum frequency generation and cross saturation effects and obtained a set of differential equations to describe an intracavity doubled laser operating on two modes:

$$\begin{aligned}
\tau_c \frac{dI_1}{dt} &= (G_1 - \alpha_1 - \varepsilon I_1 - 2\varepsilon I_2) I_1 \\
\tau_f \frac{dG_1}{dt} &= -(\beta I_1 + \beta_{12} I_2 + 1) G_1 + {G_1}^0 \\
\tau_c \frac{dI_2}{dt} &= (G_2 - \alpha_2 - \varepsilon I_2 - 2\varepsilon I_1) I_2 \\
\tau_f \frac{dG_2}{dt} &= -(\beta I_2 + \beta_{21} I_1 + 1) G_2 + {G_2}^0
\end{aligned} \tag{7.1}$$

where τ_c and τ_f are the cavity round trip time and the fluorescence lifetime, I is the mode intensity, α is the mode-loss, ε is the nonlinear coupling coefficient, β is the saturation parameter, G^0 is the small signal gain, and $\beta_{12} = \beta_{21}$ is the cross saturation parameter. The subscripts correspond to mode 1 and mode 2. The model can easily be expanded to higher mode numbers.

Following conclusions result from the equations above. For single-mode operation the laser output is stable. If two modes are oscillating, they tend to pulse periodically out of phase with each other. The turn-on peak of the modes predicted by the model is overestimated in comparison with the experiment. Baer accounts this to a deviation of the system from an ideal 4-level-laser. For three or more modes the fluctuations are chaotic and the amplitude decreases with increasing mode number due to averaging effects. The frequency of the fluctuation is only weakly effected by the pump power, but depends on the nonlinear coupling. For decreasing nonlinear coupling the oscillation frequency increases, until it reaches the relaxation oscillation of the laser. If the nonlinear coupling is further decreased, the laser becomes stable.

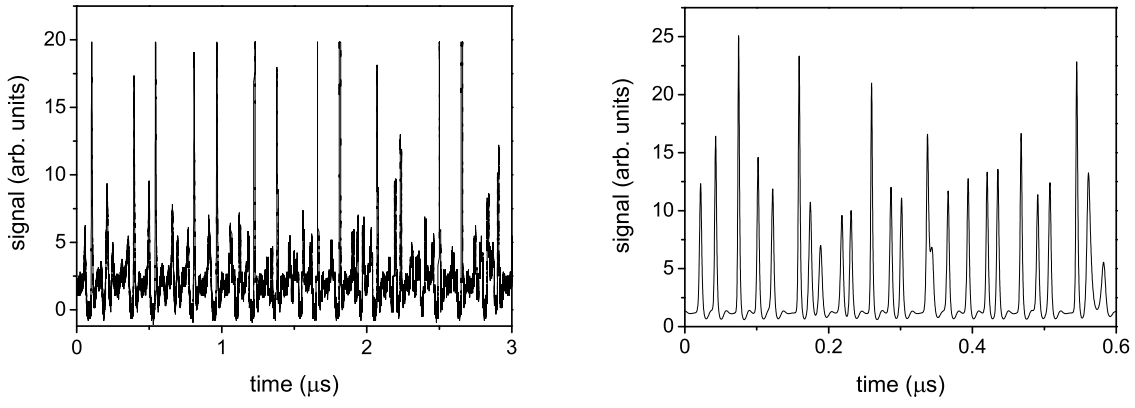

(a) experimental (b) theoretical

Figure 7.1: (a) Experimental and (b) theoretical amplitude dynamics of a continuous wave Nd:YVO_4 micro-chip laser.

According to the model of Baer, one possibility to avoid the amplitude fluctuations is to realize single-mode operation. Other methods are to suppress SFG or averaging over a high number of modes (> 100). These methods have been accomplished in numerous works (e. g. [Oka88], [Mag93]).

To compare the OPS disk laser to a compact diode pumped solid state laser, the SHG output of a Nd:YVO_4/KTP micro-chip laser has been measured. The laser consisted of a 2.0 mm long Nd:YVO_4 crystal bonded to a KTP crystal of 0.5 mm length. The outer surfaces of the crystals were coated to form the resonator. The system was pumped by an 808 nm diode laser. The dynamic behavior of the output amplitude is shown in Fig. 7.1 (a). Chaotic fluctuations indicate, that more than two fundamental modes were oscillating in the short cavity. A simulation of the output dynamics for the case of four oscillating modes using the differential equations proposed by Baer is shown in Fig. 7.1 (b). The results look similar, but the time scale is different. This deviation is presumably caused by the high uncertainty of simulation parameters, particularly of the approximated nonlinear coupling.

7.2 Differences for OPS disk lasers

The output dynamics of continuous wave OPS disk lasers differ from those of diode pumped solid state lasers. One reason is the drastically shorter fluorescence lifetime, which typically is on the order of a few nanoseconds. If such a short lifetime is included to the simulations following the Baer model, stable operation of the laser is predicted if all other parameters are unchanged. Another difference is the resonant periodic gain structure. Since the gain material is positioned at the anti-nodes of the intracavity standing wave pattern, longitudinal spatial hole burning in the laser material is suppressed efficiently and therefore inhomogeneous broadening, which is known to be a possible source of laser instabilities [Abr85], is reduced.

In the chapters 5 and 6 it has been shown, that type I phase matched BiBO and quasi phase matched MgO:PPLN yield the best output characteristics for the OPS disk lasers. In contrast to the type II phase matched KTP typically used for intracavity frequency doubling of Nd:YAG lasers, the output dynamics for these phase matching concepts is not influenced by polarization modes. This is advantageous for achieving the desired stable laser operation.

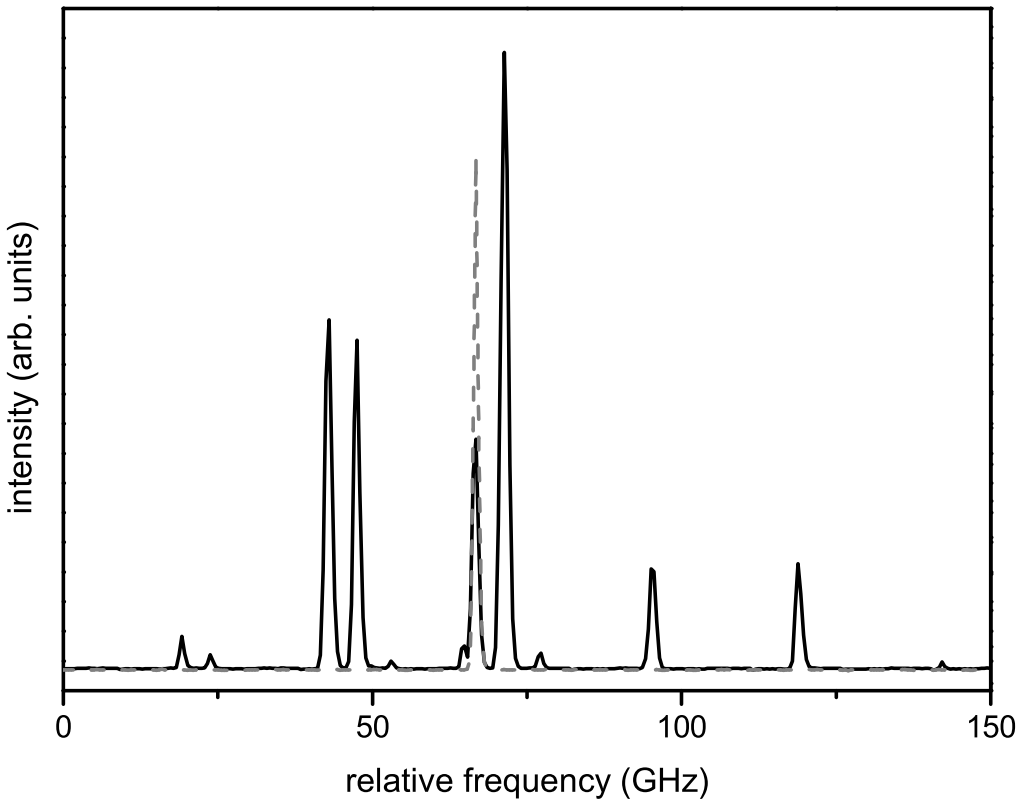

Figure 7.2: Integrated mode spectrum for a frequency doubled OPS disk laser with a linear resonator and an intracavity etalon. The single measurements exhibit only one mode (dashed line). Mode-hopping occurs between more than ten positions. The peak intensities indicate how much a mode position contributes to the total output power.

7.3 Output dynamics of the OPS disk laser

The setup for the presented experiments was the standard V-type resonator. A 6 mm long BiBO crystal was used for frequency conversion. The output dynamics was detected with a fast Si-photodiode (rise time < 1 ns). Scattered pump light and emission at the fundamental wavelength were blocked by a glass filter (Schott BG18). To distinguish between the amplitude fluctuations of the laser emission and background noise of the detector, a chopper was used in front of the Si-photodiode. Furthermore, a grating spectrometer with high resolution was applied to measure the laser spectrum and the

mode dynamics.

7.3.1 Infrared and SHG dynamics

On the fundamental wave OPS disk lasers tend to fall into stable single-mode operation, if an intracavity spectral filter is applied [Jac07]. For short external cavity lengths ($5\,\text{mm} < L < 30\,\text{mm}$), like are desired for compact display lasers, the laser output was reported to settle at linearly polarized, stable single-mode operation on a sub-millisecond time scale even without any intracavity element [Gar07]. Measurements of the infrared output of the OPS disk laser for the linear and the V-type cavity confirmed these results. The emitted infrared output was stable on long and short timescales.

The mode spectrum of the frequency doubled OPS disk laser was recorded with a reflection grating spectrometer. For these measurements a shorter, linear cavity setup with a length of 74 mm was used to meet the resolution of the spectrometer. A 30 µm thick etalon was used as spectral filter. The laser was found to operate in a single-mode regime with mode-hopping between more than ten different mode positions. Fig. 7.2 shows the integrated output for 500 single measurements taken at a rate of 0.1 Hz. A typical picture of a single measurement is indicated by the dashed curve. The fractional contribution of each mode to the total SHG output power is given by the height of the peaks in the spectrum.

The dynamic behavior of one of the modes measured with a photo multiplier tube can be seen in Fig. 7.3. The same mode is shown on two different time scales. The left picture shows the typical start up of a mode, a stable operation regime, and the fading to a different mode. From the first appearance of the mode to the stable regime it only took a few milliseconds. Stable oscillation of single modes up to a few seconds was observed. The fade to a different mode exhibited a bistability. This behavior was similar for all main modes, while for the lateral modes only short-term excitation occurred. Presumably the lateral modes are only excited during the fading process from one main mode to the next one.

The right hand side of Fig. 7.3 shows a sector in the fading regime denoted by the vertical dashed lines in the left picture. In both graphs the intensity varies between only two values corresponding to full or zero intensity of the green laser output. These intensity levels are the same for every mode position, which verifies that only one mode is oscillating at a time.

This tendency for single-mode operation is the main reason for the stable output of intracavity doubled OPS disk lasers. It results from the nearly ideal homogeneous gain broadening, where adjacent modes seize the same spatial inversion distribution [Gar07]. But even if two adjacent modes are oscillating at the same time, which can be the case for longer cavities, no green-problem was observed. This can be attributed to a strong gain-coupling of the modes, i. e. both modes see the same spectral gain and almost the

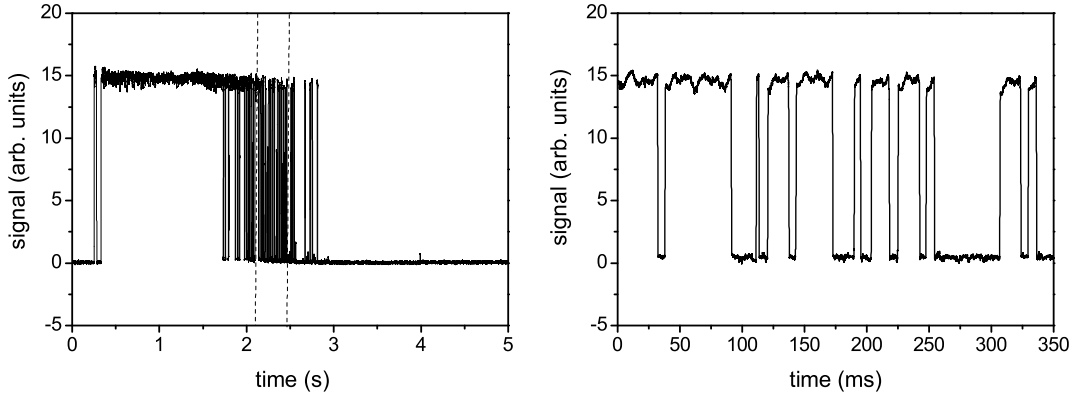

Figure 7.3: Mode dynamics on long and short timescales. The dynamic of the modes is similar for all main modes.

same spatial gain distribution. The effects of gain-decoupling will be discussed in the following section.

7.3.2 SFG dynamics

To examine the dependence of the output dynamics on the gain-decoupling of laser modes, the frequency conversion setup was employed to dual-wavelength operation in the infrared, like has been presented in section 3.3.4, and the phase matching alignment of the nonlinear crystal was optimized for sum frequency generation. The alignment of the resonator was quite delicate, since the two fundamental wavelengths had to be stabilized at a position, where they were subject to high nonlinear losses. The green output power obtained for the presented output dynamics was in a range of 10 mW to 30 mW at pump powers around 500 mW.

Etalons of different thicknesses were used to vary the gap between the two fundamental wavelengths. The infrared wavelengths were separated by 12.4 nm, 2.5 nm, 0.51 nm, and 0.13 nm respectively. Emission spectra for the green spectral range are shown on the left side in Fig. 7.4. In these spectra the outer peaks result from SHG and the middle peak can be attributed to SFG. The presence of the SFG component indicates, that two infrared wavelengths were oscillating simultaneously. The top spectrum also contains the infrared spectrum (dashed lines, top scale), since here the SHG components almost have vanished due to the limitations of spectral acceptance.

The right hand side of Fig. 7.4 displays the chopped laser output corresponding to the respective emission spectra. It can be seen, that the green-problem occurs, if the OPS

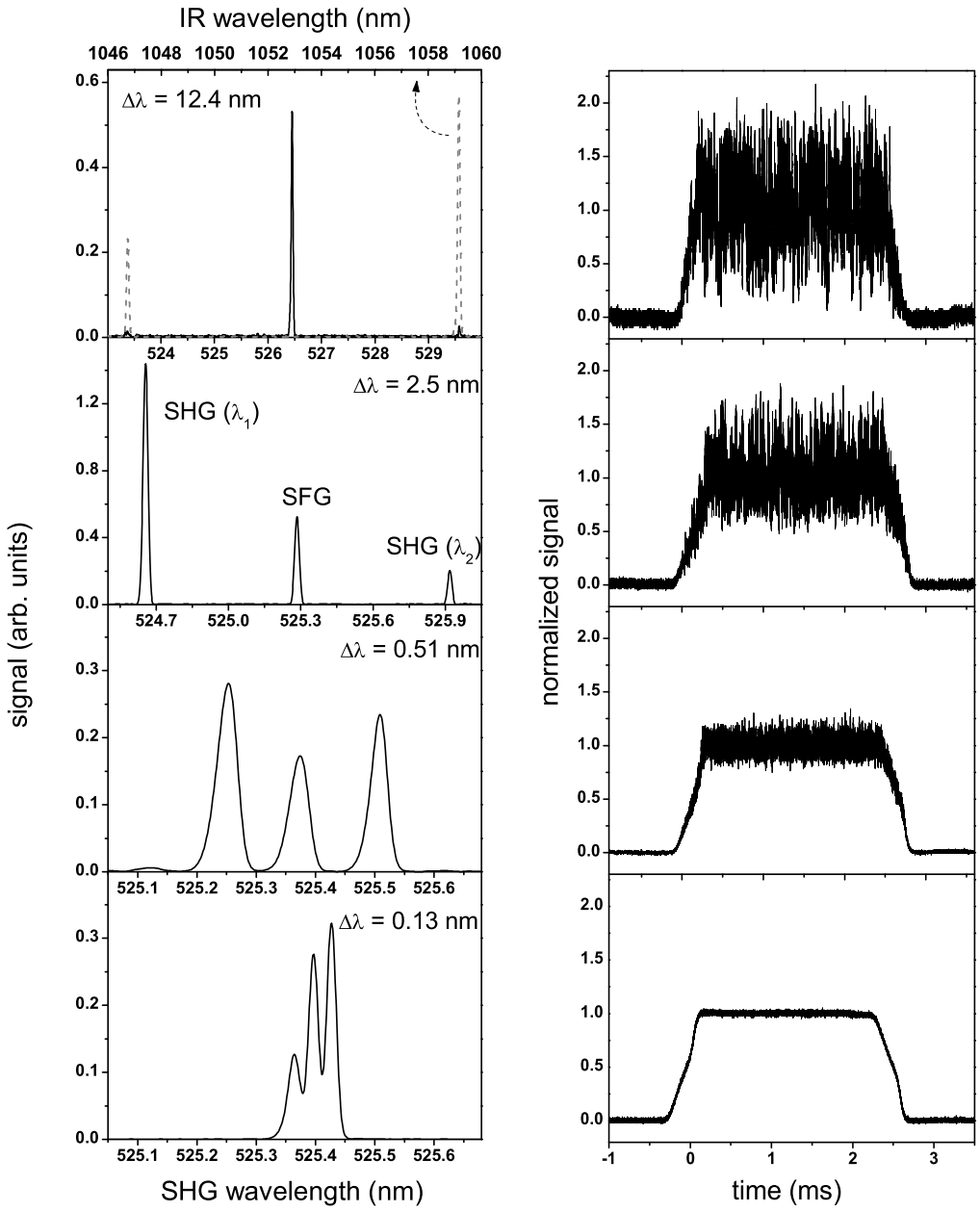

Figure 7.4: Emission spectra (left) and the corresponding amplitude fluctuations (right) for different wavelength separations.

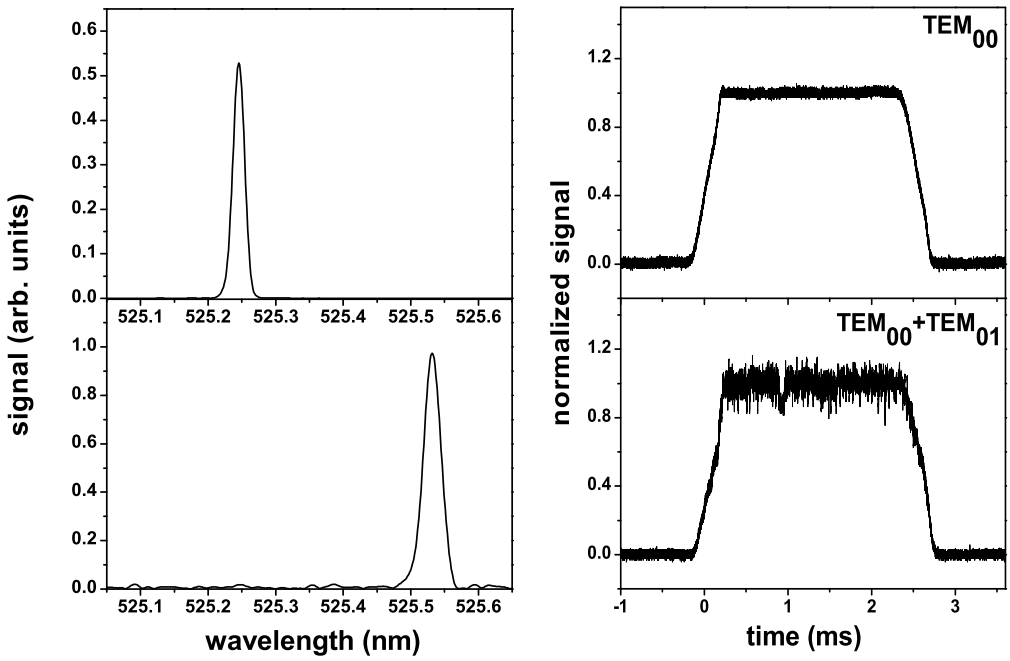

Figure 7.5: Emission spectra (left) and the corresponding amplitude fluctuations (right) for pure TEM_{00} output and for combined TEM_{00} and TEM_{01} output. In the latter case the emission linewidth is inhomogeneously broadened.

disk laser was forced to dual-wavelength operation at larger wavelength separation. The gain-decoupling of the two laser modes due to spatial inhomogeneity increases with the mode spacing. It was observed that the noise amplitude reduced for smaller spectral gaps. The rms deviations of the signal were 34.0%, 20.9%, 6.8%, and 1.3% respectively. For a gap of 0.13 nm the fluctuations have almost vanished. This is possible, because due to the short gain region length, which had a thickness of approximately 2 µm, and to the resonant periodic gain structure, the gain-decoupling of two modes is much smaller for OPS disk lasers than for typical solid state lasers, which are longer by several orders of magnitude.

Spatial decoupling of modes increases if higher transversal modes are present. In Fig. 7.5 the noise is compared for the generation of a pure TEM_{00} mode and for the additional excitation of a small fraction of TEM_{01} mode. In the latter case the transversal spatial decoupling of the modes was sufficient to cause amplitude fluctuations.

Work on a theoretical model to simulate the dependence of the noise amplitude on the

gain-decoupling is in progress at the Institute of Laser-Physics in Hamburg. The model includes modes that vary in polarization and frequency. The total inversion is distributed over many sections and for each mode four different contributions are calculated to seize this inversion. To account for the quantum noise, Langevin forces are included [Bac04]. The model already has proven to predict a decoupling parameter for longitudinal and polarization modes of a diode pumped multi-mode Nd:YAG laser [Bon07].

7.3.3 Noise frequency analysis

In the previous section it has been demonstrated, which conditions lead to the occurrence of the green-problem in OPS disk lasers. The amplitude of the noise has been shown to depend on the gain-decoupling of the oscillating modes. Further information about the noise characteristics can be gained by analyzing the frequency components of the output amplitude fluctuations.

As stated above, the output amplitude has been recorded using a fast photodiode with a time resolution of less than one nanosecond. In combination with an oscilloscope with high sampling rate, frequencies up to the GHz-range were detectable. For these measurements the chopper was removed from the setup. The noise characteristics for SFG of infrared waves spaced by 0.51 nm is shown in Fig. 7.6. The picture shows the output amplitude on different time scales ranging from nanoseconds to milliseconds. It can be seen, how the different frequency components add up to form the total output signal. The first picture (50 ns) displays the highest frequency that could be resolved. This frequency presumably is the relaxation oscillation frequency of the laser. The lower frequencies can at least partially be attributed to the green-problem. The characteristic noise frequencies were similar for all wavelength spacings presented above.

Fig. 7.7 (a) shows the fast Fourier transformation (FFT) spectra for the case of SFG with a fundamental wavelength spacing of 0.51 nm and (b) for SHG with a 30 µm etalon as wavelength selective element in comparison. The peaks in the FFT spectrum of the SFG output are located at 159 MHz, 267 MHz, 287 MHz, 318 MHz, and 446 MHz. The peaks at 159 MHz and 318 MHz assumedly correspond to the relaxation oscillation frequency for the given setup and its second harmonic. 446 MHz is the beat frequency of two adjacent modes of the resonator, which indicates, that the single-mode operation is disturbed and that every now and than two modes are excited simultaneously. The oscillation frequencies at 267 MHz, 287 MHz only occur for sum frequency generation and vary in position for the different infrared wavelength spacings.

The SHG output exhibited no amplitude fluctuations and the FFT spectrum (Fig. 7.7 (b)) indicates that relaxation oscillations do not occur. However, if the system is altered, e. g. by a change of temperature or movements of the thin etalon due to streaming air, also for this system relaxation oscillations were observed at the same frequency.

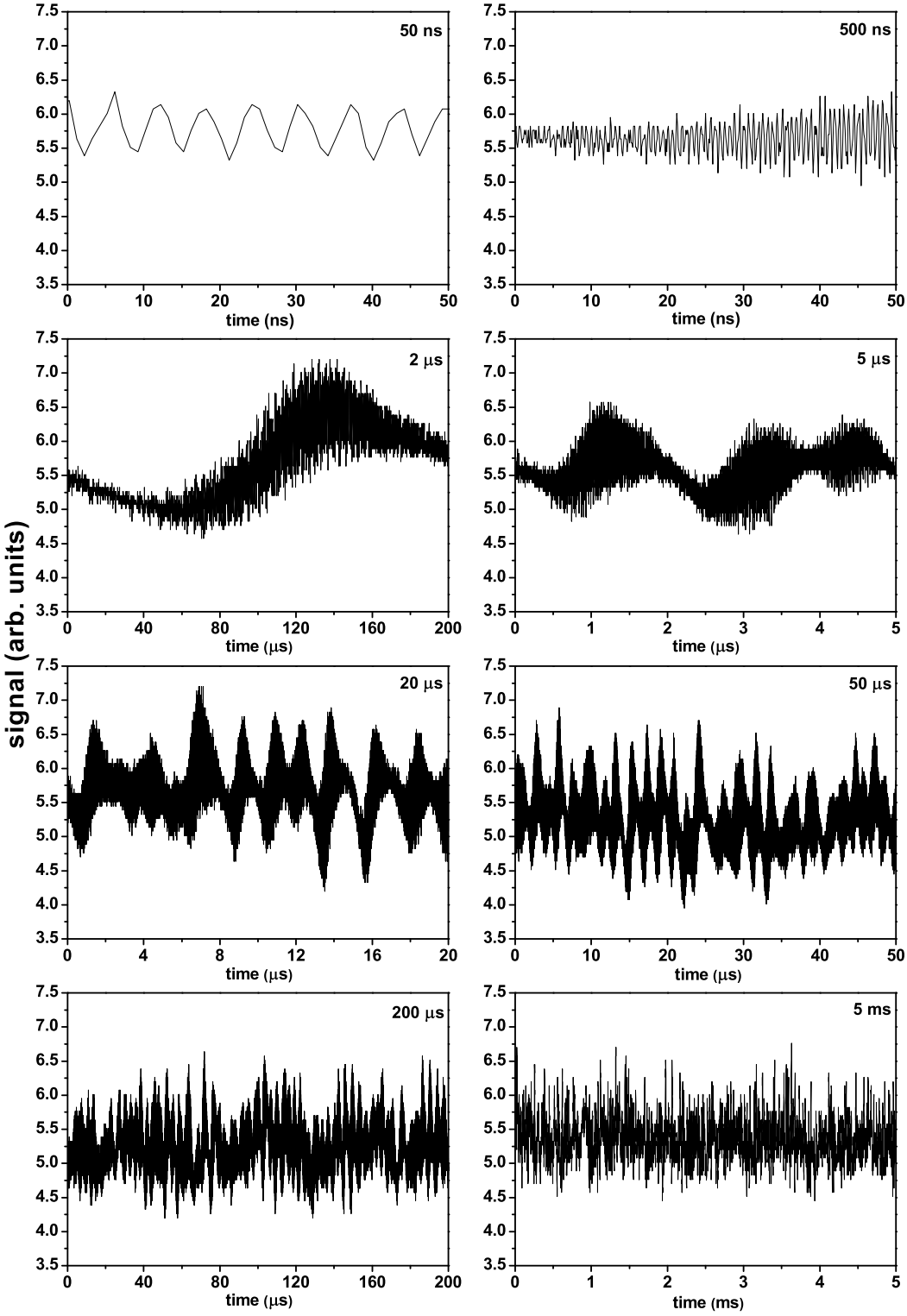

Figure 7.6: SFG amplitude signal for different time resolution.

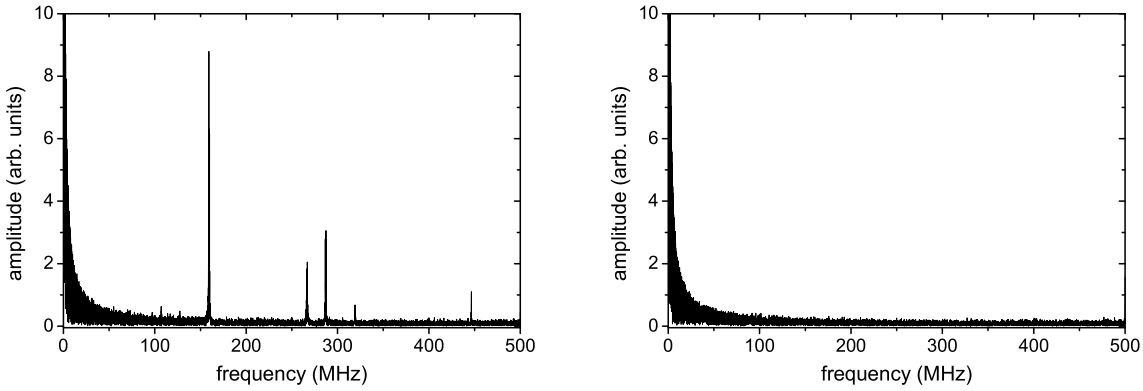

(a) SFG with 0.51 nm gap

(b) SHG with intracavity etalon

Figure 7.7: FFT spectra for laser emission with SFG and 0.51 nm gap on the fundamental wavelength (a) and for SHG without amplitude fluctuations (b). In the latter case relaxation oscillations were observed only if the system was disturbed externally.

7.4 Conclusions

In summary, an experimental study about the output dynamics of intracavity frequency conversion of OPS disk lasers via SHG and SFG was presented. The typical stable emission of SHG could be attributed to a tendency for single-mode operation. The low gain-decoupling, which is due to the short gain medium length and the resonant periodic gain structure, allowed for stable operation even if two modes were oscillating simultaneously. It was shown, how gain-decoupling resulted in large amplitude fluctuations if the laser was forced to operate on two widely spaced wavelengths simultaneously. Work on a theoretical model including spatial inhomogeneity of the gain is in progress at the Institute of Laser-Physics in Hamburg. Furthermore, the output amplitude has been analyzed regarding its frequency components.

8 Conclusions

8.1 Summary of the results

The aim of this thesis was to characterize and improve an OPS disk laser emitting in the green spectral range towards the requirements of laser display systems for consumer markets. A compact setup with good efficiency and high beam quality was developed. The adaptability to high volume production was taken into account.

The presented OPS disk lasers operated at a fundamental wavelength around 1050 nm. The lasers yielded up to a few hundred milli-Watts of near diffraction limited infrared output power and optical conversion efficiencies up to 45 %. The emission wavelength was observed to shift with temperature. By spectral filtering with an etalon or a birefringent filter, the emission linewidth was reduced to below 0.1 nm. Tunability over more than 20 nm has been achieved and simultaneous oscillation on two wavelengths has been demonstrated.

The nonlinear crystals LBO, KTP, BiBO, and MgO:PPLN have been compared regarding applicability to a V-type resonator setup optimized for efficient intracavity SHG. A record conversion efficiency to 525 nm of more than 80 % with respect to the maximum available infrared power has been achieved with a 6 mm long BiBO crystal at an output power of 113 mW. However, setups containing BiBO as nonlinear crystal suffered from a reduced beam quality due to the high walk-off angle of BiBO. LBO and KTP yielded near diffraction limited beam quality, but exhibited relatively low output powers.

The best overall performance has been realized using a 5 % MgO doped single-period PPLN crystal with the dimensions $0.50 \times 0.90 \times 1.25\,\mathrm{mm}^3$. For this crystal a maximum output power at 525 nm of 69 mW has been achieved corresponding to a conversion efficiency of 49.6% with respect to the maximum available infrared power. The beam quality was near diffraction limited and the output amplitude was stable. For MgO:PPLN bandwidth enhanced structures have been simulated and experimentally demonstrated in single- and double-pass configurations. For intracavity SHG it has been shown, that outcoupling to both sides of the nonlinear crystal is necessary to profit from the broadened phase matching acceptance.

Furthermore, it has been shown, that intracavity doubled OPS disk lasers do not suffer from the green-problem due to a tendency for single-mode operation. Amplitude fluctuations were demonstrated to depend on the gain-decoupling of simultaneously oscillating

modes.

In conclusion, it has been demonstrated that compact intracavity doubled OPS disk lasers are promising for application to laser displays, since they provide stable output with high beam quality and good efficiency. The semiconductor chips and the nonlinear PPLN crystals can be fabricated on wafer scale, which limits the high volume production costs. The results presented in this thesis presumably can be transferred to OPS disk lasers operating at other fundamental wavelengths.

8.2 Outlook

Further improvements of the laser system can be achieved by optimizing the MgO:PPLN crystal dimensions. Experiments indicated, that enhanced conversion efficiency can be expected for slightly longer crystals. Furthermore, advanced ferroelectric poling techniques could allow for an increase of the crystal thickness.

To integrate RGB projectors into portable devices like cell phones or notebooks, a more compact design of the lasers is required. The best solution would be an integrated setup containing all components and colors.

For illuminating large screens and for back-projection of TVs higher powers are needed. Power scalability of the compact concept is possible by increasing the pump spot diameter and the pump power as well as by building arrays of OPS disk lasers.

Bibliography

[Abr85] N. B. Abraham, L. A. Lugiato, and L. M. Narducci, *Overview of instabilities in laser systems*, J. Opt. Soc. Am. B **2**, 7-14 (1985)

[Alb05] T. Albrecht, W. Diehl, P. Brick, S. Lutgen, and J. Luft, *Efficient Quantum-Well Pumping of Semiconductor Disk Lasers at* 920 *nm*, Conference on Lasers and Electro-Optics (CLEO), CMFF7 (2005)

[Alf02] W. J. Alford, T. D. Raymond, and A. A. Allerman, *High power and good beam quality at* 980 *nm from a vertical external-cavity surface-emitting laser*, J. Opt. Soc. Am. B **19**, 663-666 (2002)

[Ant92] D. W. Anthon, D. L. Sipes, T. J. Pier, and M. R. Ressl, *Intracavity Doubling of CW Diode-Pumped Nd:YAG Lasers with KTP*, IEEE J. Quantum Electron. **28**, 1148-1157 (1992)

[Arm62] J. A. Armstrong, N. Bloembergen, J. Ducuing, and P. S. Pershan, *Interactions between Light Waves in a Nonlinear Dielectric*, Phys. Rev. **127**, 1918 (1962)

[Bac04] O. Back, *Theoretische Modellierung der Emissionsdynamik eines Vielmoden-Festkörperlasers*, Diplomarbeit, Institut für Laser-Physik, Universität Hamburg (2004)

[Bae86] T. Baer, *Large-amplitude fluctuations due to longitudinal mode coupling in diode-pumped intracavity-doubled Nd:YAG lasers*, J. Opt. Soc. Am. B **3**, 1175-1180 (1986)

[Bat98] R. G. Batchko, G. D. Miller, A. Alexandrovski, M. M. Fejer, and R. L. Byer, *Limitations of high-power visible wavelength periodically poled lithium niobate devices due to green-induced infrared absorption and thermal lensing*, OSA Technical Digest Series **12**, 75-76 (1998)

[Bed05] R. G. Bedford, M. Kolesik, J. L. A. Chilla, M. K. Reed, T. R. Nelson, and J. V. Moloney, *Power-limit mechanisms in VECSELs*, Proc. SPIE **5814**, 199-208 (2005)

[Bey05] S. Beyertt, M. Zorn, T. Kübler, H. Wenzel, M. Weyers, A. Giesen, G. Tränkle, and U. Brauch, *Optical In-Well Pumping of a Semiconductor Disk Laser with High Optical Efficiency*, IEEE J. Quantum Electron. **41**, 1439-1449 (2005)

[Bey07] S. Beyertt, U. Brauch, F. Demaria, N. Dhidah, A. Giesen, T. Kübler, S. Lorch, F. Rinaldi, and P. Unger, *Efficient Gallium-Arsenide Disk Laser*, IEEE J. Quantum Electron. **43**, 869-875 (2007)

[Bie89] J. D. Bierlein and H. Vanherzeele, *Potassium titanyl phosphate: properties and new applications*, J. Opt. Soc. Am. B **6**, 622-633 (1989)

[Bon07] T. Bonin, *Emissionsdynamik eines Mehrmoden-Festkörperlasers*, Diplomarbeit, Institut für Laser-Physik, Universität Hamburg (2007)

[Bor94] M. L. Bortz, M. Fujimura, and M. M. Fejer, *Increased acceptance bandwidth for quasi-phasematched second harmonic generation in* $LiNbO_3$, IEEE Electron. Lett. **30**, 34-35 (1994)

[Bou99] B. Boulanger, I. Rousseau, J. P. Fève, M. Maglione, B. Mènaert, and G. Marnier, *Optical Studies of Laser-Induced Gray-Tracking in KTP*, IEEE J. Quantum Electron. **35**, 281-286 (1999)

[Boy65] R. W. Boyd, A. Ashkin, J. M. Dziedzic, and D. A. Kleinman, *Second-Harmonic Generation of Light with Double Refraction*, Phys. Rev. **137**, 1305-1320 (1965)

[Boy03] R. W. Boyd, *Nonlinear Optics*, 2nd Edition, Academic Press, San Diego (2003)

[Bry84] D. A. Bryan, R. Gerson, and H. E. Tomaschke, *Increases optical damage resistance in lithium niobate*, Appl. Phys. Lett. **44**, 847-849 (1984)

[Bye97] R. L. Byer, *Quasi-phasematched nonlinear interactions and devices*, J. Nonlinear Opt. Phys. Mater. **6**, 549-592 (1997)

[Cai88] J. A. Caird, S. A. Payne, P. R. Staver, A. J. Ramponi, L. L. Chase, and W. F. Krupke, *Quantum Electronic Properties of the* $Na_3Ga_2Li_3F_{12} : Cr^{3+}$ *Laser*, IEEE J. Quantum Electron. **24**, 1077-1099 (1988)

[Che89] C. Chen, Y. Wu, A. Jiang, B. Wu, G. You, R. Li, and S. Lin, *New nonlinear-optical crystal:* LiB_3O_5, J. Opt. Soc. Am. B **6**, 616-621 (1989)

[Che05] Y. Chen, W. Yan, J. Guo, S. Chen, G. Zhang, and Z. Xia, *Effect of Mg concentration on the domain reversal of Mg-doped* $LiNbO_3$, Appl. Phys. Lett. **87**, 212904 (2005)

[Cho94] W. W. Chow, S. W. Koch, and M. Sargent III, *Semiconductor-Laser Physics*, Springer-Verlag, Berlin, Heidelberg (1994)

[Cze03] C. Czeranowsky, V. Baev, and G. Huber, *Stabilization of intracavity frequency -doubled lasers with type I phase matching*, Opt. Lett. **28**, 2100-2102 (2003)

[Die07] W. Diehl, P. Brick, S. Chatterjee, S. Horst, K. Hantke, W. W. Rühl, W. Stolz, A. Thränhardt, and S. W. Koch, *Dynamic behavior of* 1040 *nm semiconductor disk lasers on a nanosecond time scale*, Appl. Phys. Lett. **90**, 241102 (2007)

[Dmi99] V. G. Dmitriev, G. G. Gurzadyan, D. N. Nikogosyan, *Handbook of Nonlinear Optical Crystals*, 3rd Edition, Springer Series in Optical Science, Springer-Verlag, Berlin, Heidelberg (1999)

[Fan05] L. Fan, M. Fallahi, J. Hader, A. R. Zakharian, M. Kolesik, J. V. Moloney, T. Qui, A. Schülzgen, N Peyghambarian, W. Stolz, S. W. Koch, and J. T. Murray, *Over 3 W high efficiency vertical-external-cavity surface-emitting lasers and application as efficient fiber laser pump sources*, Appl. Phys. Lett. **86**, 211116 (2005)

[Fan06] L. Fan, M. Fallahi, J. Hader, A. R. Zakharian, J. V. Moloney, J. T. Murray, R. Bedford, W. Stolz, and S. W. Koch, *Multichip certical-external-cavity surface-emitting lasers: a coherent power scaling scheme*, Opt. Lett. **31**, 3612-3614 (2006)

[Fan06b] L. Fan, T. Hsu, M. Fallahi, J. Murray, R. Bedford, Y. Kaneda, J. Hader, A. Zakharian, J. Moloney, S. Koch, and W. Stolz, *Tunable watt-level blue-green vertical-external-cavity surface-emitting lasers by intracavity frequency doubling*, Appl. Phys. Lett. **88**, 251117 (2006)

[Fan07] L. Fan, M. Fallahi, J. Hader, A. R. Zakharian, J. V. Moloney, W. Stolz, S. W. Koch, R. Bedford, and J. T. Murray, *Linearly polarized dual-wavelength vertical-external-cavity surface-emitting laser*, Appl. Phys. Lett. **90**, 181124 (2007)

[Fej92] M. M. Fejer, G. A. Magel, D. H. Jundt, and R. L. Byer, *Quasi-Phase-Matched Second Harmonic Generation - Tuning and Tolerances*, IEEE J. Quantum Electron. **28**, 2631-2654 (1992)

[Fra61] P. A. Franken, A. E. Hill, C. W. Peters, and G. Weinreich, *Generation of Optical Harmonics*, Phys. Rev. Lett. **7**, 118-120 (1961)

[Fre04] S. T. Fredrich, *Charakterisierung der Lasereigenschaften von* $Nd:YVO_4$ *und* $Nd:GdVO_4$, Diplomarbeit, Institut für Laser-Physik, Universität Hamburg (2004)

[Fur01] Y. Furukawa, K. Kitamura, A. Alexandrovski, R. K. Route, M. M. Fejer, and G. Foulon, *Green-induced infrared absorption in MgO doped* $LiNbO_3$, Appl. Phys. Lett. **78**, 1970-1972 (2001)

[Gar99] A. Garnache, A. A. Kachanov, F. Stoeckel, and R. Planel, *High-sensitivity intracavity laser absorption spectroscopy with vertical-external-cavity surface emitting semiconductor lasers*, Opt. Letters **24**, 826-828 (1999)

[Gar00] A. Garnache, A. A. Kachanov, F. Stoeckel, and R. Houdré, *Diode-pumped broadband vertical-external-cavity surface emitting semiconductor laser applied to high-sensitivity intracavity absorption spectroscopy*, J. Opt. Soc. Am. B **17**, 1589-1598 (2000)

[Gar06] A. Garnache, A. Ouvrard, L. Cerutti, D. Barat, A. Vicet, F. Genty, Y. Rouillard, D. Romanini, and E. Cerda-Méndez, $2-2.7\ \mu m$ *single frequency tunable Sb-based lasers operating in CW at RT: Microcavity and External-Cavity VCSELs, DFB*, Proc. SPIE Photonics Europe, Semiconductor lasers and laser dynamics, 6184-23 (2006)

[Gar07] A. Garnache, A. Ouvrard, and D. Romanini, *Single-Frequency operation of External-Cavity VCSELs: Non-linear multimode temporal dynamics and quantum limit*, Opt. Express **15**, 9403-9417 (2007)

[Gie94] A. Giesen, H. Hügel, A. Voss, K. Wittig, U. Brauch and H. Opower, *Scalable Concept for Diode-Pumped High-Power Solid-State Lasers*, Appl. Phys. B **58**, 365-372 (1994)

[Gho04] M. Ghotbi and M. Ebrahim-Zadeh, *Optical second harmonic generation properties of* BiB_3O_6, Opt. Express **12**, 6002-6019 (2004)

[Gie07] A. Giesen, J. Speiser, R. Peters, C. Kränkel, and K. Petermann, *Thin-disk lasers come of age*, Photonics Spectra **41**, 52 (2007)

[Har06] A. Härkönen, M. Guina, O. Okhotnikov, K. Rößner, M. Hümmer, T. Lehnhardt, M. Müller, A. Forchel, M. Fischer, *1-W antimonide-based vertical external cavity surface emitting laser operating at* $2-\mu m$, Opt. Express **14**, 6479-6484 (2006)

[Har07] A. Härkönen, J. Rautiainen, M. Guina, J. Konttinen, P. Tuomisto, L. Orsila, M. Pessa, and O. G. Okhotnikov, *High power frequency doubled GaInNAs semiconductor disk laser emitting at* 615 *nm*, Opt. Express **15**, 3224-3229 (2007)

[Has05] J. Hastie, S. Calvez, M. Dawson, T. Leinonen, A. Laakso, J. Lyytikäinen, and M. Pessa, *High power CW red VECSEL with linearly polarized TEM00 output beam*, Opt. Express **13**, 77-81 (2005)

[Has06] J. E. Hastie, L. G. Morton, A. J. Kemp, M. D. Dawson, A. B. Krysa, and J. B. Roberts, *Tunable ultraviolet output from an intracavity frequency-doubled red vertical-external-cavity surface-emitting laser*, Appl. Phys. Lett. **89**, 061114 (2006)

[Hel99] H. Hellwig, J. Liebertz, and L. Bohaty, *Exceptional Large Nonlinear Optical Coefficients in the Monolclinic Bismuth Borate* BiB_3O_6 *(BiBO)*, Solid State Comm. **109**, 249-251 (1999)

[Hel00] H. Hellwig, J. Liebertz, and L. Bohaty, *Linear optical properties of the monoclinic bismuth borate* BiB_3O_6, J. Appl. Phys. **88**, 240-244 (2000)

[Hem07] N. Hempler, J. M. Hopkins, A. J. Kemp, N. Schulz, M. Rattunde, J. Wagner, M. D. Dawson, and D. Burns, *Pulsed pumping of semiconductor disk lasers*, Opt. Express **15**, 3248-3256 (2007)

[Hob67] M. V. Hobden, *Phase-Matched Second Harmonic Generation in Biaxial Crystals*, J. Appl. Phys. **38**, 4365-4372 (1967)

[Hoc66] E. F. Hockings, I. Kudman, T. E. Seidel, C. M. Schmelz, and E. F. Steigmeier, *Thermal and electrical transport in InAs-GaAs alloys*, J. Appl. Phys. **37**, 2879-2887 (1966)

[Hoo00] S. Hoogland, S. Dhanjal, A. C. Tropper, J. S. Roberts, R. Häring, R. Paschotta, F. Morier-Genoud, and U. Keller, *Passively Mode-Locked Diode-Pumped Surface-Emitting Semiconductor Laser*, IEEE Photon. Technol. Lett. **12**, 1135-1137 (2000)

[Ime98] G. Imeshev, M. Proctor, and M. M. Fejer, *Phase correction in double-pass quasi-phase-matched second-harmonic generation with a wedged crystal*, Opt. Lett. **23**, 165-167 (1998)

[Ish03] H. Ishizuki, I. Shoji, and T. Taira, *Periodical poling characteristics of congruent $MgO:LiNbO_3$ crystals at elevated temperature*, Appl. Phys. Lett. **82**, 4062-4064 (2003)

[Jac07] M. Jacquemet, M. Domenech, G. Lucas-Leclin, P. Georges, J. Dion, M. Strassner, I. Sagnes, and A. Garnache, *Single-frequency cw vertical external cavity surface emitting semiconductor laser at* 1003 *nm and* 501 *nm by intracavity frequency doubling*, Appl. Phys. B **86**, 503-510 (2007)

[Jun97] D. H. Jundt, *Temperature-dependent Sellmeier equation for the index of refraction, n_e, in congruent lithium niobate*, Opt. Lett. **22**, 1553-1555 (1997)

[Kat90] K. Kato, *Tunable UV Generation to* 0.2325 μm *in* $LiB_3 0_5$, IEEE J. Quantum Electron. **26**, 1173-1175 (1990)

[Kat02] K. Kato and E. Takaoka, *Sellmeier and thermo-optic dispersion formulas for KTP*, Appl. Opt. **41**, 5040-5044 (2002)

[Kel06] U. Keller and A. C. Tropper, *Passively modelocked surface-emitting semiconductor lasers*, Phys. Rep. **429**, 67-120 (2006)

[Kem06] A. J. Kemp, A. J. MacLean, J. E. Hastie, S. A. Smith, J. M. Hopkins, S. Calvez, G. J. Valentine, M. D. Dawson, and D. Burns, *Thermal lensing, thermal management and transverse mode control in microchip VECSELs*, Appl. Phys. B **83**, 189-194 (2006)

[Kim06] G. B. Kim, J. Y. Kim, J. H. Lee, Y. R. Yoo, K. S. Kim, S. M. Lee, S. H. Cho, S. J. Lim, T. Kim, and Y. J. Park, *End-pumped green and blue vertical external cavity surface emitting laser devices*, Appl. Phys. Lett. **89**, 181106 (2006)

[Kle62] D. A. Kleinman, *Nonlinear Dielectric Polarization in Optical Media*, Phys. Rev. **6**, 1977 (1962)

[Kuz97] M. Kuznetsov, F. Hakimi, R. Sprague, and A. Mooradian, *High-Power (>0.5-W CW) Diode-Pumped Vertical-External-Cavity Surface-Emitting Semiconductor Lasers with Circular TEM_{00} Beams*, IEEE Photon. Technol. Lett. **9**, 1063 (1997)

[Kuz99] M. Kuznetsov, F. Hakimi, R. Sprague, and A. Mooradian, *Design and Characterization of High-Power (>0.5-W CW) Diode-Pumped Vertical-External-Cavity Surface-Emitting Semiconductor Lasers with Circular TEM_{00} Beams*, IEEE Sel. Topics Quant. Electron. **5**, 561 (1999)

[Lee06a] J. H. Lee, J. Y. Kim, S. M. Lee, Y. R. Yoo, K. S. Kim, S. H. Cho, S. J. Lim, G. B. Kim, S. M. Hwang, T. Kim, and Y. J. Park, *9.1-W High-Efficient Continous-Wave End-Pumped Vertical-External-Cavity Surface-Emitting Semiconductor Laser*, IEEE Photonics Technol. Lett. **18**, 2117-2119 (2006)

[Lee06b] J. H. Lee, S. M. Lee, T. Kim, and Y. J. Park , *7 W high-efficiency continuous-wave green light generation by intracavity frequency doubling of an end-pumped vertical external-cavity surface emitting semiconductor laser*, Appl. Phys. Lett. **89**, 241107 (2006)

[Lei05] T. Leinonen, Y. A. Morozov, A. Härkönen, and M. Pessa, *Vertical External-Cavity Surface-Emitting Laser for Dual-Wavelength Generation*, IEEE Photonics Technol. Lett. **17**, 2508-2510 (2005)

[Li03] H. E. Li and K. Iga, *Vertical-Cavity Surface-Emitting Laser Devices*, Springer-Verlag, Berlin Heidelberg (2003)

[Lut03] S. Lutgen, T. Albrecht, P. Brick, W. Reill, J. Luft, and W. Späth , *8-W high-efficiency continuous-wave semiconductor disk laser at 1000 nm*, Appl. Phys. Lett. **82**, 3620-3622 (2003)

[Mag93] V. Magni, G. Cerullo, S. De Silvestri, O. Svelto, L. J. Qian, and M. Danailov, *Intracavity frequency doubling of a cw high-power TEM_{00} Nd:YLF laser*, Opt. Lett. **18**, 2111-2113 (1993)

[Mai60] T. H. Maiman, *Stimulated optical radiation in ruby*, Nature **4736**, 493 (1960)

[McG07] S. J. McGinily, R. H. Abram, K. S. Gardner, E. Riis, A. I. Ferguson, and J. S. Roberts, *Novel Gain Medium Design for Short-Wavelength Vertical-External-Cavity Surface-Emitting Laser*, IEEE J. Quantum Electron. **43**, 445-450 (2007)

[Miz94] K. Mizuuchi, K. Yamamoto, M. Kato, and H. Sato, *Broadening of the Phase-Matching Bandwidth in Quasi-Phase-Matched Second-Harmonic Generation*, IEEE J. Quantum Electron. **30**, 1596-1604 (1994)

[Miz98] K. Mizuuchi and K. Yamamoto, *Waveguide second-harmonic generation device with broadened flat quasi-phase-matching response by use of a grating structure with located phase shifts*, Opt. Lett. **23**, 1880-1882 (1998)

[Moo01] A. Mooradian, *High Brightness, cavity-controlled, electrically pumped surface emitting GaInAs lasers operating at 980nm*, Proc. Int. Conf. on Opt. Fiber Commun. (OFC), Postdeadline Paper (2001)

[Mul03] M. I. Müller, C. Karnutsch, J. Luft, W. Schmid, K. Streubel, N. Linder, S.-S. Beyertt, U. Brauch, A. Giesen, and G. H. Döhler, *Optically pumped vertical-external-cavity semiconductor thin disk laser with cw operation at* 660 *nm*, Proc. Int. Symp. Compound Semiconductors **174**, 427-430 (2003)

[Oka88] M. Oka and S. Kubota, *Stable intracavity doubling of orthogonal linearly polarized modes in diode-pumped Nd:YAG lasers*, Opt. Lett. **13**, 805 (1988)

[Pet07] R. Peters, C. Kränkel, K. Petermann, and G. Huber, *Broadly tunable high-power $Yb:Lu_2O_3$ thin disk laser with* 80% *slope efficiency*, Opt. Express **15**, 7075-7082 (2007)

[Raf03] E. U. Rafailov, W. Sibbett, A. Mooradian, J. G. McInerney, H. Karlsson, S. Wang, and F. Laurell, *Efficient frequency doubling of a vertical-extended-cavity surface-emitting laser diode by use of a periodically poled KTP crystal*, Opt. Lett. **28**, 2091-2093 (2003)

[Rei03] D. T. Reid, *Engineered quasi-phase-matching for second-harmonic generation*, J. Opt. A: Pure Appl. Opt. **5**, 97-102 (2003)

[Saa06] F. Saas, V. Talalaev, U. Griebner, J. W. Tomm, M. Zorn, A. Knigge, and M. Weyers, *Optically pumped semiconductor disk laser with graded and step indices*, Appl. Phys. Lett. **89**, 151120 (2006)

[Saa06b] E. J. Saarinen, A. Härkönen, S. Suomalainen, and O. G. Okhotnikov, *Power scalable semiconductor disk laser using multiple gain cavity*, Opt. Express **14**, 12868-12871 (2006)

[Sch04] M. Schmid, S. Benchabane, F. Torabi-Goudarzi, R. Abram, A. I. Fergison, and E. Riis, *Optical in-well pumping of a vertical-external-cavity surface-emitting laser*, Appl. Phys. Lett. **84**, 4860-4862 (2004)

[Sch07] N. Schulz, M. Rattunde, C. Ritzenthaler, B. Rösener, C. Manz, K. Köhler, and J. Wagner, *Resonant optical in-well pumping of an (AlGaIn)(AsSb)-based vertical-external-cavity surface-emitting laser emiting at* 2.35 μm, Appl. Phys. Lett. **91**, 091113 (2007)

[Shc03] A. V. Shchegrov, D. Lee, J. P. Watson, A. Umbrasas, E. M. Strzelecka, M. K. Liebman, C. A. Amsden, A. Lewis, V. V. Doan, B. D. Moran, J. G. McInerney, and A. Mooradian, *488nm coherent emission by intracavity frequency doubling of extended cavity surface-emitting diode lasers*, Proc. SPIE **4994**, 197 (2003)

[She84] Y. R. Shen, *The Principles of Nonlinear Optics*, John Wiley, New York (2003)

[Smi70] R. G. Smith, *Theory of Intracavity Second-Harmonic Generation*, IEEE J. Quantum Electron. **6**, 215-223 (1970)

[Su06] K. W. Su, S. C. Huang, A. Li, S. C. Liu, Y. F. Chen, and K. F. Huang, *High-peak-power AlGaInAs quantum-well 1.3-μm laser pumped by a diode-pumped actively Q-switched solid-state laser*, Opt. Lett. **31**, 2009-2011 (2006)

[Suh90] T. Suhara, and H. Nishihara, *Theoretical Analysis of Waveguide Second-Harmonic Generation with Uniform and Chirped Gratings*, IEEE J. Quantum Electron. **26**, 1265-1276 (1990)

[Sut96] R. L. Sutherland, *Handbook of Nonlinear Optics*, Marcel Dekker Inc., New York (1996)

[Sve98] O. Svelto, *Principles of Lasers*, 4th edition, Plenum Press, New York (1998)

[Tal95] J. Talghader and J. S. Smith, *Thermal dependence of the refractive index of GaAs and AlAs measured using semiconductor multilayer optical cavities*, Appl. Phys. Lett. **66**, 335-337 (1995)

[Tro04] A. C. Tropper, H. D. Foreman, A. Garnache, K. G. Wilcox, and S. H. Hoogland, *Vertical-external-cavity semiconductor lasers*, J. Phys. D: Appl. Phys. **37**, R75-R85 (2004)

[Tro06] A. C. Tropper and S. Hoogland, *Extended cavity surface-emitting semiconductor lasers*, Prog. in Quantum Electron. **30**, 1-43 (2006)

[Uka90] T. Ukachi, R. J. Lane, W. R. Bosenberg, and C. L. Tang, *Measurements of noncritically phase matched second-harmonic generation in a LiB_3O_5 crystal*, Appl. Phys. Lett. **57**, 980-982 (1990)

[Wes06] V. Wesemann, J. A. L'Huillier, L. K. Friess, P. A. v. Loewis of Menar, G. Bitz, A. Borsutzky, R. Wallenstein, T. Salva, S. Vernay und D. Rytz, *Optical properties of BiB_3O_6 with different phase matching orientations*, Appl. Phys. B **87**, 95-99 (2007).

[Yam93] M. Yamada, N. Nada, M. Saitoh, and K. Watanabe, *First-order quasi phase-matched LiNbO waveguide periodically poled by applying an external electric field for efficient blue second-harmonic generation*, Appl. Phys. Lett. **62**, 435-436 (1993)

[Zel97] D. E. Zelmon, D. L. Small, and D. Jundt, *Infrared corrected Sellmeier coefficients for congruently grown lithium niobate and 5mol.% magnesium oxide-doped lithium niobate*, J. Opt. Soc. Am. B **14**, 3319-3322 (1997)

[Zhu97] S. Zhu, Y. Zhu, Y. Qin, H. Wang, C. Ge, and, N. Ming, *Experimental Realization of Second Harmonic Generation in a Fibonacci Optical Superlattice of $LiTaO_3$*, Phys. Rev. Lett. **78**, 2752-2755 (1997)

[Zhu03] Y. Zhu, X. Chen, J. Shi, Y. Chen, Y. Xia, and Y. Chen, *Wide-range tunable wavelength filter in periodically poled lithium niobate*, Opt. Commun. **228**, 139-143 (2003)

[Zon03a] J. J. Zondy, C. Bonnin, and D. Lupinski, *Second-harmonic generation with monolithic walk-off-compensating periodic structures. I. Theory*, J. Opt. Soc. Am. B **20**, 1675-1694 (2003)

[Zon03b] J. J. Zondy, D. Kolker, C. Bonnin, and D. Lupinski, *Second-harmonic generation with monolithic walk-off-compensating periodic structures. II. Experiment*, J. Opt. Soc. Am. B **20**, 1695-1707 (2003)

[Zum76] F. C. Zumsteg, J. D. Bierlein, and T. E. Gier, *$K_xR_{1-x}TiOPO_4$: A new nonlinear optical material*, J. Appl. Phys. **47**, 4980-4985 (1976)

Acknowledgments

During the three years I have been working on this thesis, I was supported by many people to whom I am deeply grateful. I want to thank

- Prof. Dr. Günter Huber for the opportunity to work and learn within his group

- Prof. Dr. Ernst Heumann for supervising the VISULASE sub-project ORFOS

- Dr. Klaus Petermann for answering endless questions

- my colleagues, the technical stuff, and our secretary Silke Frömmig for the great atmosphere and their helpfulness

- Dr. Kühnelt and Dr. Steegmüller from Osram Opto Semiconductors GmbH for providing material and knowledge

- Dr. Valery Baev and Kai Seger for supporting the amplitude fluctuation experiments

- the BMBF for the funding (FKZ 13N8592)

- my family for everything

- all others who supported me and my work